Stockholm University

Bachelor Thesis

Independent project in
Geochemistry, 30 hp

A field and laboratory study of suspected biotic features in Svecofennian rocks on Utö in the Stockholm Archipelago

Katja Smurakova

Stockholm 2024

Department of Geological Sciences
Stockholm University
SE-106 91 Stockholm

Abstract

This study investigates the potential biotic origin of sedimentary structures located at Södra Sandvik, Utö, by combining field observations and laboratory analyses. A sedimentological log was constructed to interpret depositional facies of the outcrop, evidence of metamorphism and deformation was analyzed through field and petrographic observations, SEM-EDS analysis was performed to examine possible biotic morphologies and to perform geochemical analysis, while fluorescence microscopy was used to detect any organic remains. The study applies a falsification approach to evaluate both biotic and abiotic explanations for the origin of the structures. Field observations identified potential microbially induced sedimentary structures (MISS), including irregular crinkled laminations, a roll up clast and a structure with thin undulating laminations thickening over small surface irregularities. The sedimentary log included laminations, concretions, soft sediment deformation features along with several sets of ripples, which were found to be consistent with a medial to distal turbidite system transitioning into a deeper setting. Multiple metamorphic events evidenced by the presence of cordierite, biotite, crenulation cleavage, sagenitic textures and reaction rims etc., could have erased biological signatures. The SEM analysis showed no carbon, iron cycling minerals or diagnostic microbial morphologies or textures. The chemical analysis detected REEs, distributed in monazite and zircon and as trace amounts across the outcrop, but showed no association with the laminations. While the features at Södra Sandvik visually resemble MISS, no conclusive evidence supporting biotic origin was found. Through the falsification approach all observed features and iron-cycling processes can be explained by abiotic mechanisms. It cannot be fully ruled out that MISS once existed, however, metamorphic overprint may have erased any biosignatures.

Table of Contents

1.0 Introduction

Situated in the southern part of the Stockholm Archipelago, the island of Utö emerged from the geological forces of the Svecofennian orogeny, approximately 1.91 to 1.87 Ga and is now part of the Baltic Shield (Fig. 1; Gavelin *et al.* 1976; SGU 2024). The bedrock of Utö acts as a geological time capsule, preserving traces of ancient and complex geological processes that shaped the region (Talbot 2008).

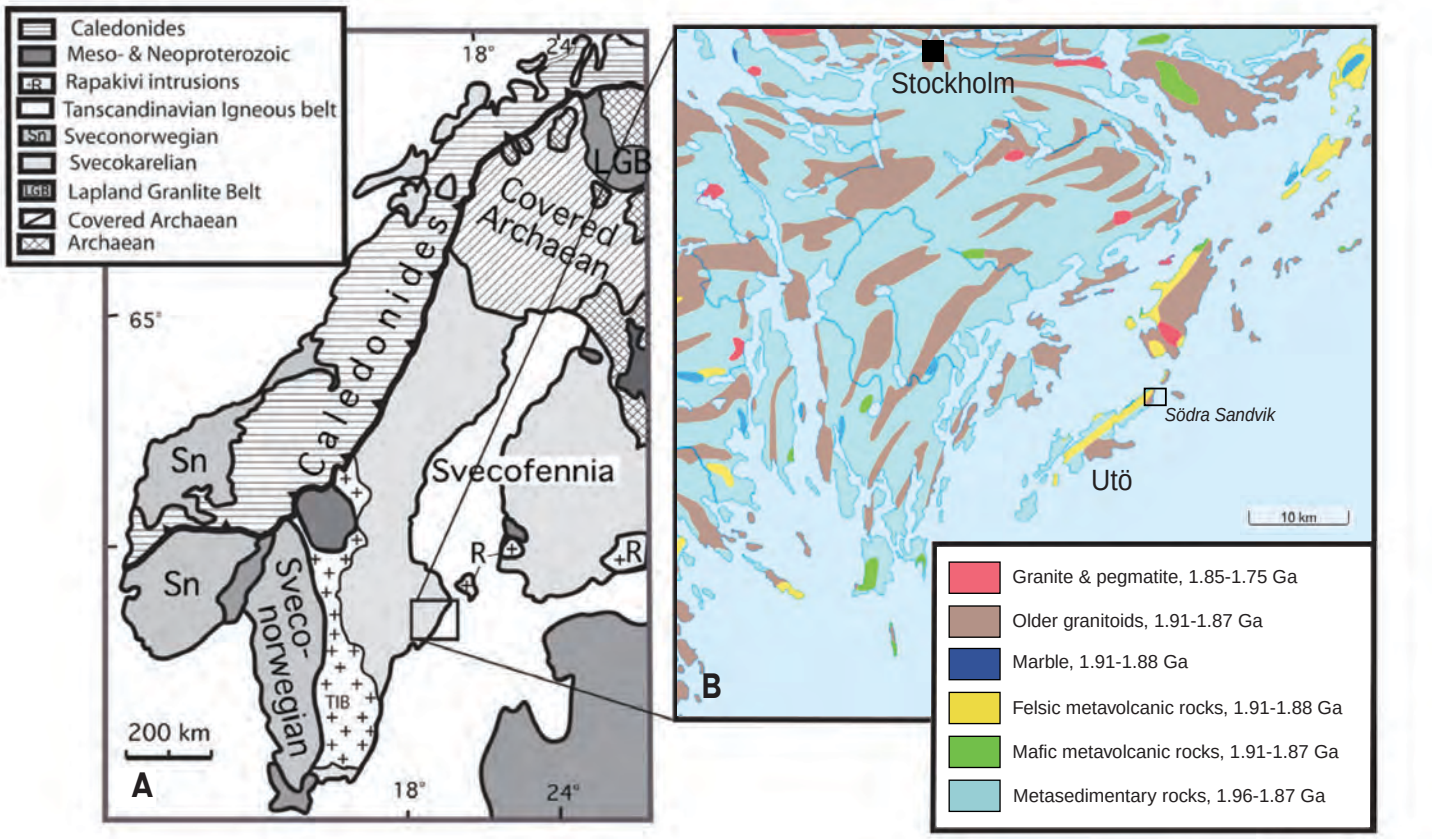

Figure 1 *Location maps:* ***A*** *Tectonic map showing the position of Utö in the Baltic Sea (as published in Talbot 2008).* ***B*** *Geological map of Utö outlining the geographic position of the study area, Södra Sandvik locality, with a black frame (SGU map services: www.sgu.se/kartvisare/).*

Utö holds records of a dynamic marine environment, ranging from shallow shelves to deeper waters (Talbot 2008). The Södra Sandvik locality in the northeastern part of the island is a perfect example of this, it exhibits metasedimentary rocks believed to have been derived from epiclastic sediments (Gavelin *et al.* 1976). This is evident by the presence of both argillite, which is comparable to greywacke, suggesting deposition in deeper marine environments, as well as meta-arenite similar to subgreywackes, which is indicative of shallow water deposition near the wave base (Gavelin *et al.* 1976; Tucker 2011). Additionally, active sedimentary processes at varying depths with sediments sourced from multiple origins are evident in the NE of Utö from the presence of turbidites, mass flow deposits, polymictic breccias, conglomerates and structures such as graded bedding and cross-bedding (Gavelin *et al.* 1976; Talbot 2008). The metasedimentary rocks at Södra Sandvik were deposited in a back-arc basin setting, which influenced the formation of turbidic and volcanoclastic deposits due to volcanic and sedimentary processes that later underwent metamorphism and defromation during Svecokarelian orogenesis (Skelton 2023).

Microbially Induced Sedimentary Structures (MISS) record a wide variety of microbial mat communities across many environments and date back as far as 3.48 billion years ago (Noffke *et al.* 2013). Additionally, a significant environmental event occurred in the Paleoproterozoic known as the Great Oxygenation Event, around 2.3 to 2.1 Ga. This shift fascilitated aerobic microbial metabolism and organic accumulaion in marine settings (El Albani *et al.* 2014; Olejarz *et al.* 2021). The increase in atmospheric oxygen levels, largely due to photosynthetic activity of cyanobacteria, promoted carbonate precipitation and oxygenation of the oceans (El Albani *et al.* 2014). After its formation, Utö likely encountered a relatively stable climate regime around 1.8 - 1.3 Ga, associated with the supercontinent Nuna, characterized by a relatively warm climate without

polar ice sheets. Such conditions as shallow marine environments combined with warm climate and processes like sedimentation and diagenesis would have been favorable to the growth, expansion of microbial life and preservation of calcium carbonate based biotic features (Jellinek *et al.* 2020).
The processes of preservation of early life forms in the geological record, leading to the formation of microbialites such as stromatolites, thrombolites and leiolites, which vary in structure, are influenced by various environmental factors, including microbial activity, sedimentology and geochemical conditions (Dupraz *et al.* 2009). Identifying traces of early life can be difficult, since natural abiotic processes can create structures that closely resemble those formed by biological activity. Thus, examining and understanding the processes that lead to fossilization, including the conditions under which organic matter is preserved or destroyed, is crucial (Javaux & Benzerara 2009).

While the geology of the Södra Sandvik locality has been well documented, the geochemical and biological aspect of its metasedimentary rocks remain mostly unexplored, offering an opportunity for further research. This paper examines a selected outcrop by analysing its geological characteristics as well as the nature of suspected biotic features. The outcrop is a metasedimentary rock that was chosen after initial visual observations at Södra Sandvik locality suggested its potential to contain biotic features (Fig. 2).

Figure 2 *Map showing the position of the study site.*

Compilation of metamorphic pressure/temperature (P/T) from the Svecofennian province of eastern and central Sweden by Skelton *et al.* (2018) points out Utö's complex geological history. The metamorphic field gradient of the province presented by the scholars, including several areas on Utö, exhibits low-medium P/T Buchan metamorphism conditions indicative of crustal growth via volcanic arc accretion. The Svecofennian rocks exhibit a wide range of metamorphic conditions, ranging from greenschist to granulite facies, with amphibolite facies conditions being most common (Skelton *et al.* 2018). The metamorphic nature of the selected outcrop could conceal the biotic features, making it challenging to analyze and identify traces of early life.

Soft-part preservation in ancient life forms is primarily achieved through silica mineralization. This process can also obscure taxonomically important characteristics of microorganisms due to mineral precipitate, revealing only basic morphological details like size, shape and sometimes cellular structures, while potentially masking or destroying others (Konhauser 2007). Additionally, distinguishing biogenic from abiotic structures in ancient metamorphosed rocks can be a challenge that requires a multidisciplinary approach that goes beyond morphology (Javaux & Benzerara 2009; Anderson *et al.* 2023). This paper adopts this approach and combines field observations and sample collection with analytical techniques such as light, fluorescent and scanning electron microscopy coupled with energy-dispersive spectroscopy (SEM-EDS).

This paper proposes a hypothesis that the features observed within the Svecofennian rocks on Utö are of biotic origin. To evaluate the hypothesis a falsification approach is adopted, which considers biotic explanations together with abiotic ones. The goal of the paper is to explore how geological and potential biological processes might have interacted in these ancient rocks to offer an insight into the region's geological past.

2.0 Method

Field Work & Sedimentary Log

During fieldwork a sedimentary log was constructed of an approximately 20 m long outcrop located at the coastal area of Södra Sandvik, with the log documenting a total thickness of 9.38 m. The base of the log was determined by selecting a part of the study area that was coherent and featured continuous stratigraphic sequences, positioned above of a platform-like feature and past a fracture to avoid disruptions in stratigraphy. The log was divided into 4 sections, which were further subdivided into units comprised of several beds (Fig. 3). The units were grouped based on the repetition or similarity of certain sedimentary structures for clarity and simplicity. The units were temporarily marked directly on the outcrop with chalk, which was later removed.

Grain size and mineral composition were analyzed with a 10x hand lens. Due to the metamorphic history of the outcrop the mineral assemblage was analyzed to determine the protoliths. Sedimentary structures were recorded through observation, sedimentary log sketches and photographs for further analysis. The outcrop was carefully studied for identification of potential biotic features, with field sketches created and annotated to highlight certain visual attributes suggestive of biotic origins. Evidence of metamorphism and deformation in the field was documented through photography.

At the end of the week samples were selected and collected from both the beginning and the end of the log. The samples were chosen so that they would not damage the rock face, while still presenting the key features of the area, such as laminations, possible rounded and laminated intraclasts, which may represent microbial mat fragments. Thin sections, 30 µm in thickness, were prepared at Fribourg University in Switzerland.

The log was constructed to interpret the depositional facies of the rocks in the area. Evidence of metamorphism and deformation was gathered through field observations and thin section analysis in order to interpret the conditions that influenced the rocks in the study area.

SEM-EDS Analysis

Laboratory work included SEM-EDS and fluorescence scans in order to explore potential biotic features or minerals that could suggest biotic origin. Philips XL 30 S FEG, a Scanning Electron Microscope (SEM) was used for the SEM-EDS analysis at Fribourg University in Switzerland. The SEM was used to produce high-resolution images of the samples' surface features by scanning them with a focused electron beam, while Energy-Dispersive X-ray Spectroscopy (EDS) provided detailed elemental analysis and mapping. The collected data was exported using AZtec software.

For the SEM-EDS analyses the thin sections were cleared with ethyl alcohol and wiped with non-scratching Chemtronix Coventry tissues. Conductive aluminum tape was applied at four corners with of the samples to create a bridge. The sections were coated with 50 nm carbon to improve electrical conductivity and to avoid electrostatic charge buildup on the surface of the thin sections using a Leica EM ACE600 High Vacuum Coater. A carbon thread was used for coating, with 4 threads loaded to achieve a 50 nm coating. Once the machine reached ultra high vacuum of at least -10^{-8} to 10^{-10} Pa the coating process could begin. The current passing through the threads vaporized the carbon, subsequently evenly coating the section. For optimal performance of the SEM the following settings were applied: the working distance, measured from the highest relief point of the thin section surface to the detector, was set to 8mm, providing optimal angle for X-ray generation and detection during elemental analysis; the accelerating voltage was set to 20 kV; the electron beam was set to 3.5 nA.

During SEM-EDS analysis some challenges were encountered. Despite proper preparation and the 50 nm carbon coating for conductivity, the image quality progressively degraded over time eventually resulting in a static gray image. Beam scattering and signal destabilization were likely caused by the high concentration

of rare earth elements (REE) found in the samples such as uranium (U), thorium (Th), neodymium (Nd), ytterbium (Yb), cerium (Ce) and lanthanide (Ln) etc., along with ilmenite, a magnetic mineral present in the samples. Future studies of similarly challenging samples could explore optimizing SEM parameters by adjusting beam voltage or using alternative conductive coatings to enhance imaging quality.

Some spectra showed rather high Weight% sigma values for some elements, possibly due to the interference mentioned above. Therefore, in order to determine reliability of the SEM-EDS data the standard deviation in absolute % given by the element's Weight% sigma was exported from AZtec software and used to calculate relative error %. A threshold of 0.3% was selected to identify higher uncertainty values. The relative error was calculated for all values greater than 0.3% using the formula: Relative error % = 100 × (Weight% sigma / Weight %). The results are presented in Appendix F3.

Fluorescence Microscopy

For capturing high-resolution imaging of fluorescence signals in order to identify possible organic traces a Nikon Eclipse Ci POL microscope with a Nikon Plan UW 2x/0.06 objective lens equipped with filters for red and green fluorecence imaging and a digital color camera Nikon DS-Ri2 was used. This technique uses specific emission wavelengths of light: blue (420 nm), green (515 nm) and red (590 nm) to excite fluorophores within the samples, causing them to emit fluorescent signals. The images were processed with Nikon NiS-Elements AR software to enhance brightness and contrast. It should be noted that the epoxy resin used to embed the samples contributed to background fluorescence.

Petrographic Microscopy

Petrographical analysis was conducted using a Zeiss - Axio Scope.A1 petrographic microscope equipped with objectives from 5x to 50x at Heidelberg Materials Slite laboratory. The microscope was used to examine mineral assemblage of the samples and to asses fluorescence areas to account for inorganic fluorescence signals during interpretation of data. Photomicrographs were captured using AxioVision SE64 software.

3.0 Data & Interpretations

This part of the thesis consists of multiple sections. Therefore, to ensure readability and coherence interpretations for each section are presented directly after observations. The broader implications of all these findings combined and the hypothesis of this study will be addressed in the Discussion section.

3.1 Features Indicative of Biotic Activity Observed in the Field

The study area at Södra Sandvik is composed of meta-greywacke with well-preserved sedimentary structures such as laminations, ripples, convolute bedding, load casts among others. Some of the features are visually indicative of biotic activity and resemble potential microbial mat structures. Three of these features were depicted in the field sketches and photographs presented in Fig. 3:

- A folded structure with preserved laminations within shown at the center of Sketch A resembles a possible mat roll-up fragment, while the disrupted undulated laminations above the structure could potentially be "irregularly crinkled mat surfaces" (Noffke *et al.* 2022, p. 13).
- Wavy laminations combined with fine darker laminations with preferential thickening over small surface irregularities depicted at the center of Sketch B are also indicative of microbial mat activity.
- Undulated and discontinuous laminations best seen above the central feature in Sketch B resemble sinoidal structures described by Noffke et al. (2022) as dark-colored biofilms covering ripple mark troughs.

The occurrence of cordierites, seen both in the sketches and the photographs in Fig. 3, as well as cordierite-rich concretions at Södra Sandvik (Fig. 6) indicate an iron-rich sedimentary protolith. Possible formation processes and environmental context that influences formation of these features are discussed below.

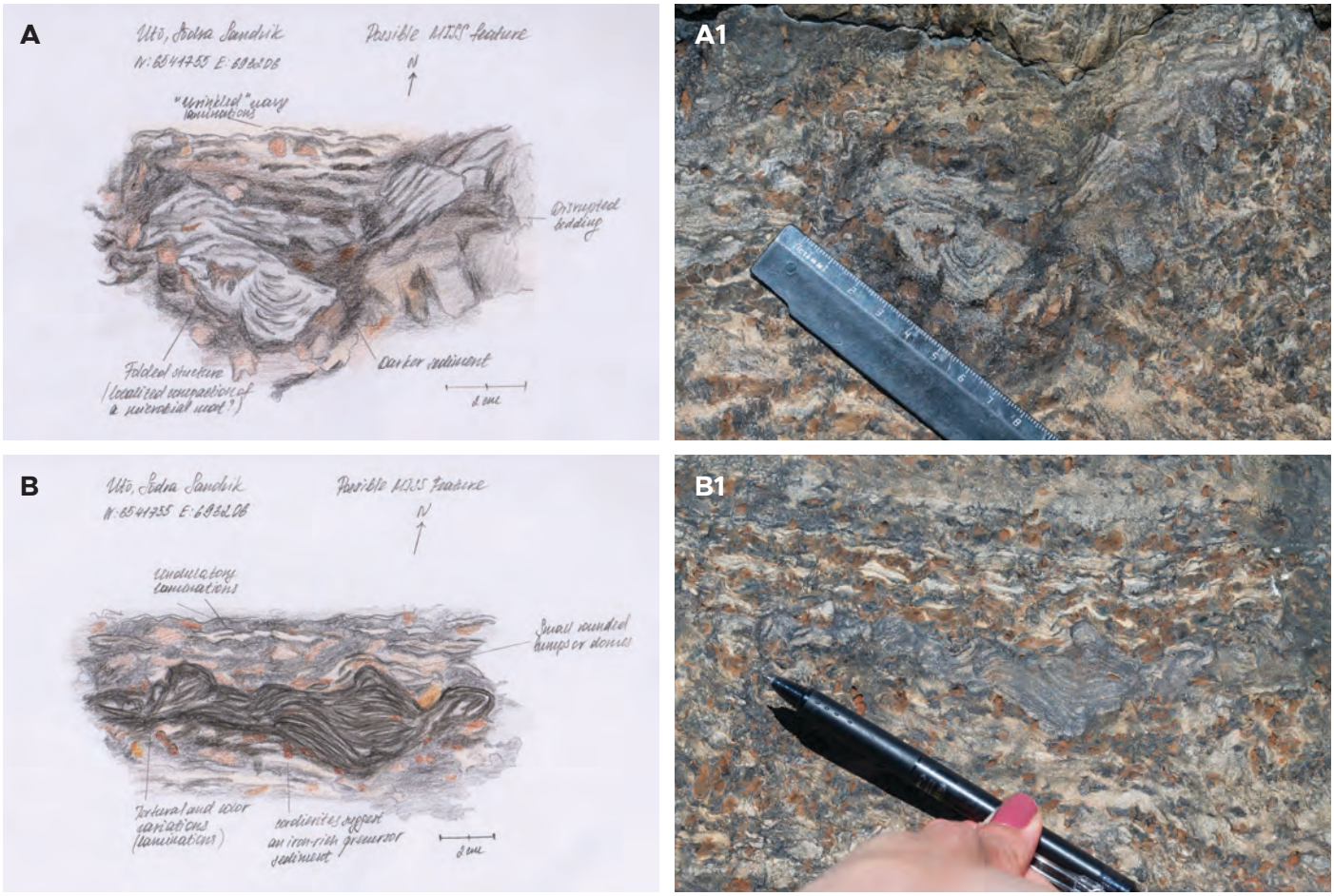

Figure 3 *Field sketches and corresponding photographs of potential MISS at Södra Sandvik:* ***A*** *Wrinkled laminations, disrupted bedding and a folded feature resembling a ripped-up microbial mat.* ***B*** *Wavy laminations with domal structures, textural and color variations indicative of possible MISS.*

Interpretation

MISS are biogenic structures that have a variety of morphologies and in contrast to stromatolites form solely as a result of microbial responses to physical sedimentary processes in most aquatic environments, which leads to biostabilization, sediment trapping and binding of particles (Dupraz *et al.* 2009; Noffke *et al.* 2013). Microbial mats form through the colonization of sediment surfaces by bacteria, which then develop into biofilms and subsequently mature into vertically stratified mats with distinct subsystems. When buried by sediments, microbial mats grow upward to maintain their position near the sediment-water interface and maintain continued access to favorable conditions for growth. Microbial mats can grow at rate of approximately 1 mm per year under optimal conditions over time forming stable structures that accumulate significant organic and mineral deposits (Konhauser 2007). Under specific environmental conditions, microbial mats can induce organomineralization processes by modifying their surrounding environment through the production of exopolymeric substances (EPS), which act as nucleation sites for micrite and other minerals and chemically facilitate carbonate precipitation. Microbial activity stabilizes sediment surfaces and protects them from erosion, forming various characteristic features that may later fossilize under the right conditions (Dupraz *et al.* 2009).

Depending on the environmental conditions, these features can range from microscopic tufts and subtle laminations to more pronounced macroscopic features such as oscillation cracks, shrinkage cracks, roll-ups and mat chips. Other common characteristic structures are wrinkle structures, gas domes, elephant-skin textures, disrupted bedding patterns and laminations. Preservation of these structures typically requires a pause in sedimentation, allowing the structures to become buried before the mat is eroded (Noffke *et al.* 2022). Noffke *et al.* (2022) categorizes MISS structures into five classes based on the main microbial activity that controls the formation of the MISS: structures caused by growth, biostabilization, baffling and trapping, binding and by the interaction of all the mentioned microbial activities. The authors identified 18 main MISS structures.

• Roll-ups or over-flips belong to the biostabilization class and form due to erosion, possibly depicted in Sketch A (central feature). For example, in aquatic environment waves and currents may erode and rip off fragments of microbial mats in a high energy setting, sometimes forming roll-ups up to several meters in scale (Noffke *et al.* 2022). According to Noffke *et al.* (2022), biostabilization includes three types of processes: a response to erosion caused by horizontal water currents, the effects of gas pressure within the sediment and mechanical stress resulting in ductile deformation. The effectiveness of biostabilization is determined by factors such as species diversity, structure and adhesiveness of EPS, salinity, light and other environmental conditions.

• Wavy discontinuous laminations found at the study area (Fig. 3A) could possibly belong to the binding class of MISS which is described as "irregularly crinkled surfaces" (Noffke *et al.* 2022, p. 13). This structure forms when a microbial mat detaches from its surface due to the action of bottom currents. A layer of a microbial mat can form irregular tissue-like folds and quick preservation produces crinkled surfaces that may have tears in the material. A pause in the sedimentation is important for the development of the mat, so that fine-grained fall out can cover the mat surface and become incorporated into the mat fabrics (Noffke *et al.* 2022). Distinct laminated fabrics in microbial mats form due to these recurring disruptions that create pauses in biomass accumulation as a result of variations in sedimentation rate, salinity or seasonality (Konhauser, 2007).

• MISS growth can also include laminae that are generally millimeter to several millimeters in thickness and consist of micrite, peloids and fine skeletal debris, sometimes with layers of cement or sand, possibly depicted in Sketch B (central feature). The microbial origin is indicated by small corrugations and undulations and preferential thickening over small surface irregularities. The laminae can be disrupted and exhibit broken, overturned and folded structures due to the expansion of the microbial mat (Tucker 2011).

• Reticulate patterns comprised of centimeter to millimeter-scale ridges and tufts, which result from mi-

grating trichomes and can spread over vast areas of microbial mats belong to the binding class of MISS. This class is defined as an arrangement of a microbial colony into a biofilm or microbial mat and is only controlled by sedimentary parameters, while no biomass accumulation is involved (Noffke *et al.* 2022). The continuous wavy laminations above the central feature in Sketch B could possibly represent these structures.

The Fe enrichment at Södra Sandvik could have resulted from microbial activity or diagenetic processes within an oxygen-poor depositional environment. Microbial mats act like sponges for cations, and when dominated by Fe(II)-oxidizing bacteria, for example, Beggiatoa, they can trap and bind Fe(III) minerals. Microbial EPS act as binding agents and facilitates the precipitation and accumulation of ferric hydroxides ($Fe(OH)_3$) and other Fe-enriched minerals in the mat layers, contributing to the geochemical composition of the rock. Microbial activity also creates microenvironments that enhance the geochemical cycling of elements like Fe and associated trace elements such as REEs, which can adsorb onto Fe(III) hydroxides or oxides precipitated through microbial processes, subsequently resulting in REE enrichment in sediments (Konhauser 2007).

Modern analogues of MISS are able to survive in a variety of environments such as tidal flats, shallow marine zones, continental settings, anoxic basins and hypersaline systems and are resistant to high energy events (Noffke *et al.* 2022; Konhauser 2007). In high-energy settings such as tidal flats microbial mats can persist under waves and currents but may become ripped up, forming disrupted bedding and roll-ups. In low energy settings laminated or clotted textures form. Fossil microbial mats can be observed in both siliciclastic and carbonate settings: carbonaceous banded cherts or interbedded with volcaniclastic sandstones, siltstones and quartz-rich sandstones. According to Tucker (2011), MISS are commonly found in Precambrian sandstones, since there were no grazing or burrowing organisms disrupting the mat at the time.

However, wrinkled patterns in clastic sediment and described above structures do not always indicate biologically induced patterns. There are many non-biological mechanisms of formation that include, for example, millimeter-sized ripple marks created by rapid water motion in shallow water depths, deformation of semi-consolidated material by slumping or by ball and pillows structures or load clasts, tectonic crinkling or diagenetic processes (Noffke *et al.* 2022). Distinguishing biotic from abiotic structures requires broader environmental context, which will be explored further in the next section through an analysis of the sedimentological log and interpretation of depositional facies of the study area.

3.2 Sedimentary Log and Depositional Facies

A notable characteristic of the outcrop is its well-preserved stratification, which is the focus of this section. According to Tucker (2011), greywacke is a hard sedimentary rock of light to dark grey color with high matrix content and lithic grains. Field observations showed that the lighter layers of the outcrop are composed of silt to fine grain-sized sandstone interlayered with frequent darker biotite-rich layers derived from mud-rich matrix. The original sorting and the presence of lithic grains are difficult to determine due to locality's metamorphic history. The protolith was likely a poorly sorted greywacke with an abundant mud and clay matrix. Therefore, the lithology of the entire outcrop in the log has been categorized as meta-greywacke. According to field measurements the beds are dipping ca 23-25° to the northeast, indicating post-depositional tectonic processes. The grain size in the log was categorized as fine sand, since quartz grains range from silt to fine sand in size and biotite crystals were originally derived from mud. Grain size or crystal sizes in this case for each section of the log are documented with photographs taken through a hand lens and provided in Appendix B. Several images were taken for each part of the log. Since the grain size and sorting were consistent across the sections, only a few images were chosen to represent each section. Correlating photographs for each unit are also provided in Appendix B. The photographs' numbers are listed in the first column of the log followed by the section and the unit number. An overview of the outcrop is provided in two photographs in Fig. 4, showing the starting part of the sedimentary log (A) and its continuation to the end of the logged sequence (B). The outcrop correlation sketch (Fig. 5) illustrates how the log was divided into four sections and corresponding numbers of units, making it easier to read the log and correlate the sections and the units with Figure 4. A larger landscape-format of this figure is available in Appendix A.

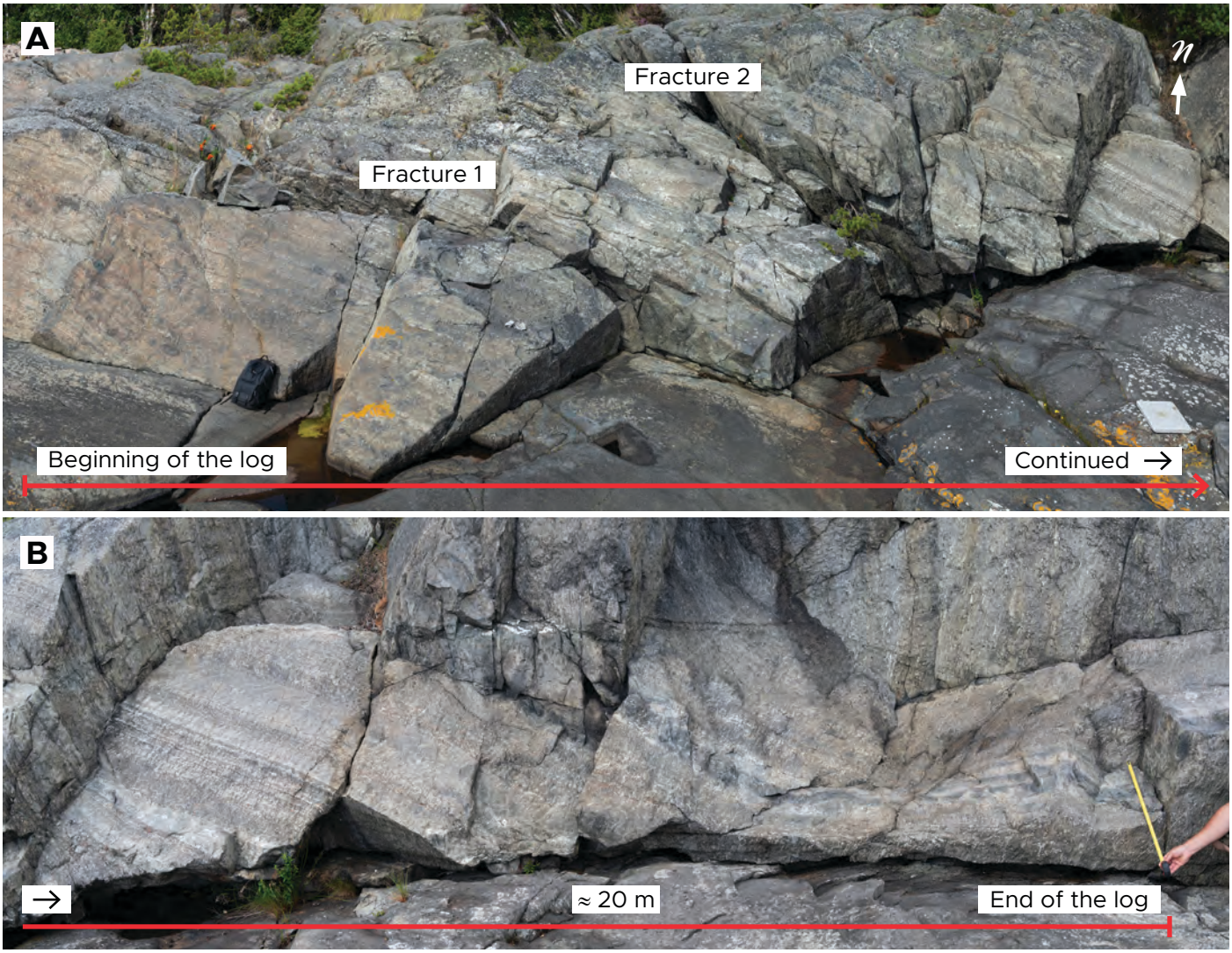

Figure 4 *An overview of the site:* **A** *The first part of the outcrop.* ***B*** *The continuation and the end of the outcrop.*

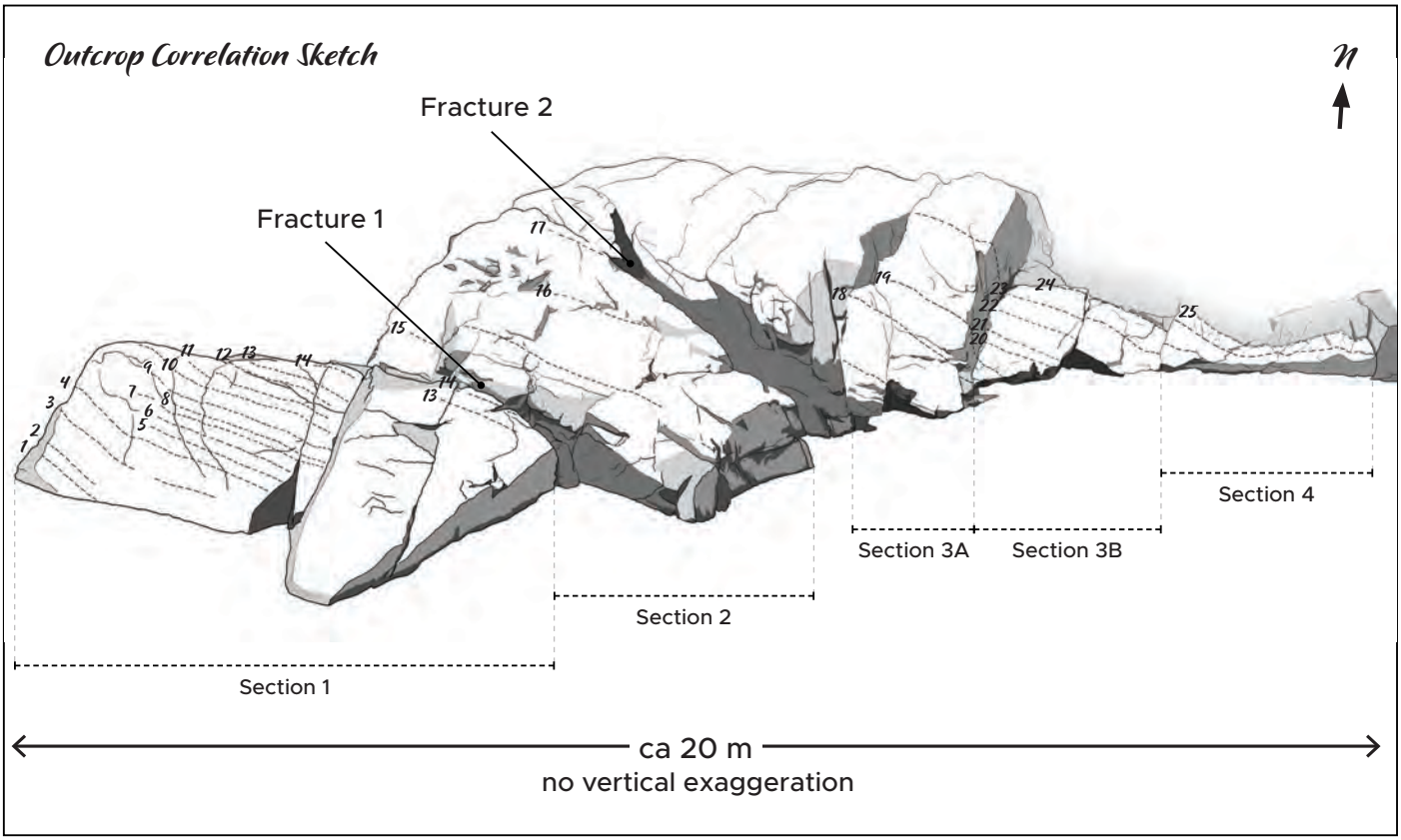

Figure 5 *Correlation sketch of the outcrop showcasing the four sections and the units into which the log was divided for easier referencing when reading the log.*

Location:	Formation:	Coordinates:	Date:	Sheet No.
Utö, Södra Sandvik	*Lower, "Greywacke lens"*	*N: 6541755 E: 693206*	*28/7 - 2/8 - 2024*	*1/3*

Continued on the next page →

Image reference *(in the attachments)*	Section number	Bed/ unit number	Bed/ unit thickness (cm)	Lithology	Grain size (Mud; Sand: vf, f, m, c, vc; G)	Sedimentary structures & other features	Palaeocurrents	Color	Remarks
013 014 015 016	***2***	*15*	*80*					*Light to dark grey, rusty patches*	*Possible load clasts (image 014), unevenly distributed. Directly after there is rather planar bedding best defined directly after the fracture, cordierites present along the darker bedding planes (Image 015). Fractures.*
					f				
010		*14*	*26*					*Beige to light grey, rusty patches*	*Ca 6 cm convolute bedding at the bottom of the unit. Homogeneous bed. The first section ends with unit nr.14. Fractures and weathering.* *Images 011 and 012 in Appendix B showcase grain sizes for Section 1.*
009		*13*	*19*					*Beige to light grey, rusty patches*	*Thicker ca 5 cm convolute bedding at the lower part of the unit with overlaying homogeneous bedding and thin wavy laminations on top.*
009		*12*	*19*					*Beige to light grey, rusty patches*	*Thin to medium laminations, some discontinuous with possible convolute laminations on top.*
008		*11*	*21*					*Beige, light to dark grey, rusty patches*	*Ca 2 cm of thin discontinuous laminations with a diffuse boundary capping a homogeneous bed with convolute bedding below.*
008		*10*	*15*					*Beige, light to dark grey, rusty patches*	*Thicker ca 9 cm wavy to corrugated laminations deformations capping a homogeneous bed with convolute bedding below.*
008		*9*	*13*					*Beige, light to dark grey, rusty patches*	*Homogeneous bed capped with ca 4cm medium wavy laminations, no balls and pillows.*
008		*8*	*12*					*Beige, light to dark grey, rusty patches*	*Ca 5 cm laminations overlying a homogeneous bed with Incipient balls and pillows.*
007		*7*	*14*					*Beige, light to dark grey, rusty patches*	*Ca 5cm layer of medium to thick laminations overlying pronounced and abundant balls and pillows.*
007		*6*	*17*					*Beige, light to dark grey, rusty patches*	*Convolute bedding with balls and pillows, up to 15cm capping 1 homogeneous bed.*
006		*5*	*19*					*Beige, light to dark grey, rusty patches*	*Three sets of wavy laminations capping 3 homogeneous beds. Small 1-2 cm balls and pillows.*
004 005		*4*	*34*					*Beige, light to dark grey, rusty patches*	*Lower part is heterolithic. Thin continuous laminations. Undulating thin >3 beds with discontinuous non parallel laminations within. Convolute bedding is observed in the upper section of the unit.*
003		*3*	*30*					*Beige, to dark grey with rusty patches*	*The unit is heterolithic in the lower part. Medium from 1-2 mm to ca 3-4 mm laminations and poorly defined thin laminations within. Discontinuous, likely due to cordierite-bearing bands.*
002		*2*	*17*					*Beige, to dark grey with rusty patches*	*Disrupted convolute laminations present in the lower grey bed, indicating soft-sediment deformation.*
001	***1***	*1*	*23*					*Beige to dark grey with rusty patches*	*Very thin beds >1-2 cm. Variations of composition of thin to very thin laminations within beds. Localized soft-sediment folding.*

Legend

- Meta-greywacke
- *f* Fracture
- Fractured surface
- Homogeneous unit, no distinctive features
- Planar bedding
- Undulated wavy laminations
- Discontinuous laminae, composition variations
- Discontinuous wavy laminae, composition variations
- *Load clasts*
- *Pseudonodules*
- *Convolute laminae*
- *Convolute bedding*
- *Flame structures*
- *Balls & pillows*
- *Water-escape structures*
- *Slump structures*
- *Unidirectional current ripples*
- *Climbing ripples*
- *Concretions*
- **Contact:**
- *Sharp, regular*
- *Sharp, irregular*
- *Gradational*

 Scale: 1:12.86

Location:	Formation:	Coordinates:	Date:	Sheet No.
Utö, Södra Sandvik	*Lower, "Greywacke lens"*	*N: 6541755 E: 693206*	*28/7 - 2/8 - 2024*	*2/3*

Image reference *(in the attachments)*	Section number	Bed/ unit number	Bed/ unit thickness (cm)	Lithology	Grain size (Mud, vf, f, m, c, vc, G)	Sedimentary structures & other features	Palaeocurrents	Color	Remarks
025	**3A**	*18*	*100*					*Light to medium grey, some rusty patches*	*Slightly more prominent concretions. Load clasts. Medium-sized laminations.* *Massive slump structures.* *Massive grey bed on top of a homogeneous bed with subtle irregular laminations and small-scale folding or soft-sediment deformation. Minor fractures and quartz encrustations.*
013 *018* *019*		*17*	*70*	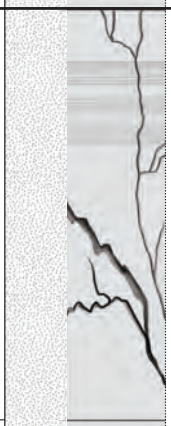				*Light grey, very few rusty patches*	*2 sets of planar bedding with darker very fine laminations within. Smaller weathered cordierite voids.* *Fractured surface, quartz encrustations, quartz veins. The lower sections appears homogeneous and transitions into planar and faintly laminated structure bedding.* *Images 020, 021 and 022 in Appendix B showcase grain sizes for Section 2.*
013 *017*		*16*	*130*			*Surface quartz encrustations and veins*		*Light to medium grey, some rusty patches* *Light to medium grey*	*3 sets planar bedding with very fine darker laminations within.* *Mostly fractured surface, weathered covered with lichens and thin white quartz encrustations. Indistinct laminations appear sporadically.* *Quartz incrustations on the surface and veins, smaller weathered concretions, no rusty color.*
013 *014* *015* *016*	**2**	*15*	*80*			*Quartz veins*		*Light grey, rusty patches*	*Quartz veins. Weathered surfaces with quartz incrustations have masked sedimentary structures. Weathered voids from concretions. The color is n longer rusty or beige color. Fractures. A large structure similar to a large ball and pillow capped almost planar less defined beds with weathered cordierite voids.*

f

Legend

- Meta-greywacke
- *f* — Fracture
- Fractured surface
- Homogeneous unit, no distinctive features
- Planar bedding
- Undulated wavy laminations
- Discontinuous laminae, composition variations
- Discontinuous wavy laminae, composition variations
- *Load clasts*
- *Pseudonodules*
- *Convolute laminae*
- *Convolute bedding*
- *Flame structures*
- *Balls & pillows*
- *Water-escape structures*
- *Slump structures*
- *Unidirectional current ripples*
- *Climbing ripples*
- *Concretions*

Contact:

- *Sharp, regular*
- *Sharp, irregular*
- *Gradational*

 Scale: 1:12.86

Location: Utö, Södra Sandvik	Formation: Lower, "Greywacke lens"	Coordinates: N: 6541755 E: 693206	Date: 28/7 - 2/8 - 2024	Sheet No. 3/3

Image reference (in the attachments)	Section number	Bed/ unit number	Bed/ unit thickness (cm)	Lithology	Grain size (Mud | Sand: vf, f, m, c, vc | G)	Sedimentary structures & other features	Palaeocurrents	Color	Remarks
End of the log			*932 cm*						
040	***4***	*25*	*26*			*Quartz veins*		*Light to medium grey*	*Banded layers with subtle color changes (variations in sedimentary composition), load clasts, pseudonodules.* *Image 041 in Appendix B demonstrate grain sizes in Section 4.*
037 040		*24*	*50*						*A unit with slightly smaller ball-and-pillows and convolute structures.* *Discontinuous wavy laminations.* *Water-escape structures (dewatering pillars).* *From a couple cm to 15-20cm in size ball-and pillows.* *Images 037, 038 and 039 in Appendix B demonstrate grain sizes in Section 3B.*
036		*23*	*45*				→ →	*Light to medium grey*	*Larger continuous ripples. Remnants of ripple crests are stretched and slightly smoothed over, possibly by slow wave action that flattened them while depositing a fine layer. Water-escape structures (dewatering pillars).* *Ca 3 cm ripples.* *Load clasts on top of a homogeneous bed.*
034 035		*22*	*32*				→ →	*Light to medium grey*	*2 larger ripple sets 4-6cm on top with increased amplitude (a higher-energy depositional environment/shift in current strength).* *3 sets of ripples, approx. 3 cm at the crest.* *Ca 5 cm of climbing ripples.*
033		*21*	*27*					*Light to medium grey*	*Homogeneous bed with no visible laminations in the lower part of the unit. Irregular undulating contact and a darker color may indicate changes in sediment composition in the upper bed.*
032		*20*	*23*					*Light to medium grey*	*Parallel continuous wavy laminations with subtle flame structures capping a homogeneous unit with minor color variations.*
026 027 028 029	***3B***	*19*	*70*					*Darker grey matrix with light grey balls and pillows and convolute laminations*	*This unit is characterized by very prominent, massive ball-and-pillow structures transitioning into convolute laminations with possible incipient ball-and-pillow structures or load deformations in the middle section. Additional large ball-and-pillow structures overly the unit.* *Images 030, 031 and 032 in Appendix B illustrate grain sizes in Unit 19.*
		18	*100*					*Light to medium grey, rusty patches*	*Bedding appears homogeneous, thin quartz veins, weathered surface, capped with incipient load clasts and small, several centimeters in size ball-and-pillows.* *Images 023 and 024 in Appendix B showcase grain sizes in Section 3A, Unit 18.*

Legend: Meta-greywacke; *f* Fracture; Fractured surface; Homogeneous unit, no distinctive features; Planar bedding; Undulated wavy laminations; Discontinuous laminae, composition variations; Discontinuous wavy laminae, composition variations; *Load clasts*; *Pseudonodules*; *Convolute laminae*; *Convolute bedding*; *Flame structures*; *Balls & pillows*; *Water-escape structures*; *Slump structures*; *Unidirectional current ripples*; *Climbing ripples*; *Concretions*; **Contact:** Sharp, regular; Sharp, irregular; Gradational

 Scale: 1:12.86

The sedimentary log documents a sequence of meta-greywacke characterized by well-preserved sedimentary structures including laminations, ripples, convolute bedding, slumps, ball-and-pillow structures among other features. The outcrop shows a transition from a rusty iron-rich zone in the beginning of the log, where cordierites are most abundant, to a grey colored zone to the right side of the logged area with fewer cordierites.

Section 1

Section 1 of the log features mostly wavy laminations fine to medium in thickness (ca 0.1 - 0.6 mm), convolute laminations and ball-and-pillow structures from incipient to several centimeters in size. This section features a beige to rusty color interlayered with darker laminations in contrast with predominantly grey tones of the subsequent sections. The sandstone beds are fine-grained and are interbedded with rich in biotite laminations. Section 1 contains the highest concentration of concretions, also called nodules, which gradually decrease in number through the logged sequence (Fig. 6). The concretions contain cordierite bearing zones mostly along the outer edges, while the darker areas are primarily composed of biotite.

Section 2

Section 2 follows the first fracture and starts with a relatively thick unit of dark grey beds measuring approximately 80 cm and features cordierites along the darker bedding planes. In this section color transitions to predominantly grey. This part of the log was challenging to document due to fractures, weathered surfaces and quartz encrustations concealing details. The remaining part of the section is mostly homogeneous, although there may be a potential ball-and-pillow structure present (Appendix B, image 016). Several planar 3-4 cm in thickness beds with very fine dark laminations are present on top of the homogeneous unit (Appendix B, images 017-019). Several concretions were observed in Section 2, much less than in Section 1.

Section 3A and 3B

Section 3A consists of Unit 18 (Appendix B, image 025). Unit 19 is present in both Sections 3A and 3B, but since it extends to the beginning of Section 3B, it was recorded as part of Section 3B. 3A begins with large overturned slump structures and convolute laminations. Load clasts are also present.

Section 3B is notable for its remarkably well-preserved sedimentary structures including very distinct ball-and-pillow structures and several sets of ripples. At the start of the section massive ball-and-pillow structures, up to 40cm in size (Appendix B, images 026-029), as well as convolute laminations set in dark grey matrix can be seen. There are distinct colour transitions between light and dark grey colors. Possibly the most notable features in this section are the ripple sets, ranging from about 2 cm to about 4 cm in height and from ca 4 cm to 5 cm in length. All sets of ripples exhibit asymmetry with gentle stoss sides and steeper lee sides. The paleocurrent direction is oriented from the southwest to the northeast for all sets of ripples. Other features in the Section 3B include load clasts, water escape structures, climbing ripples and large ripple-shaped structures with stretched tops embedded into overlaying darker sediments, possibly elongated

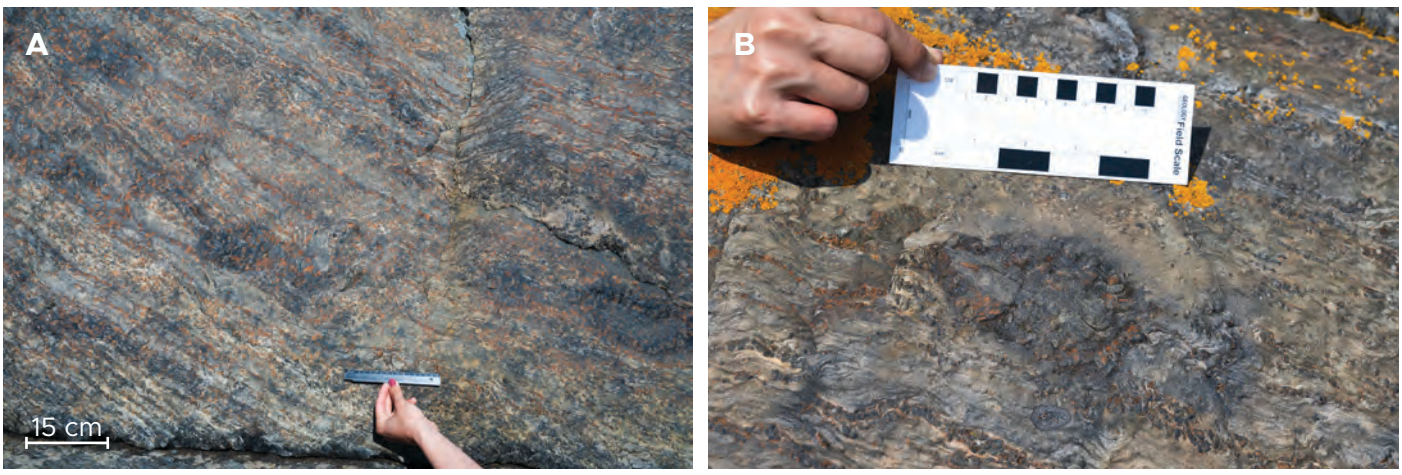

Figure 6 *Concretions found in Section 1:* ***A*** *Several darker round features with rusty cordierites along the edges represent concretions.* **B** *A close-up of a single concretion with a lighter depletion area above the feature.*

by a current flow, also consistent with the northeastern paleocurrent direction (Appendix B, image 036). The number of concretions is decreasing in this section.

Section 4

The beds in Section 4 are near planar beds and exhibit gradational change from lighter to darker grey color (Appendix B, image 040). The contact along these transitional boundaries resembles load clasts. No concretions were observed in this section.

Interpretation

The higher concentration of cordierite in the rust-colored section in the beginning of the logged area suggests higher iron content in the original sediment transitioning into the lower content in the grey-colored sections. Cordierite minerals indicate the effects of post-depositional metamorphism not original depositional processes. Key features observed in the outcrop that provide insight into the depositional processes and environmental conditions at the time of sedimentation are described and interpreted below.

Sediment Instability and Deformation Features

• Convolute bedding often forms from deformation processes such as shearing from currents or frictional drag from moving sand, where lamination become distorted and create irregular asymmetric features without specific orientation. It is linked to dewatering processes (fluidization and liquefaction) and associated with synsedimentary fault and seismic activity (Tucker 2011).

• Load clasts, including ball-and-pillow structures, commonly occur at the base of sandy turbidite beds or when sand is deposited directly on top of wet mud, resulting in unstable conditions due to higher density of sand overlying water-saturated mud with a lower density. The sand then partially sinks into the mud, forming rounded bulbous structures pushing the mud up. Overtime some sand masses may become isolated within the muddy layer creating prominent load balls (Nichols 2023).

• Slumps are structures that often exhibit folding, including recumbent folds, asymmetric anticlines and synclines and thrust folds. A common trigger for the features are earthquake shocks (Tucker 2011).

• Water escape structures observed in the outcrop resemble vertical escape pipes, which form when excess water is expelled from sediment during dewatering due to fluid pressure changes (Appendix B, image 034). These structures are associated with fluidization and liquefaction. Fluidization occurs when increased pore pressure causes sediment grains to lose cohesion and behave like a fluid, while liquefaction occurs water-saturated sediment temporarily loses its strength and stability. These processes are often triggered by earthquake shocks and linked to synsedimentary fault movements (Tucker 2011).

All the mentioned above features are present in all 4 sections, although not all are present in every section. These features are influenced by gravity-driven processes and can be triggered by similar events such as seismic activity, for example, earthquake shocks, sediment loading and rapid deposition (Nichols 2023). Their presence throughout the log suggests deposition with episodes of instability.

Flow Energy and Ripple Characteristics

• Change in color from grey or darker tones within laminations as well as within the units suggest higher content of lithic grains and finer mud-rich sediments. Laminations primarily form through sedimentation from suspension or low-density turbidity currents (Nichols 2023). An example of such a change can be observed in Section 2, where it is reflected by the homogeneous unit and planar 3-4 cm in thickness beds with very fine dark laminations on top. This change indicates a shift towards much calmer depositional conditions compared to Section 1.
• The ripples height and asymmetry (about 2 - 4 cm in height and 4 -5 cm in length) in Section 3B are in-

dicative of current ripples (Baas 1978; Nichols 2023). A set of 5 well-preserved ripples from this Section was measured to calculate Ripple Index (RI) and Ripple Symmetry Index (RSI) to identify the type of the ripples. The way the ripples were measured and calculated can be seen in Appendix C (Fig. C1 - C3). RI is calculated as a ratio of ripple wavelength to its height. The RI for the set measures from 1.11 to 1.40 with an average value of 1.29. While RI is used to distinguish between ripple types, these values are too low compared to the typical ranges of: 4-16 for wave-formed ripples, 8-20 for current and 30-70 for wind ripples provided by Allaby (2020). Although RI is not conclusive for identifying ripple type in this case, Tanner (1967) states that values below 15 mark the threshold between eolian and subaqueous ripples, pointing to subaqueous depositional origin. RSI is calculated as a ratio of the stoss side of the ripples to its lee side length and ranges from 1.96 to 3.6 with the mean value of 2.63, suggesting current rather than wave ripples, which generally have values lower than 2.5 (Alaby 2020). Current ripples form at lower limit of sediment transport conditions in relatively low-energy environments with unidirectional flow. They are often associated with intertiadal flats, turbidites and sandy rivers (Baas 1978). Nichols (2023) states that the formation of ripples is influenced by processes within the viscous sublayer and is not dependent on water depth, which allows current ripples to develop in water depths ranging from a few centimeters to several kilometers. Climbing ripples present in the same section suggest high rate of deposition (Allaby 2020). Section 3B ripples are indicative of relatively low-energy current-dominated environment with consistent unidirectional flow, evidenced by the NE-oriented paleocurrent direction of all ripple sets.

Concretions

The origin of concretions observed at the Södra Sandvik outcrop remains debated. Talbot (2008) classifies these dark grey concretions with diffuse edges as "second generation" concretions, which can incorporate not only first generation concretions but also other clasts, for example, vein quartz, that were already compacted and deformed during earlier phases of sedimentation and tectonic activity. They can also grow independently under new diagenetic conditions during tectonic reworking and sediment recycling in the accretionary prism. The first generation concretions (not observed at the study site), according to Talbot (2008), formed in unlithified sediments, while the second-generation concretions formed post-depositionally in lithified sediments and may not incorporate first-generation concretions. Thus, according to Talbot's theory they cannot be used to interpret the depositional facies of the locality, but rather serve as evidence of fluid activity and localized redistribution of iron and other elements during uplift in the accretionary prism.

However, Skelton (2023) describes these concretions as forming in soft sediments, potentially as a result of early diagenesis and microbial activity, suggesting that their occurrence alongside ferric precipitation could indicate a link to photosynthetic cyanobacteria and chemical precipitation processes. If these concretions indeed formed during early diagenesis, their presence in the logged outcrop would suggest that they formed in shallow, permeable sediments under warm conditions, where iron-rich groundwater facilitated their precipitation (Nichols 2009; Allaby 2020), in moderately deep and low energy environment with low sedimentation rates, since dynamic and anoxic conditions can hinder growth or dissolve existing concretions (Kaikkonen *et al.* 2019).

Modern studies of ferromanganese concretions in the Baltic Sea suggest that concretions need stable and low energy environment to form with depths of 40-100 m. Although concretions can occur in shallower or deeper waters under right environmental conditions. Formation of concretions mostly occurs in oxic conditions as anoxic or hypoxic conditions can lead to the dissolution of Fe-Mn concretions, often on slopes, near depressions or on seabed elevations (Kaikkonen *et al.* 2019). However, the Paleoproterozoic conditions at Södra Sandvik may have differed from the ones described by Kaikkonen *et al.* (2019). Concretion growth is also influenced by changes in pH, oxygen availability, salinity and microbial activity, which lead to precipitation of iron. In sandstone iron can diffuse through the rock and precipitate around nucleation sites, resulting in spherical or layered structures, often with surrounded by lighter depleted of iron "halos", which indicate localized reactions and fluid migration during cementation (Fig. 6B).

Depositional Facies

The study area represents subaqueous depositional environment and resembles a part of a turbidite system, which was influenced by occasional higher energy events and seismic activity. The consistent grain size throughout the outcrop possibly indicates a consistent sediment source over time. The absence of coarser sediments, scoured surfaces or cross-bedding supports medial to distal sediment source (Nichols 2023).

Sedimentary structures described in Sections 1-2 align with Tb-Tc divisions of the Bouma sequence, typical for medial to possibly distal settings (Nichols 2023, p.124). Load clasts and incipient ball-and-pillow structures indicate episodic instability within a low-energy depositional environment, consistent with deeper medial to distal turbidites (Nichols 2023). Ripples are often found in the Tc division of the Bouma sequence, deposited under moderate flow velocities. Climbing ripples generally indicate deposition by turbidity currents through simultaneous suspended load fallout and bedload transport sedimentation (Jobe *et al.* 2012), when the rate of sediment transport is higher than the rate of the downstream migration of a ripple (Nichols 2023). The planar bedding in Section 4 could be representative of Td division.

The decreasing abundance of concretions across the outcrop, the presence of slump structures and large ball-and-pillow structures together with several ripples sets in Section 3B suggest a transition to downslope conditions, consistent with Talbot's (2008) interpretation of the area as a transitional zone between a continental shelf and a canyon with a slope deepening toward NE. According to Nichols (2003), proximal to distal turbidites can from 10s to 100s of kilometers, distances that can occur on continental shelves. Based on these interpretations, the maximum depth at which the sediments were likely deposited would correspond to the maximum depth of a continental shelf, which ranges from 100 to 200 meters in general, based on modern environments (Encyclopaedia Britannica n.d.). Additionally, if the concretions formed during early diagenesis, their presence further suggests that deposition occurred in a stable, low-energy setting, possibly within a depth range comparable to modern ferromanganese concretions in the Baltic Sea of approximately 40–100 m. (Kaikkonen *et al.* 2019).

3.3 Evidence of Metamorphism and Deformation

Field Observations of Metamorphism and Deformation

A variety of features observed during field work were recorded as evidence of metamorphism and deformation at Södra Sandvik. These observations provide an insight into the metamorphic history and tectonic processes that shaped the outcrop after its deposition (Fig. 7A).

• Several boudins were found at the study area (Fig. 7 B-D). The rock surrounding boudin number two, observed in Fig. 7 C and D, is plastically deformed and shows clear foliated texture. Additionally, while the boundary between the competent material and the host rock is sharp in Fig 7B, the matrix around the boudin in Fig. 7 C-D shows partial quartz redistribution.

• Joints, parallel diagonal cracks cutting through the rock, can be seen in the lower right part of Fig. 7A. Additionally, a set of fractures can be observed in the lower central part of the same image. These features can be found throughout the whole study area and are especially prominent in the same area as the veining.

• Other features observed in the study area are quartz-filled veins. Several meters long quartz-filled veins are shown in Fig. 7E. Cross-cutting quartz veins are presented in Fig. 7F. While Fig. 7G displays a particularly interesting vein. This vein has a curved shape and exhibits deformation with similar direction to the elongated and horizontally aligned light-colored foliated crystals surrounding the vein (Fig. 7H). Some of the veins found at the site show rusty coloration due to iron oxidation similar to the vein in Fig. 7G. However, the host rock around the veins shows no significant alteration.

• Not in the immediate vicinity of the logged sequence but approximately 15-20 meters west two recumbent folds facing each other can be observed (Fig. 7I). Their axes are oriented towards the center where the bedding becomes vertical. A near-horizontal axial plane in Fold 1 can be seen in Fig. 7J. The fault that is observed in the middle of the vertical bedding is marked with a white dashed line in Fig. 7I. Additionally, potential minor folding can be observed starting from the logged part of the study area and continuing to the in the right part of Fig. 7A. The logged part of the outcrop is marked with a solid line and the continued dashed line marks potential folding.

• The study area is rich in cordierite, which is a diagnostic mineral for metamorphic grade and compositional variations. Rusty-colored minerals or in some cases voids, where the mineral has weathered away, can be seen throughout the whole outcrop (Fig. 6K).

• The presence of biotite and its preferred orientation can also be used as an indicator of a metamorphic overprint (Fig. 7O). Additionally, phyllitic metapelite outcrop (Fig. 6L) with distinct phyllitic texture and slight sheen is located within approximately 5 m of the logged section.

• Another notable feature that serves as an evidence of deformation and metamorphism is crenulation cleavage, which is a secondary foliation formed by the microfolding of pre-existing foliation and was observed just east of the logged outcrop (Fig. 7M-N).

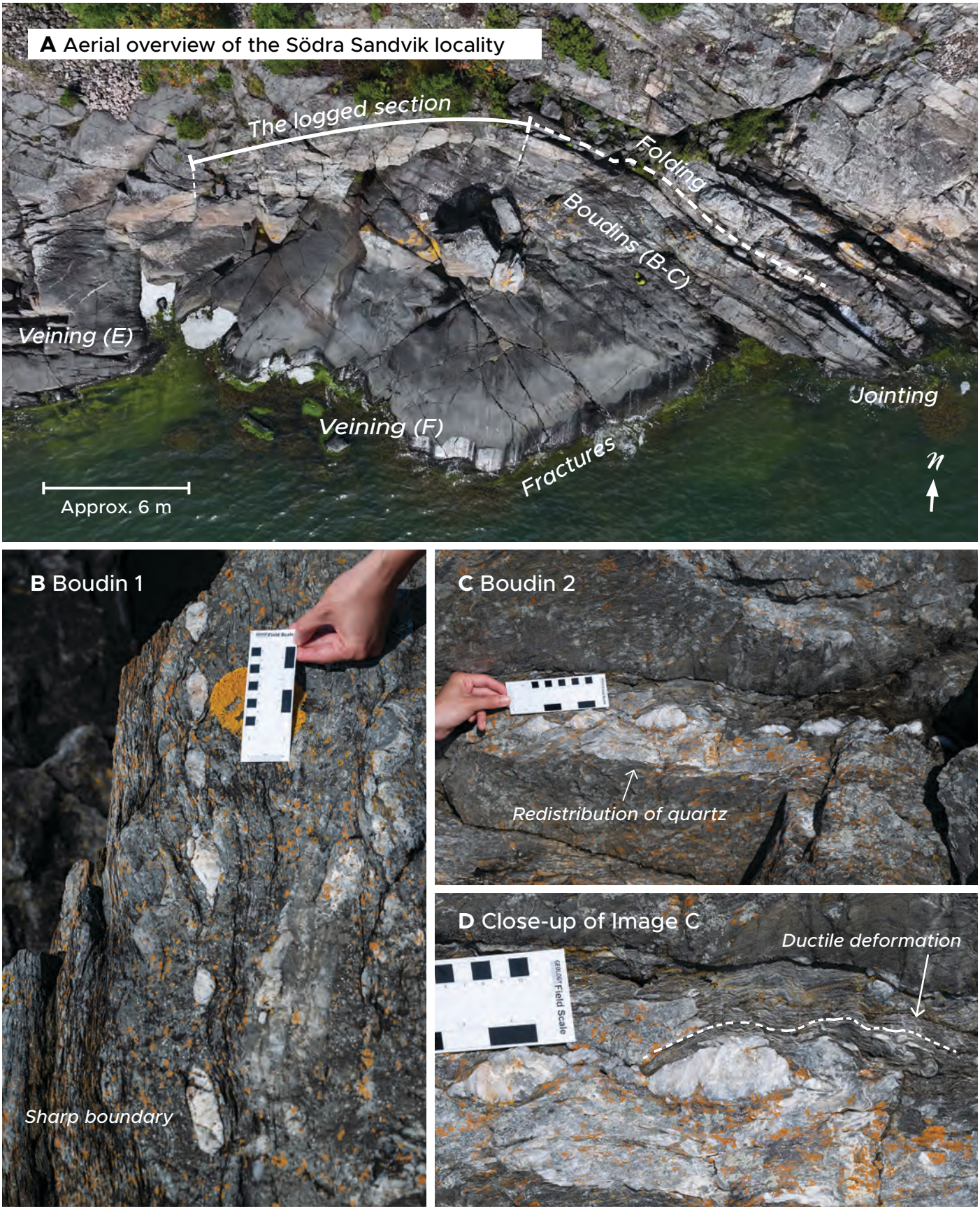

Figure 7 *shows evidence of metamorphism and deformation observed in the field:* ***A*** *Areal view of the Södra Sandvik outcrop provides an overview of deformation features found at the study area such as fractures, jointing, potential folding, veining and boudins. The letters in parentheses correspond to photographs of some of the features provided in this figure.* ***B-D*** *Two boudins formed from competent quartz-rich material surrounded by plastically deformed metapelite.* ***B*** *shows sharp boundary between quartz that may have been a part of a larger layer that deformed into the boudin structure within the host rock.* ***C*** *shows partial quartz redistribution during deformation, with some quartz being moved into the surrounding matrix.* ***D*** *A close-up of the plastic deformation of the host rock foliation wrapped around the boudin blocks and marked with a dashed white line.*

Continued on the next page

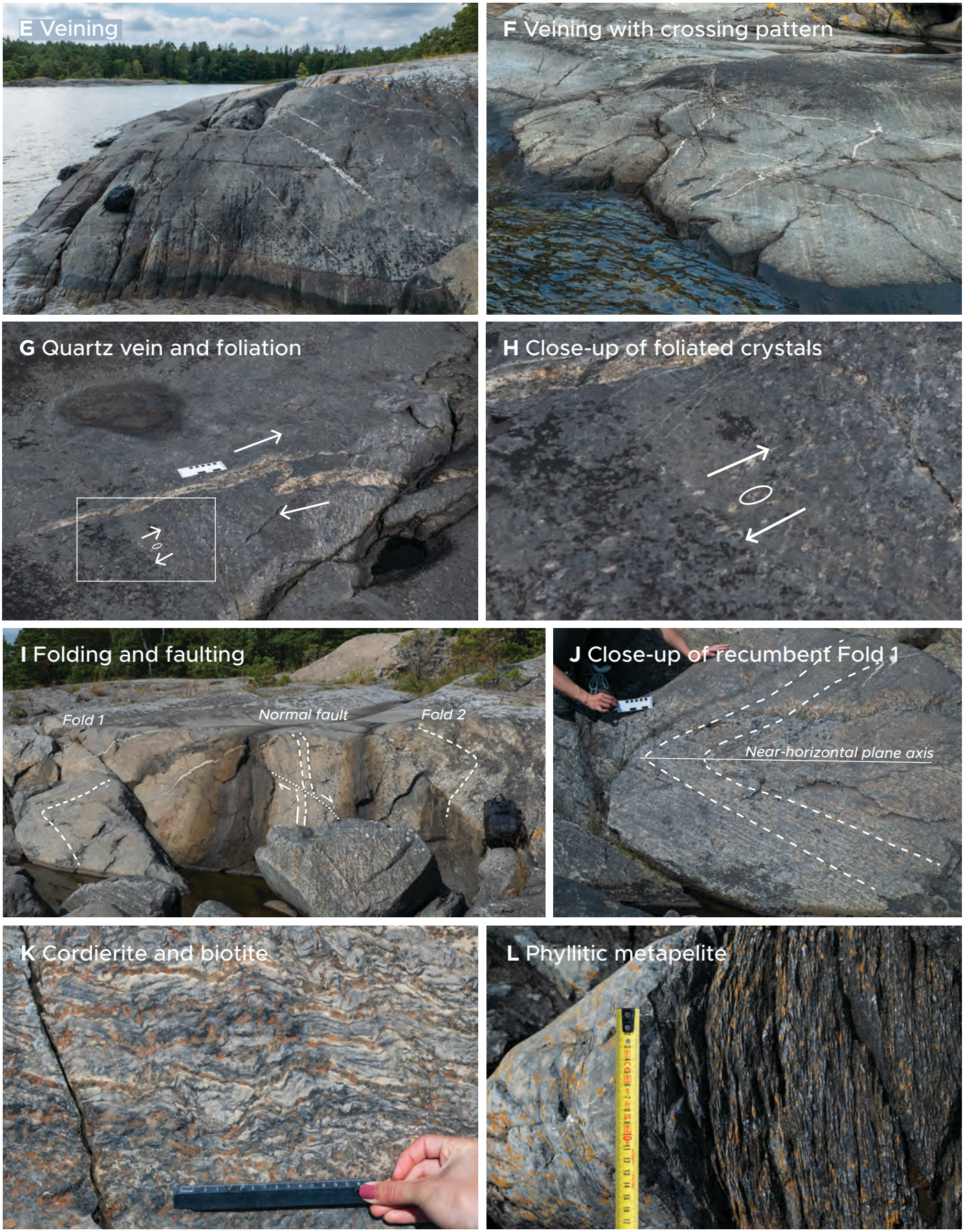

Figure 7 (continued): ***E*** *Multiple several meter long quartz veins.* ***F*** *Veining with cross-curring pattern.* ***G*** *Quartz vein and foliation of the host rock.* ***H*** *Close-up of the host rock foliation defined by flattened and elongated crystals.* ***I*** *Folding and faulting observed ca 15-20 m away from the logged outcrop. Two recumbent folds (Fold 1 and Fold 2) face each other and merge in the middle with vertical bedding. The displacement along the near-vertical bedding suggests that this deformation occurred after the bedding was reoriented.* ***J*** *Close-up of the recumbent Fold 1. The fold exhibits a near-horizontal axial plane characteristic of recumbent folds, which typically form under lateral compression.* ***K*** *Rusty cordierite crystals together with dark biotite-rich bands are indicative of medium-grade metamorphism.* ***L*** *Phyllitic foliation of metapelite suggests low to medium grade metamorphic conditions under directed stress.*

Continued on the next page

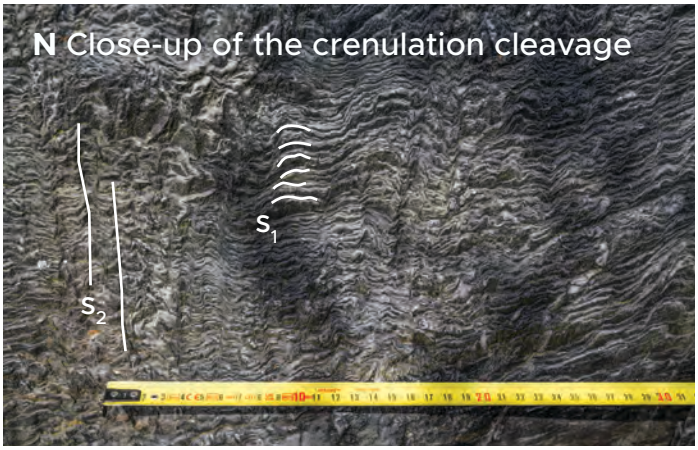

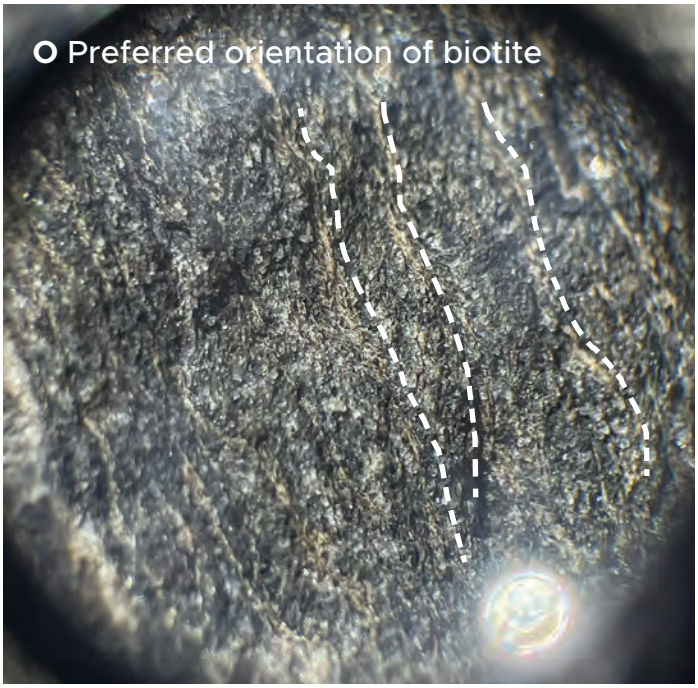

Figure 7 (continued) M *Crenulation cleavage showing microfolding over an existing foliation is indicative of multiple deformation events during metamorphic conditions.* ***N*** *Close-up of crenulation cleavage. S_1 represents the earliest foliation, now folded into smaller crenulations. S_2 represents later foliation.* ***O*** *Preferred orientation of dark biotite and light mica crystals (marked with white dashed lines) with translucent quartz crystals within the foliation. The orientation suggests alignment of minerals along a foliation plane. The image taken through a x10 hand lens at Section 3A of the logged outcrop.*

Interpretation

• Boudins provide evidence of extensional deformation and ductile conditions. A boudin, also called a pulled-apart block, is a feature that exhibits angular blocks with distinct necking. Necking occurs where strain was localized into the surrounding matrix that deforms more easily, causing the competent blocks to "pull apart". As a result the more competent material, such as quartz in this case, deforms into separate shapes due to extensional forces, while the surrounding rock deforms under shear conditions (Jerram and Caddick 2022). The foliation wrapping around the boudin blocks is a result of shear stress and indicate ductile deformation (Fig. 7 C-D). The sharp boundary between the competent material and the host rock in Fig 7B suggests minimal chemical alteration, while the partial quartz redistribution around the boudin in Fig.7 C-D suggests that the matrix acted as a pathway for fluid migration during deformation (Jerram and Caddick 2022).

• Joints are brittle deformation features that formed due to extensional and stress-release processes. Joints form when rocks that used to be buried deep within the Earth's crust rise closer to the surface. In the depth of the crust these rocks experience a lot of pressure, or overburden, and are significantly warmer. Over time, the overburden is gradually removed due to erosion by air, water, ice etc., and the rocks start to rise closer to the surface. This process is called exhumation. These changes in pressure and temperature alter the rock's shape: it stretches slightly vertically, shortens horizontally, and as it cools, it also contracts, leading to the formation of crack. Planar and long joints with regular spaces are called systematic joins. A group of such joints is called a joint set (Marshak 2001).

A set of fractures observed in the lower central part of the image 7A also indicates brittle deformation. These fractures are possibly related to localized stress or stress release form unloading and erosion, and developed through processes similar to joint formation. These features can be observed throughout the whole study area and are especially prominent in the same area as the veining, which possibly indicates episodic fluid infiltration along the fractures during or after their formation (Jerram and Caddick 2022).

• Quartz-filled veins are shown in Fig. 7E-F are deformation-related features observed. The cross-cutting quartz veins (Fig. 7F) formed in conjugate shear fractures that had formed earlier due to shear stress in the host rock. This pattern indicates multiple phases of deformation. Formation of quartz veins suggests fluid migration along these pre-existing fractures. The curved vein in Fig. 7G exhibits ductile deformation that aligns with the foliated crystals surrounding the vein seen in the close-up image in Fig. 7H. The vein deformation such as its irregular width and curvature suggest later progressive shearing that occurred after the vein had formed. The rusty coloration of some veins due to iron oxidation(Fig. 7G,) is likely indicative of fluid migration within the veins. Since there is no significant alteration in the host rock around the veins, this implies minimal metasomatic interaction (Jerram and Caddick 2022).

• The recumbent folds with their axes oriented towards the center, where the bedding becomes vertical, suggest ductile deformation associated with plastic flow at shallow crustal depths. Recumbent folds can form in sediments due to gravitational instabilities or overpressure in buried porous materials, where ductile behavior occurs due to high fluid pressures in pores (Fossen 2016). The displacement along the near-vertical bedding that previously used to be horizontal, suggests that this deformation occurred after the bedding had been reoriented. Folding and later faulting implies multiple deformation events.

• Cordierite, observed across the whole study area, is a cyclosilicate mineral with the formula $Al_3(Mg,Fe)_2[Si_5AlO_{18}]$ that typically forms in aluminous rocks that underwent high temperature and low to medium pressure during thermal or regional metamorphism (Fig. 6K). It is commonly forms alongside such minerals as andalusite, quartz, biotite and spinel within hornfels, schists and gneisses (Allaby 2020). Cordierite is a diagnostic mineral for metamorphic grade or compositional variations. Its formation is influenced by fluid-driven processes and chemical interactions with surrounding rocks (Jerram & Caddick 2022).

• Preferred orientation of biotite foliation is also an indicator of a metamorphic overprint. Biotite reorients under directed pressure to form foliated texture evidenced by the preferred alignment of biotite grains in Figure 7O (Jerram & Caddick 2022). The lighter quartz crystals within the foliation exhibit signs of recrystallization such as parallel alignment to the foliation and size variability. Additionally, the lighter platy minerals likely represent muscovite, also aligned parallel to the foliation under regional metamorphic conditions (Jerram & Caddick 2022).

A phyllitic metapelite outcrop with distinct phyllitic texture is located within approximately 5 m of the logged section. The protolith of this metapelite is mudstone, which has undergone low to medium grade metamorphism. Regional stress causes parallel orientation of phyllosilicate minerals, which leads to development of foliation that often has a slight sheen (Allaby 2020). Foliation develops when a rock undergoes both deformation and metamorphosis at the same time (Marshak 2001).

• Crenulation cleavage is another feature that is an evidence of deformation and metamorphism. It develops by microfolding pre-existing foliations and indicates multiple deformation and metamorphic events (Allaby 2020). Crenulation cleavage typically results from pressure solution, ductile shearing and faulting at a range of scales from microscopic to several decimeters (Rajlich 1991). This feature forms across a range of metamorphic conditions from low to medium grade, with microfolding and solution transfer processes at lower grades transitioning to grain recrystallization at higher temperatures (Gray 1987).

Field observations of metamorphism and deformation at Södra Sandvik provide evidence of multiple metamorphic and deformation events. Ductile deformation is indicated by features such as boudins, crenulation cleavage and deformed quartz veins. Brittle deformation is supported by jointing, fractures and faulting. Folding with two recumbent folds ca 15 m to the west from the logged area suggests compressional stress followed by faulting of the reoriented vertical bedding. The presence of cordierite, biotite and phyllitic texture also indicates low to medium grade metamorphism under regional metamorphic conditions. Petrographic analysis of the samples collected at the study site will provide further insights into metamorphic and deformation processes in the next part of this section.

Petrographic Evidence of Metamorphism and Deformation

The samples collected in Section 1 showcase porphyroblastic texture characterized by yellow cordierite porphyroblasts, while samples collected from the end of the log display fine-grained and finely laminated texture with no visible porphyroblasts. Textural differences in samples collected at the start and just past the end the logged are presented in Appendix D. Evidence of metamorphism and deformation observed in thin sections is presented below.

• A part of a cordierite porphyroblast is visible together with quartz and biotite crystals in Fig. 8 A and B. Cordierite can be difficult to identify due to its low birefringence, low relief and first order grey to white interference colors. However, cordierite is pleochroic. Its yellow pleochroism, seen in Fig. 8 A and serves as a distinguishing characteristic. Zircon or monazite inclusions within the cordierite can cause burn marks visible in plane-polarized light (PPL), appearing as darker yellow to orange-brown pleochroic halos surrounding the grains, and can be also considered a diagnostic property (Nesse 2000). The pleochroic halos can be seen in Fig. 8B and are marked with white dashed circles. Cordierite is absent in the samples collected just past the end of the logged area.

• The following characteristics of quartz crystals formed due to dynamic recrystallization and metamorphic deformation were observed: Grain Boundary Area Reduction (GBAR), undulose extinction, Grain Boundary Migration (GBM) and bulging in quartz grains.
- GBAR is indicated by the development of polygonal quartz grains with the characteristic 120° triple junctions shown in Fig. 8 C and D.
- Bulging recrystallization of quartz also shown in Fig. 8D and marked with white dashed circles.
- Undulose extinction can be best observed under crossed polars in the right top corner just above the larger quartz crystals in Fig. 8E.
- The irregular grain boundaries of the central quartz crystal in Fig. 8E suggest grain boundary migration (GBM) recrystallization.

• A cordierite crystal surrounded by a sericite reaction rim can be observed in Fig. 8H.

• Quartz-filled veins cutting through the matrix in Fig. 8E-G can be also observed in thin sections. Fig. 8F showcases several notable features: two quartz filled veins cutting across the matrix and a quartz band. The smaller vein on the right side of the image is surrounded by a matrix with different colors. A horizontal grey quartz band in the lower part of the image marked with two dashed lines contains larger quartz grains with potential preferred orientation.

• A fractured feldsar crystal with a yellow vein or staining passing through both parts of the crystal can be seen in PPL and XPL views in Fig. 8I. The crystal fragments are marked with a solid white line and the space between the fractured parts of the crystal is marked with a dashed line. Both the vein and the fractured crystal indicate brittle deformation. Additionally, almost parallel unfilled microfractures are visible in a sericitized cordierite visible in PPL and XPL views in Fig. 8J.

• Alignment of platy minerals muscovite and biotite can be observed in Fig. 8E and 8K-L respectively.

• Features that have a "stair-step" offset pattern are called C'-type shear bands and can be seen in Fig. 8M.

• Sagenitic texture can be observed in biotite crystals in the samples collected in Section 1 of the logged section. This texture features needle-like rutile forming asterisk-like clusters with rutile needles intersecting at approximately 60° and equilateral triangle shaped titanite inclusions and resembles "Widmanstätten-type" exsolution texture (Barker 2014).

• Rutile, titanite and ilmenite are common Ti-bearing minerals in metamorphic rocks, and were identified in all samples collected both at the beginning and the end of the log (Fig. 8O-R). Opaque grains shown in Fig.

8Q were identified as ilmenite based on the presence of Ti content discovered during the SEM-EDS analysis (Section 3.4).

• Sericite is a variety of white muscovite or paragonite that usually forms due to alteration of feldspar by hydrothermal alteration or later stage weathering and can be observed in Fig. 8R (Allaby 2020). It is a very finely crystalline alteration product (Barker 2014). Sericitization can be also observed within some cordierite porphyroblasts (Fig. 8J) as well as sericite rims (Fig. 8H). Sericite was not observed in the samples taken at the end of the logged area.

Interpretation

The following section correlates these features with literature in order to interpret their metamorphic and deformational context.

• Metamorphic grade for pelitic and semi-pelitic rocks can be deducted based on the presence of diagnostic minerals in the Barrowian sequence, the coexistence of specific minerals or the absence of certain mineral or mineral combinations (Jerram & Caddick 2022). Cordierite is a diagnostic mineral for determining

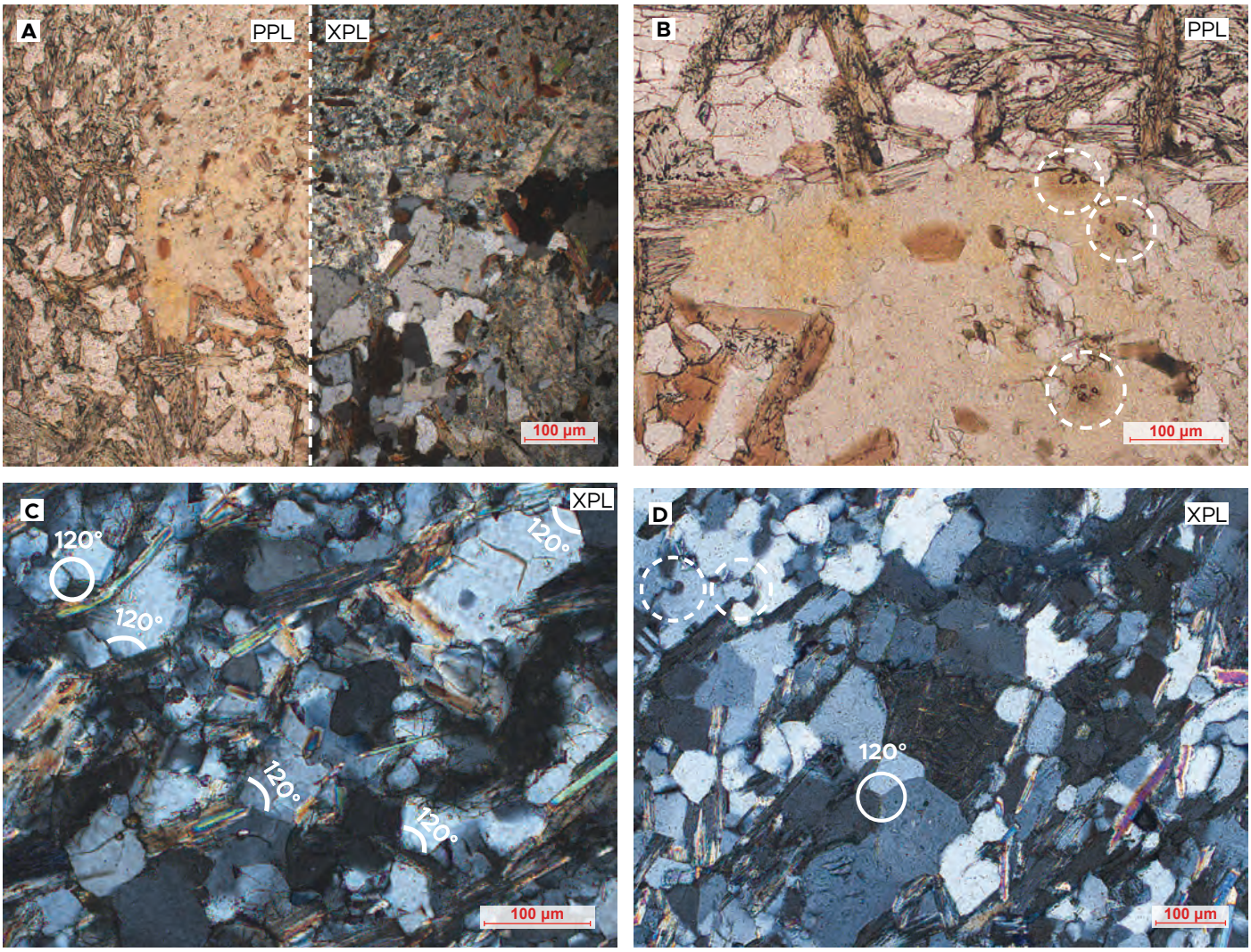

Figure 8 *Petrographic evidence of metamorphism and deformation in thin sections:* ***A*** *Photomicrograph of a part of a cordierite porphyroblast under PPL and XPL respectively (Sample 1a).* ***B*** *A close up of yellow pleochroic areas within a cordierite porphyroblast and grains of possibly zircon or monazite surrounded by pleochroic halos marked with white dashed circles (Sample 1).* ***C*** *This photomicrograph showcases Grain Boundary Area Reduction (GBAR) in quartz grains, which form triple junctions at approximately 120° through recrystallization, indicative of ductile deformation at high temperatures (Sample 1a).* **D** *Buldging marked with white dashed line and GBAR marked with a solid line (Sample 1a).*

Continued on the next page

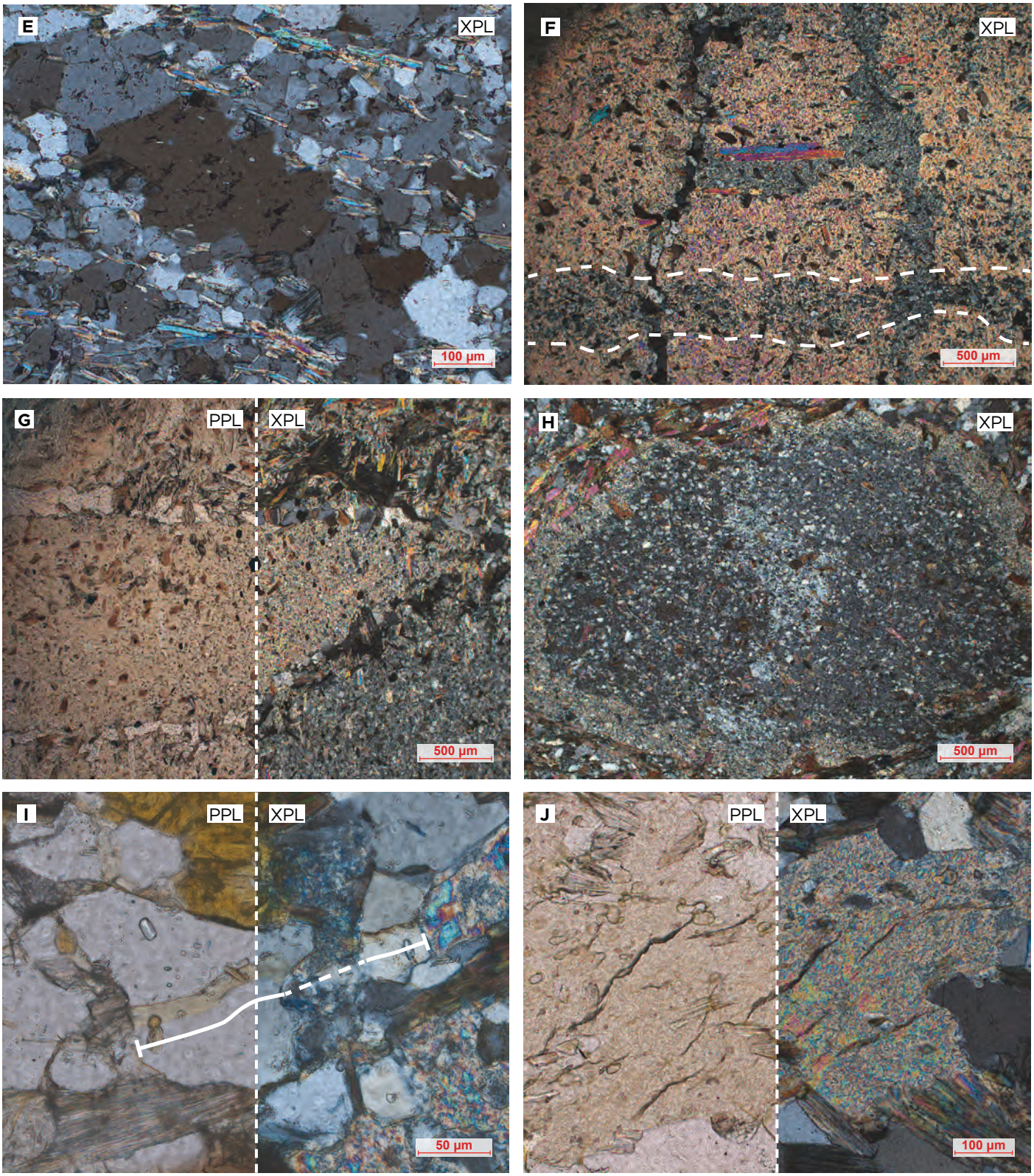

Figure 8 (continued): **E** *Undulose extinction best visible in the right upper corner above the larger central quartz crystal with irregular grain boundary is indicative of ductile deformation. The alignment of platy mica crystals reflects foliation formed under stress (Sample 1a).* **F** *A horizontal grey band marked with two white dashed lines in the lower portion of the image displays larger quartz grains with possible preferred orientation, suggesting deformation and recrystallization processes. One of the quartz veins, cutting across the sample on the right side, shows color changes in the surrounding matrix, indicative of potential fluid migration. A large muscovite porphyroblast perpendicular to the veins can be observed in the center of the image (Sample 1).* **G** *Veins filled with quartz crystals indicate fracturing and fluid activity (Sample 1a).* ***H*** *Cordierite grain surrounded by a fine-grained sericite reaction rim visible in cross-polarized light. The rim is evidence of retrograde reaction under lower metamorphic grade conditions, which involved hydration (Sample 9).* **I** *A fractured feldspar grain visible in PPL and CPL views, marked with a solid white line. The dashed line marks the space between the fractured parts of the crystal. The fractured crystal indicates brittle deformation (Sample 1).* **J** *Almost parallel unfilled microfractures in a sericitized cordierite in PPL and CPL are indicative of brittle deformation that possibly occurred during or after metamorphism (Sample 1).*

Continued on the next page

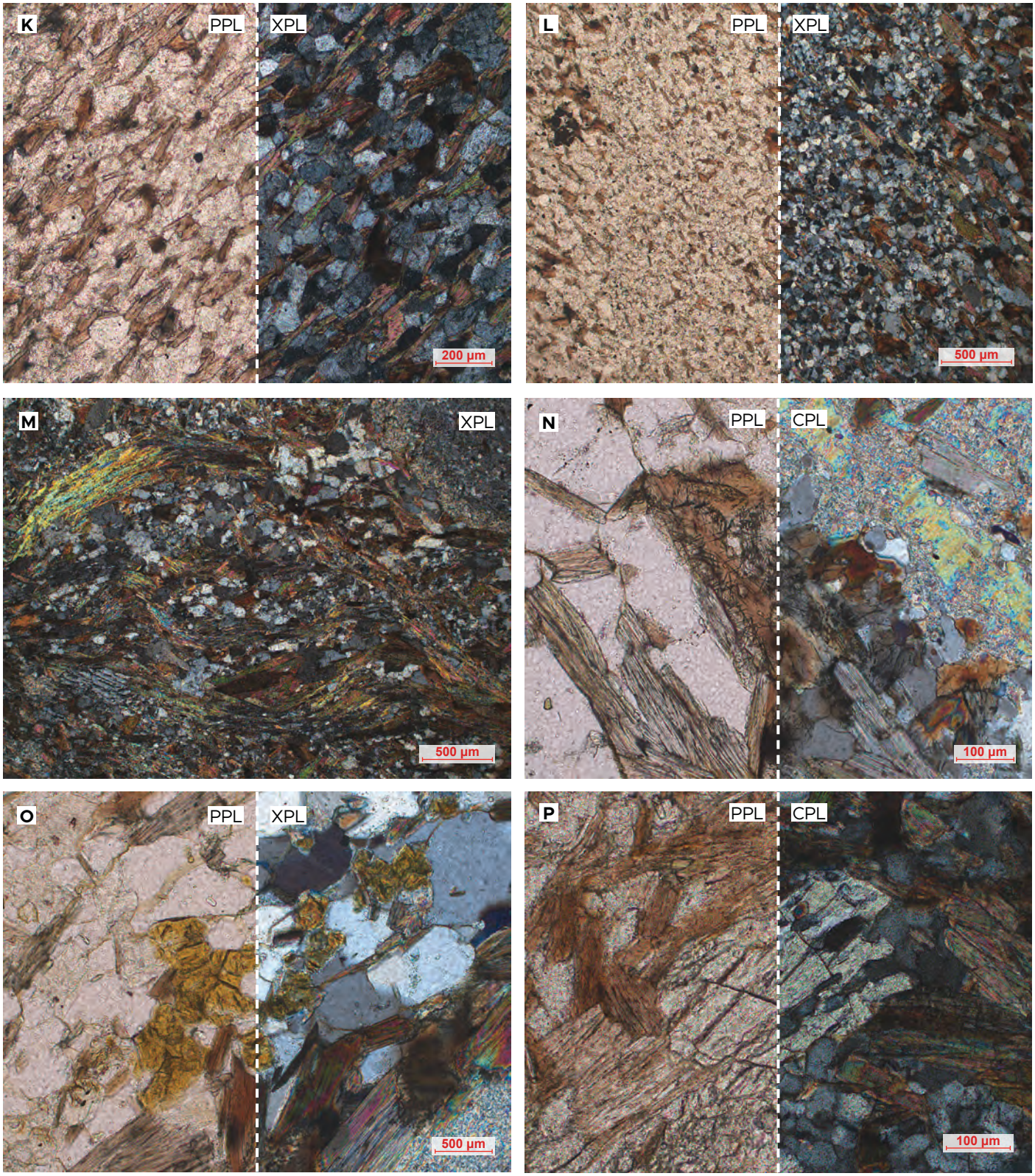

Figure 8 (continued): **K** *Alignment of biotite crystals in PPL and CPL reflects foliation developed during deformation (Sample 16).* **L** *Large biotite crystals within laminations and smaller biotite crystals between the laminations exhibit preferred orientation indicative of deformation processes (Sample 8).* ***M*** *"Stair-step" C'-type shear bands are indicative of simple shear deformation (Sample 9).* ***N*** *Sagenitic texture in a biotite crystal, characterized by needle-like inclusions of rutile and possibly titanite. This texture is indicative of retrograde metamorphism (Sample 1).* ***O*** *Rutile crystals are often stable in high-pressure metamorphic conditions but can be influenced by local Ti/Ca gradients (Sample 1a).* ***P*** *Titanite reflects low-grade metamorphic conditions influenced by Ca activity and fluid composition (Sample 9).*

Continued on the next page

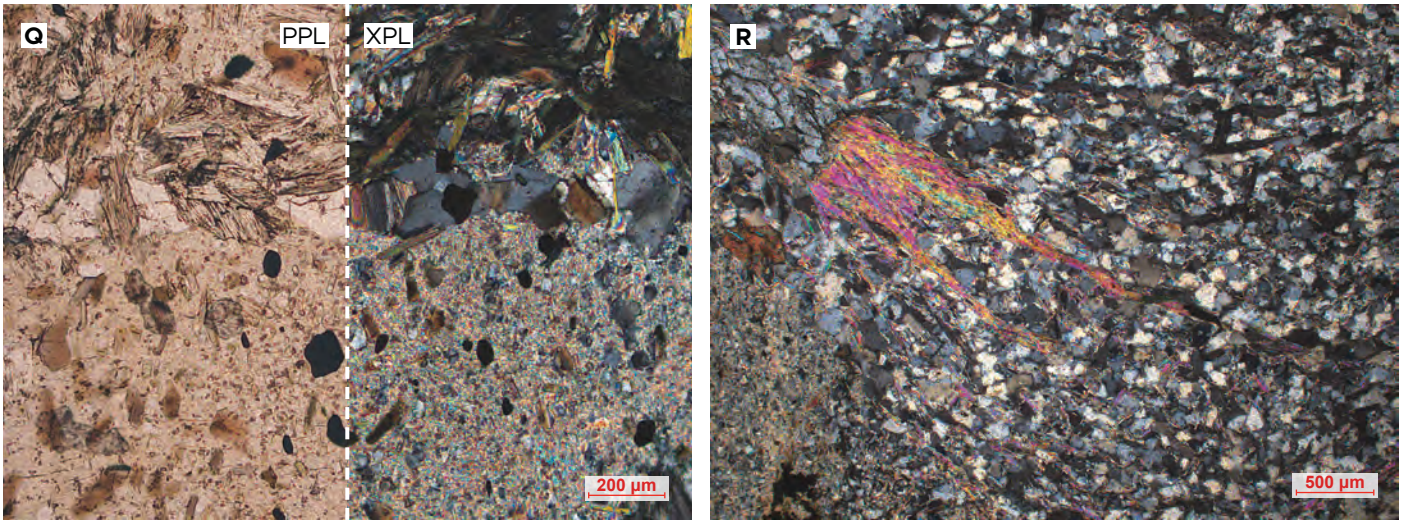

Figure 8 (continued): Q *Opaque grains interpreted as ilmenite, based on the presence of Ti in the outcrop. This mineral is present in all samples (Sample 1a)* ***R*** *Sericite forms as fine-grained white mica or paragonte usually by altering feldspars during hydrothermal alteration or later stage weathering. Present in the samples collected at the start of the logged sequence (Sample 1).*

metamorphic grade. It forms at high temperatures and intermediate to low pressure conditions (Klein and Philpotts 2016; Jerram & Caddick 2022). The combination of white mica, biotite, quartz and aluminium-rich mineral like cordierite is usually associated with medium-grade metamorphism in pelitic and semi-pelitic rocks. Jerram and Caddick (2022) broadly categorize greywackes as semi-pelitic rocks due to their high proportion of fine-grained material. All of the mentioned above minerals have been identified in the thin sections collected from Section 1 of the logged sequence. These conditions can be observed in low pressure regional metamorphic settings and sometimes in contact metamorphism. Cordierite is stable in amphibolite facies and often forms in response to large magma intrusions at shallow depths (Klein and Philpotts 2016).

• Several characteristics of quartz crystals mentioned above are indicative of dynamic recrystallization and metamorphic deformation:
- GBAR is indicative of grain growth during deformation with high temperature recovery (Fig. 8C and D).
- Bulging recrystallization of quartz is indicative of localized grain boundary migration under moderate to low differential stress (Fig. 8D).
- Undulose extinction is indicative of ductile deformation (Fig. 8E.) It is occurs when a crystal lattice is slightly bent due to the accumulation of dislocations, which causes uneven extinction and appears as "sweeping" or irregular patchy zones associated with these dislocation or small fractures.
- Grain boundary migration (GBM) recrystallization indicated by the irregular grain boundaries of the central quartz crystal in Fig. 8E suggest recrystallization that occurred at high-temperatures. This is a process where due to higher temperatures grain boundaries sweep through crystals to remove dislocations and sub-grain boundaries, leading to lobate boundaries and formation of new grains of variable sizes.

Together, these features are indicators of dynamic recrystallization and metamorphic processes within the outcrop that occurred in a range of temperatures and under directed stress. GBAR and GBM are indicative of recrystallization at higher metamorphic grades, and bulging and undulose extinction suggest localized deformation under moderate stress and lower temperature (Passchier & Trouw 2005).

• A sericite reaction rim around a cordierite crystal is the product of a reaction between the cordierite and the surrounding it matrix minerals during retrograde metamorphism. Such reaction rims form when dis-equilibrium conditions result in the growth of new minerals through hydration or carbonation reactions under lower-grade metamorphic conditions (MacKenzie *et al.* 2017). These reaction rims can be mono- or polymineralic zones and usually involve hydrous phases (Barker 2014). The presence of this rim indicates a shift to cooler and more hydrous conditions and serves as evidence of retrograde metamorphism.

• Two quartz filled veins cutting across the matrix and a quartz band also suggest deformation and fluid-related processes, specifically the matrix exhibiting different colors around the smaller vein in Fig. 8F compared to the rest of the thin sections. Which is possibly indicative of fluid migration during or after fracturing that potentially affected the composition of the matrix (Jerram & Caddick 2022). Preferred orientation of quartz within the band marked with a white dashed line in the lower part of the image suggests deformation and recrystallization under directed stress.

• The fractured crystal and the vein in Fig. 8I suggests brittle deformation. Microfractures in a sericitized cordierite visible in Fig. 8J may have formed after metamorphic event. The absence of fluid infill suggests limited or no fluid activity during or directly after fracturing (Jerram & Caddick 2022).

.• The alignment of platy minerals such as muscovite in Fig. 8E and biotite in Fig. 8K-L indicates preferred orientation of the minerals and suggests deformation and recrystallization associated with metamorphic conditions. Foliation forms due to parallel or subparallel arrangement of elongate minerals under directed stress during regional metamorphism. It is influenced by the growth rates of platy minerals, which grow faster perpendicular to the maximum principal compressive stress. Additionally, reorientation and flattening of minerals within the foliation plane is also influenced by such processes as shear and dissolution-precipitation reactions (Philpotts & Ague 2009).

• C'-type shear bands are indicative of deformation in shear zones. These features have a "stair-step" offset pattern with small parallel zones of localized shear cutting through the main foliation at an oblique 15–35° angle. These bands can indicate the direction of movement within the shear zone and serve as indicators of dynamic metamorphism (Philpotts & Ague 2009).

• Sagenitic texture is associated with retrograde metamorphism, when Ti- and Ca-rich biotite that formed at higher temperatures (e.g., amphibolite facies) becomes unstable at lower temperatures, leading to excess Ti and Ca precipitating as titanite and rutile (Shau *et al.* 1991).

• Rutile, titanite and ilmenite can be indicative of certain metamorphic conditions as it was showed in the experiments by Pereira *et al.* (2023). For example, titanite can remain stable at low-grade metamorphic conditions, rutile at high pressure and ilmenite at high temperature - low pressure conditions. However, both titanite and rutile can coexist, as seen in the samples collected at Södra Sandvik, and be stable at low or high pressure. The main controlling factors of their stability are Ti/Ca and Ca/Al ratios within the rock, which can shift locally during mineral replacement reactions. The presence of these minerals throughout the whole outcrop reflects fluid activity within the rock, which controls mineral stability across different pressures and temperatures (Pereira *et al.* 2023).

• Sericitization observed within some cordierite porphyroblasts (Fig. 8J) as well as the presence of sericite rims (Fig. 8H) points to localized hydrothermal reactions and fluid activity that altered properties of cordierites and other surrounding minerals, possibly feldspars. Sericite was not observed in the samples taken at the end of the logged area.

Petrographic findings are consistent with field observations and provide evidence of several metamorphic and deformation events. At least one prograde metamorphic event is evidenced by the presence of cordierites and other metamorphic minerals, while retrograde metamorphism is evidenced by the presence of sagenitic texture, a reaction rim and sericitization, features indicative of cooling and fluid-driven reactions. Dynamic recrystallization of quartz and the presence of C'-type shear bands suggests ductile deformation, also observed in the field in such macro-structures as, for example, boudins and crenulation cleavage. Microfractures, veining and fragmented quartz crystals that can be observed in thin sections suggest brittle deformation, which was also observed in the field (jointing, fractures, faulting). Interestingly, metamorphic "gradient" is not evenly distributed throughout the site. This is evidenced by the difference in metamorphic textures between the samples collected at the beginning of the log that contain cordierite porphyroblasts and sagenitic texture and the fine-grained laminated samples collected at the end of the log. Cordierites indicate

higher temperatures, while the fine-grained laminated texture observed at the end of the log suggests lower metamorphic grade or possibly a variation in protolith composition across the study area. Additionally, sericitization, quartz-filled veins and the presence of rutile and titanite in the same samples suggest dynamic fluid activity. The presence of muscovite, biotite, quartz and aluminium-rich mineral like cordierite point to medium-grade metamorphism, according to Jerram and Caddick (2022), while textures like foliation, C'-type shear bands and dynamic recrystallization suggest regional metamorphism (Philpotts & Ague 2009).

In general, both field and petrographic observations align with two phases of metamorphism reported by Talbot (2008) and Skelton *et al.* (2018). Talbot (2008) identified two phases of deformation that occurred at the same time and even outlasted both metamorphic events, associated with the Svecokarelian orogeny. Skelton *et al.* (2018) state that both phases occurred between 1.96 and 1.80 Ga. Samples used for P–T estimates for Utö by Skelton *et al.* (2018) record pressures of 0.28–0.45 GPa and temperatures of 518–550°C, consistent with low to low-medium metamorphic grades within the amphibolite facies.

3.4 SEM-EDS Analysis

SEM-EDS analysis was performed in order to analyze suspected biotic features, morphologies and chemical composition of the samples. However, no clear biotic features indicative of life except for the wrinkled discontinuous laminations (described in the sedimentological log in Section 3.1) were identified neither in the samples collected from the beginning of the logged area nor in the sample from the end. Thus, this section presents SEM images of the laminations, the chemical composition of the samples and chemical maps of the laminations in order to analyze their chemical composition and potential biotic origin.

• SEM images of three different samples presented in the images below in Fig. 11 show distinct laminations. Image A is an overview of a wider area that includes a lamination rich in biotite on the left side of the image and a part of a cordierite porphyroblast on the right. Image B Is a composite overview of several laminations, also consiting of biotite. Image C showcases a close up of the laminations, surrounded by grey and dark grey quartz and feldspar as well as smaller white monazite crystals. The light grey-colored crystals are biotites. The laminations do not exhibit any morphologies indicative of biotic origin such as fossilized filamentous networks, irregular and diffuse boundaries, microspheroids or trapped and bound grains. The borders of the laminations in all samples are distinct. Additionally, in the SEM images of the laminations appear to consist of mainly biotite, but their chemical composition will be discussed further in this section.

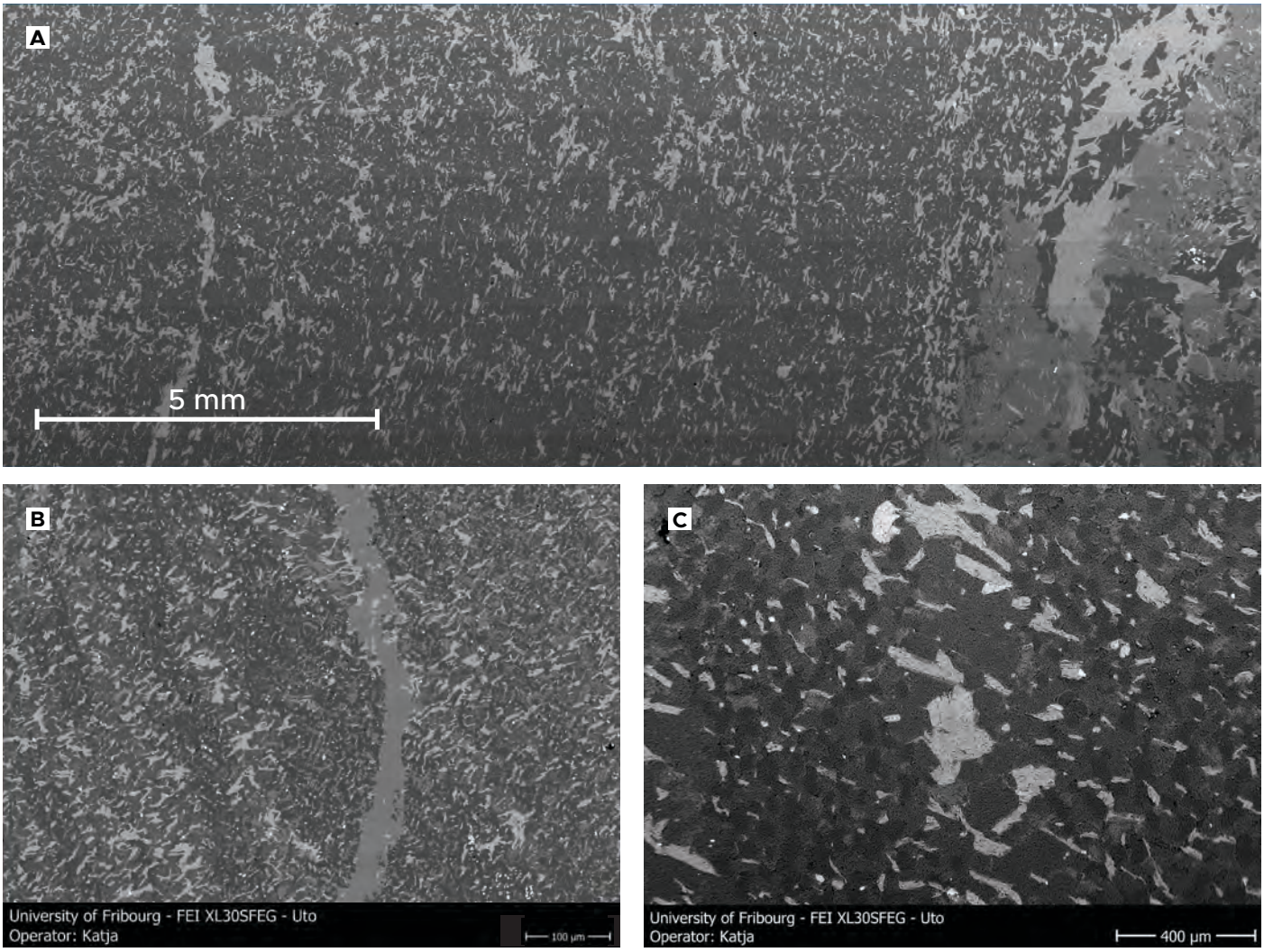

Figure 11 *SEM images of the samples:* ***A*** *A composite overview of Sample 1with a distinct vein on the left side and a part of a cordierite porphyroblast on the right.* ***B*** *A composite image of several laminations showing distinct boundaries between minerals (Sample 15).* ***C*** *A close-up of a laminations positioned at the center of the image surrounded by grey and dark grey quartz and feldspar and white monazite crystals.*

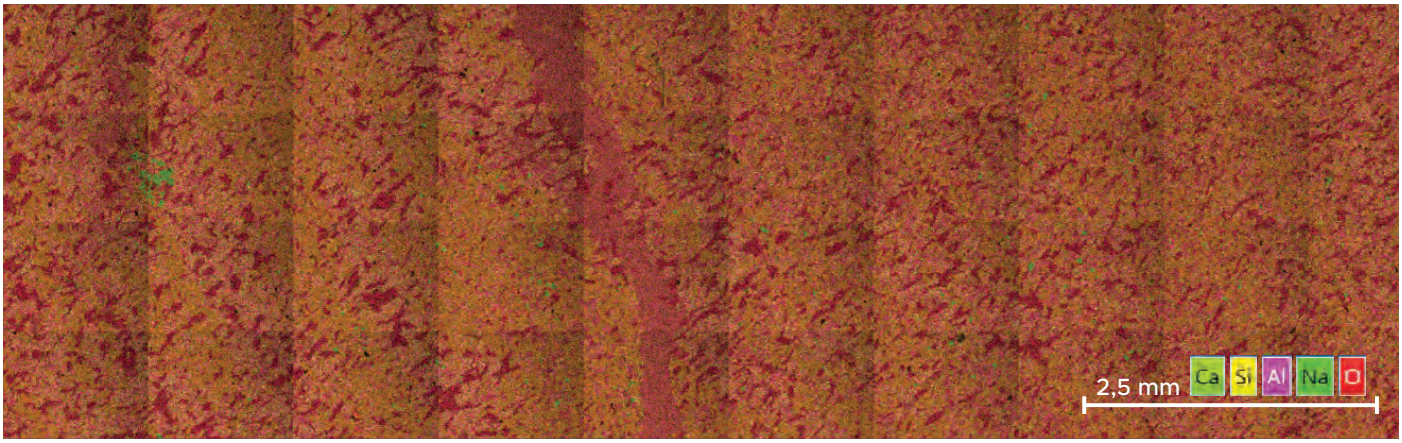

Figure 12 *Composite elemental map showing the distribution of elements Ca, Si, Al, Na and O across the laminations in Sample 8. Separate maps for each element are available in the Appendix F5.*

• The composite map in Fig. 12 shows rather even distribution of the elements as well as the standalone maps for all elements that can be found in Appendix F4:

Si: Map nr.2 for silicon shows more clear difference between the laminations with lighter parts representing quartz-rich zones and darker parts representing biotite and feldspar zones, since feldspar contains less silicon than quartz.

Na: The brighter concentration in the sodium map, nr. 3, shows feldspar rich zones.

Al: Laminations with brighter signals in the aluminum map nr.4 indicate feldspar or biotite. Since quartz lacks aluminum, darker zones are likely to be quartz-rich.

Ca: Calcium appears as a faint dark hue across the whole map that corresponds with aluminum signal as well as more concentrated scattered spots. The faint hue signal that aligns with aluminum concentrations suggests the presence of plagioclase feldspar, while concentrated spots suggest a calcium bearing mineral such as apatite. Both minerals were identified in a more detailed analysis of the sample presented in the next part of this section.

Ce and Nd: The maps for both elements show weak and diffuse hue with no distinct concentrations. Both elements are rare earth elements (REE) and are diffusely distributed throughout the sample. Both cerium and neodymium maybe present in trace amounts and may also be associated with monazite, which was also identified in the chemical analysis of the samples.

The map sum spectrum in Fig. 13 shows ca 30% of silicon, consistent with the abundance of quartz and feldspar. Approximately 8.7% of aluminum supports the presence of feldspar. The presence of potassium and iron in the sum spectrum aligns with the occurrence of biotie. Trace elements such as REEs likely reflect the presence of accessory minerals.

• Detailed spectra for two samples from the beginning and end of the log will be presented next, Sample 1 and Sample 8 respectively. The sites for analysis were chosen based on the lowest sigma weight % to ensure minimal error margin for oxide and formula calculations. A table with SEM-EDS error margins for spectra with sigma weight % values over 0.3% is provided in Appendix F3. The value of 0.3% was chosen as a threshold to be fully transparent about potentially unreliable measurements in the data.

Element	Weight %	σ
O	46,00	0,04
Si	29,70	0,03
Al	8,67	0,01
Rb	3,58	0,05
Na	3,58	0,01
Fe	3,40	0,01
K	2,77	0,01
Ca	1,25	0,01
Ti	0,31	0,01
In	0,27	0,03
Sb	0,17	0,02
Tb	0,12	0,02
Cd	0,08	0,02
Ba	0,07	0,01
Mn	0,04	0,01

Figure 13 *Map sum spectrum for the composite elemental map.*

Sample 1

The SEM-EDS analysis of Sample 1 (Fig. 14) confirms the presence of quartz, biotite and plagioclase feldspar, which were suggested from the sum spectra and the composite chemical maps in Fig. 12 and 13. Plagioclase feldspar zones can be seen in the sodium map, while biotite shows higher iron and potassium signals. Potassium signals can also be associated with k-feldspars. Quartz crystal is almost completely composed of SiO_2 (Spectrum 26). Calcium in this sample is also concentrated in small localized spots. Such spot with a strong Ca signal was identified as apatite (Spectrum 29). The stoichiometry calculations used for mineral identification can be found in Appendix F2. Bromine was detected as a diffuse hue across the sample, although it is absent from the spectra measurements, suggesting that it is only present in trace amounts. Additionally, high concentration of ZrO_2 suggests the presence of zircon (Spectrum 23), which can be either a detrital grain from the original sediment or a crystal that formed during metamorphism.

Sample 8

The SEM-EDS analysis of sample 8 showed a mineralogical composition dominated by feldspars (K-feldspar and plagioclase), biotite and monazite (Fig.15). Several monazite grains (white speckles in the electron image in Fig.14) were identified (Spectra 14, 17, 20, 21). This minerals contains significant amounts of Ce_2O_3, La_2O_3, Nd_2O and other REE. Several attempts to create elemental maps for this sample exhibited strong noise, possibly due to interference from REEs which may have affected data acquisition. These maps were not included in the paper, but the patterns for REE showed their enrichment in the monazite grains along with calcium and phosphorus, as can be seen in the chemistry table of Sample 8 in Fig. 15.

Spectra from sample 8 contains more REEs compared to the specific site mentioned from Sample 1. However, comparison of other sites in Sample 1 showed similar levels of REEs across the logged area (Appendix F1, Sample 1 Site 4), suggesting similar REE distributions across the whole outcrop.

Intrepretation

According to Noffke *et. al* (2013), microscopic laminae in ancient fossilized microbial mats fabrics from younger Archean, Proterozoic and Phanerozoic time periods remnants can be composed of some original carbon, although they are usually mineralized forming pyrite, hematite and goethite and trapped-and-bound grains. In thin sections, cut perpendicular to mat layers, fossilized microbes often resemble networks of intertwined and curved laminae, which incorporate fossilized EPS, trichomes, filaments and allochthonous sedimentary grains. In comparison to organic microfossils or organic biofilms, microbial mats are preserved through mineral replacement rather than impregnation. Laminae in mats have less clear and rather diffuse borders due the release of chemical compounds and organic matter through microbial decomposition during diagenesis of the mat (Noffke *et al.* 2013).

The mineralogy of the samples collected at the study site confirms meta-greywacke with most common minerals being quartz, plagioclase feldspar and biotite as well as some accessory minerals such as monazite, zircon and apatite. The origin of zircon and apatite is not clear and could be detrital or metamorphic. The light laminations are mostly composed of quartz, feldspar and possibly muscovite, while dark laminations follow the pattern of iron- and aluminum-bearing minerals such as biotite and sodium-bearing patterns suggest plagioclase feldspar. The clear patterns of the laminations with sharp borders seen in the composite maps of silicon, sodium and aluminum suggest that the laminations are mineralogically controlled. This is also supported by the SEM images, which reveal well-defined laminations without any biotic textures or filamentous structures. No carbon was observed in the laminations, excluding the possibility of detecting preserved organic material. The scattered distribution of calcium in both composite map and the close-up map from Sample 1 indicate that calcium is not a major component in the rock and it exists as inclusions or phases of such minerals as apatite, plagioclase and monazite. No minerals associated with biotic processes in similar settings such as hematite, pyrite (or other iron sulfides), goethite, chamosite, illite or calcite (Noffke, 2022), were identified in the analyzed samples. Significant amounts of Ce_2O_3, La_2O_3, Nd_2O and other REEs

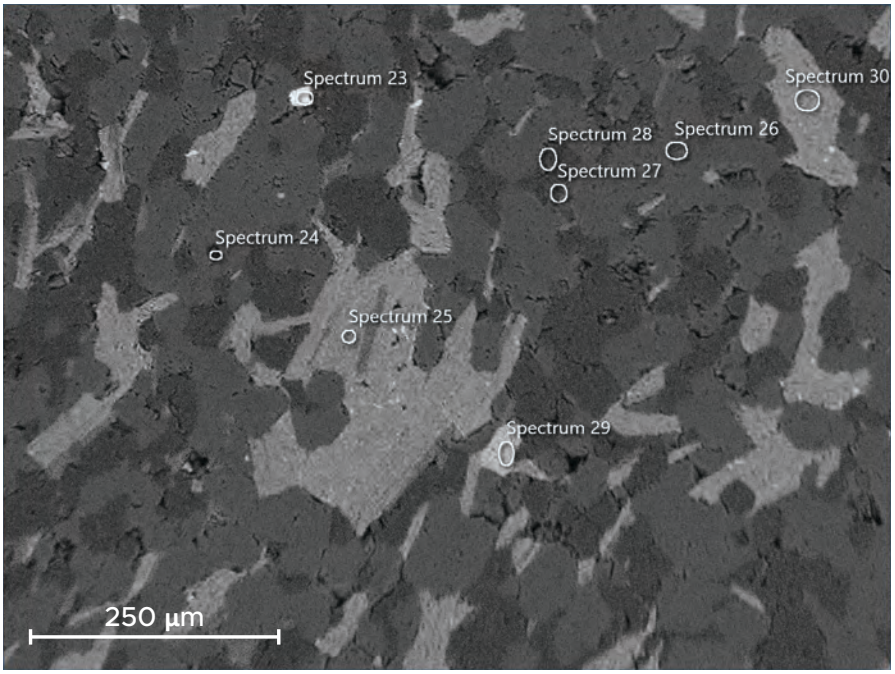

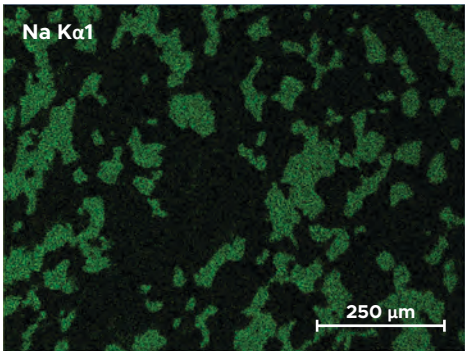

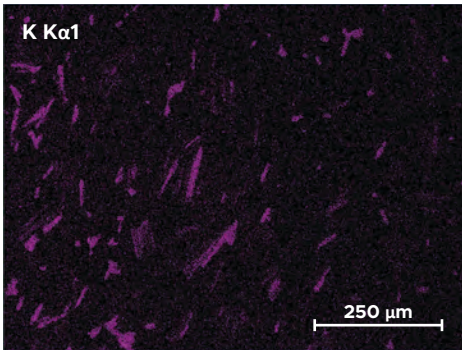

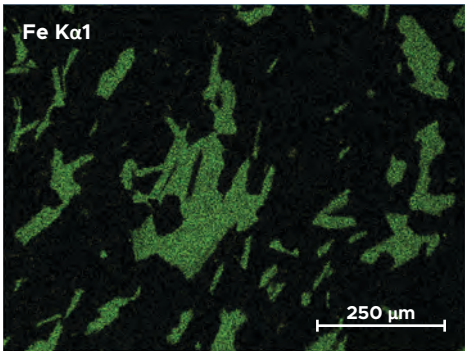

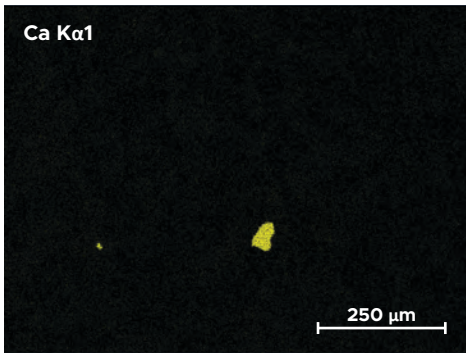

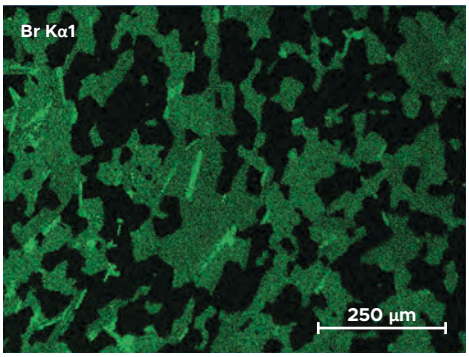

Sample 1	Spectrum 23	Spectrum 24	Spectrum 25	Spectrum 26	Spectrum 27	Spectrum 28	Spectrum 29	Spectrum 30
Oxide	Zircon	Plagioclase f-spar	Biotite	Quartz	Plagioclase f-spar	Plagioclase f-spar	Apatite	Biotite
	Oxide wt %							
SiO_2	35.98	85.51	31.93	99.97	73.28	67.29	1.82	30.67
Al_2O_3	4.63	—	24.39	—	16.91	20.18	—	22.90
Na_2O	2.22	2.40	—	—	8.80	11.74	—	—
CaO	1.01	2.59	—	—	0.38	0.77	54.78	—
FeO	2.15	—	24.11	—	—	—	0.49	24.89
K_2O	—	1.43	0.55	—	0.61	—	—	0.41
MgO	—	—	16.31	—	—	—	—	17.09
TiO_2	—	0.77	—	—	—	—	—	1.27
Cl_2O_7	—	8.38	—	—	—	—	—	—
ZnO	—	1.37	—	—	—	—	—	—
SO_3	—	1.92	—	—	—	—	—	—
Y_2O_3	7.12	—	—	—	—	—	—	—
ZrO_2	46.66	—	—	—	—	—	—	—
P_2O_5	—	—	—	—	—	—	42.88	—

Figure 14 *Chemistry of sample 1 (oxide weight %) derived from SEM-EDS spectra from Aztec software and chemical maps of the same site showing spatial distribution of the elements. The stoichiometry calculations used for mineral identification can be found in Appendix F2.*

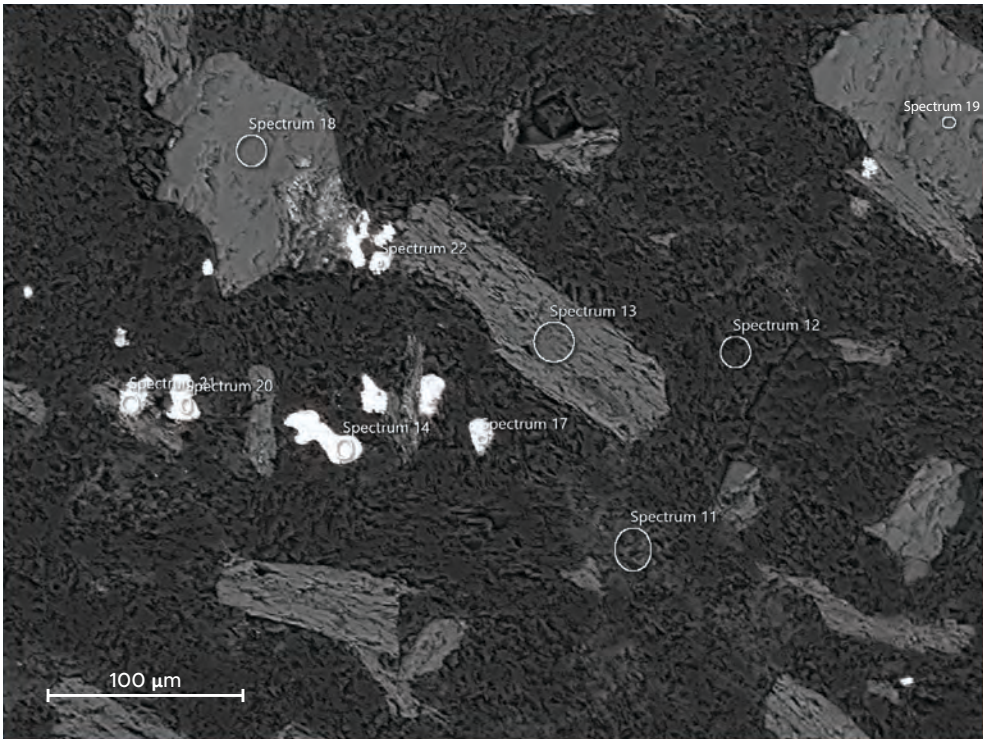

Sample 8	Spectrum 11	Spectrum 12	Spectrum 13	Spectrum 14	Spectrum 17	Spectrum 18	Spectrum 19	Spectrum 20	Spectrum 21	Spectrum 22
Oxide	K-feldspar	Plagioclase f-spar	Biotite	Monazite	Monazite	Biotite	Biotite	Monazite	Monazite	Biotite
	Oxide wt %									
SiO_2	62.98	62.40	32.32	—	13.11	35.85	34.86	—	3.21	3.14
Al_2O_3	21.41	23.90	22.22	—	5.97	21.24	21.33	—	1.83	1.78
Na_2O	1.60	9.21	—	—	2.71	—	—	—	—	—
CaO	0.53	4.49	0.34	0.85	5.19	—	—	1.06	5.74	0.95
FeO	—	—	26.77	—	—	20.83	22.73	—	0.62	—
K_2O	13.48	—	2.43	—	—	8.43	6.55	—	—	—
MgO	—	—	11.89	—	—	9.75	10.43	—	—	—
TiO_2	—	—	0.72	—	—	1.59	1.22	—	—	—
MnO	—	—	0.31	—	—	—	0.32	—	—	—
ZnO	—	—	—	—	—	—	—	—	—	—
Ce_2O_3	—	—	—	32.90	23.14	—	—	32.09	26.53	32.55
La_2O_3	—	—	—	17.36	12.78	—	—	18.01	14.20	17.24
P_2O_5	—	—	—	32.65	28.03	—	—	37.17	31.12	29.63
Nd_2O_3	—	—	—	11.92	9.06	—	—	11.66	9.80	12.19
Pr_2O_3	—	—	—	2.77	—	—	—	—	2.17	—
Sm_2O_3	—	—	—	1.55	—	—	—	—	1.32	—
Y_2O_3	—	—	—	—	—	—	—	—	3.39	2.51

Figure 15 *Chemistry of sample 8 (oxide weight %) derived from SEM-EDS spectra from Aztec software. The stoichiometry calculations used for identification of minerals can be found in Appendix F2.*

were found in monazites both in the beginning and the end of the log. Monazites and zircons were identified in all samples collected from the outcrop. The composite REE maps did not show any correspondence with the laminations and their diffuse distribution suggests that they occur as trace amounts across the samples or concentrated in monazite grains. Thus, no definitive evidence of biotic origin was found in the analyzed samples.

3.5 Analysis of Fluorescent Features in Thin Sections

All samples collected from the outcrop were scanned using fluorescent microscopy in order to detect and study the possible organic remains or diagnostic grain size variation. Green fluorescence (FITC) images were omitted due to the absence of a signal, since the samples were coated in resin. Brightfield and TexRed fluorescence images for all samples collected at Södra Sandvik locality are presented in Appendix D.

Grain size variation can be used to assess biotic influences in sedimentary rocks, however, original grain structures were destroyed by metamorphic overprint in this study, making such analysis not possible. Fluorescence imaging revealed that, interestingly, fluorescence is mainly found at the outer edges of cordierite porphyroblasts in all the samples collected in the beginning of the logged area, while the samples collected from the end of the logged area, where no cordierites are present, exhibit little to no fluorescence.

Fluorescent edges of cordierite porphyroblasts seen in the scans of the thin sections of Samples 1 and 1a are marked with a dashed white line (Fig. 16). The corresponding to the fluorescent zones photomicrographs are presented in the same figure. Additional scans of thin sections for Samples 9 and 11 as well as corresponding photomicrograps are included in Appendix E. The fluorescence is most intense at the outer borders of the porphyroblasts and decreases inward. It appears to be uniform and does not seem to be associated with any mineral inclusions within the edges of the cordierite porphyrobasts. However, not all edges of the porphyroblats are fluorescent and not all cordierite porphyroblasts show fluorescence. This is best seen in Appendix D, where fluorescence scans are paired with brightfield scans and all of the porphyroblasts are clearly visible.

Cordierite porphyroblasts exhibit partial replacement textures indicative of retrograde metamorphism, including sericitization and possible chloritization best seen in cross-polarized light in Fig. 16. The possible chloritization texture is best evident in Sample 1a (Fig. 15, Images N and O). While the darker alteration zones resemble chloritization, it could also be fine-grained pinite described by Nesse (2000). Fluorescent area 4 of Sample 1 in Fig.15 shows a fluorescent grain that exhibits similar texture seen in the porphyroblasts with alternating dark and light bands under cross-polarized light. This grain could possibly be a cordierite fragment that detached during metamorphism and deformation.

Interpretation

The fluorescence patterns observed in the thin sections are primarily concentrated along the outer edges of cordierite porphyroblasts and have no clear association with other minerals or textures. The textures observed in the cordierites suggest mineral alteration during retrograde metamorphism. Nesse (2000) describes cordierite as a mineral susceptible to fluid-mediated alteration. SEM-EDS analysis confirmed the presence of REEs both concentrated in monazite and zircon crystals as well as also diffusely spread across the samples as trace elements. The fluorescence observed at the edges could indicate that REEs were redistributed by metamorphic fluids during cooling, possibly linked to hydrolytic alteration processes that promote element mobility (Vernon and Clarke 2008). The authors write that a number of elements becomes mobile during low temperature hydrous alteration, especially light REEs. Since the fluorescene is mostly observed along the edges of the porphyroblasts, it could mean interaction between the REE-bearing fluids and the porphyroblasts. The REEs could have been acquired from the protolith or metasomatic fluids during retrograde metamorphism.

An additional chemical analysis comparing the fluorescent and non-fuorescent areas of cordierites is needed to confirm whether the fluorescence occurs due to REE enrichment or some other metamorphic alteration. Nevertheless, no other fluorescence signals and textures resembling degraded microbial mat fabrics were detected in any of the samples.

Sample 1

Fluorescent area 1:

Fluorescent area 2:

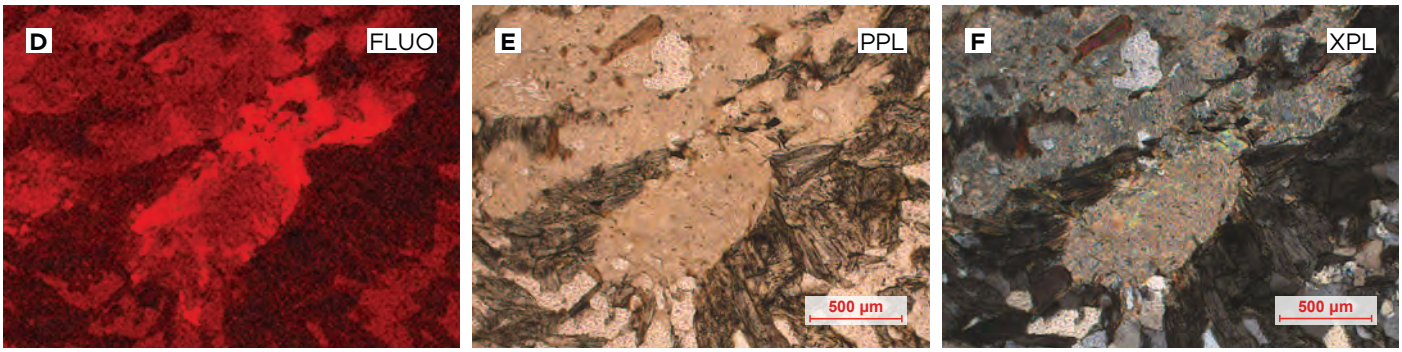

Fluorescent area 3:

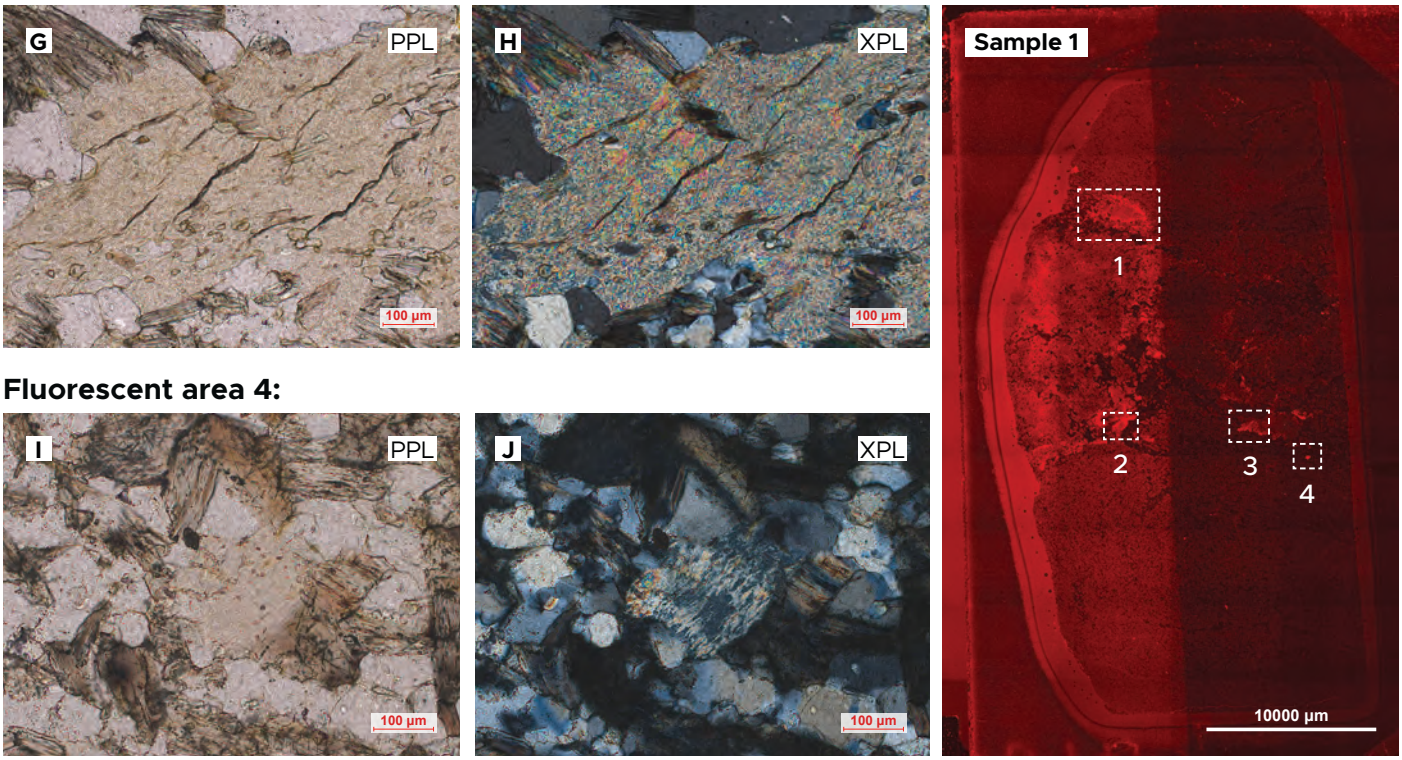

Fluorescent area 4:

Figure 16 *This part of the figure shows some of the fluorescent areas observed in Sample 1 and corresponding photomicrographs. Fluorescent areas are marked with a white dashed line in the thin section scan in the lower right corner. Images A-C correspond to Zone 1, D-F to Zone 2, G and H to Zone 3, I and J to Zone 4 of Sample 1.*

Continued on the next page

Sample 1a

Fluorescent area 1, a wider view and close-up photomicrographs:

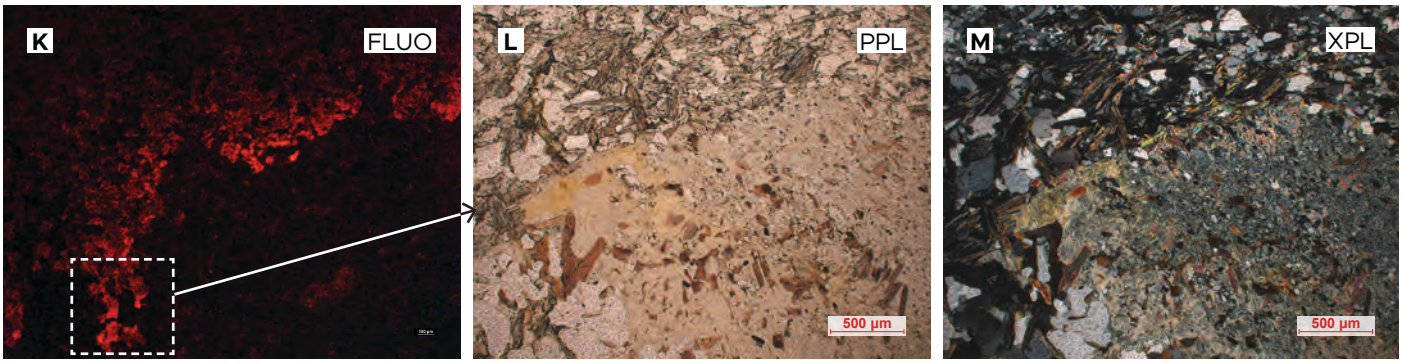

Fluorescent area 2:

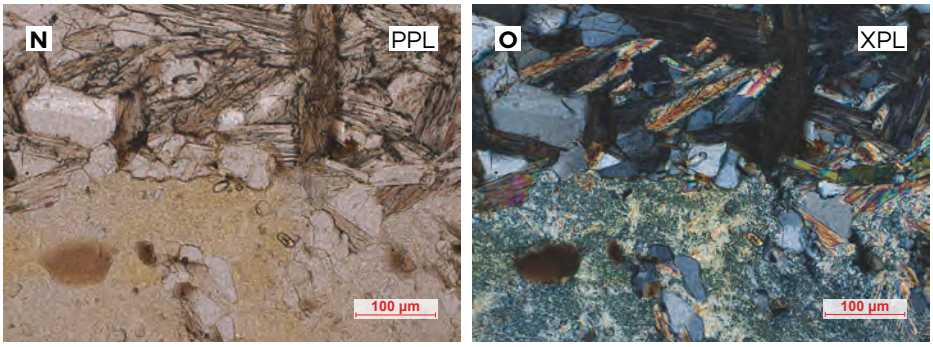

Fluorescent area 2 (another part of the same zone):

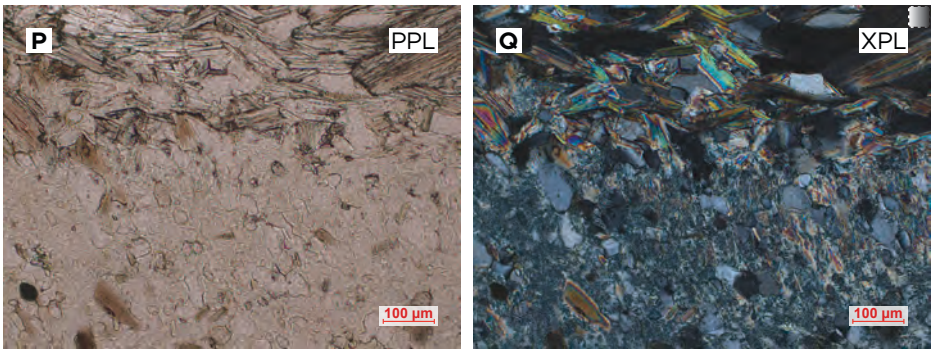

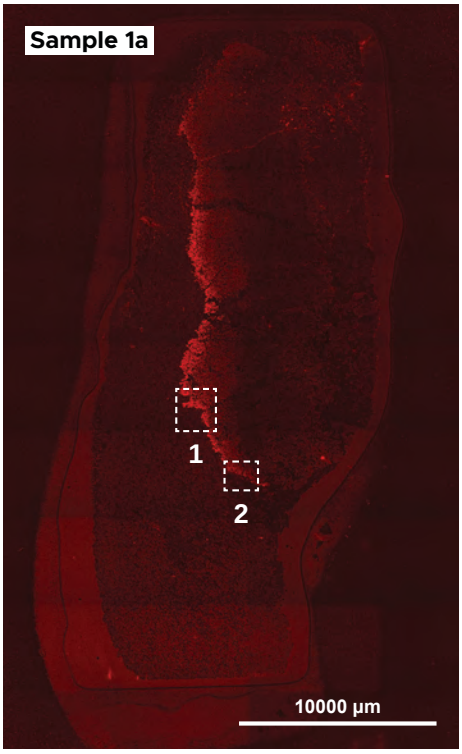

Figure 16 (continued) *This part of the figure an overview of two fluorescent areas in Sample 1a are shown. Images K-M represent fluorescent Zone 1. Images N-Q showcase fluorescent Zone 2. Fluorescence is observed within the edges of cordierite porphyroblasts here a well.*

4.0 Discussion

This study was performed to test the hypothesis that the features observed at Södra Sandvik locality on Utö are of biotic origin. A falsification method will be adopted in this section to discuss both biotic and abiotic explanations for the analyzed features. Additionally, this section will also apply the seven criteria for depositional habitat and identification of MISS proposed by Noffke *et al.* (2013). These criteria have been used in more than 14 studies in order to identify MISS both in ancient and modern sites.

Criteria For MISS Depositional Habitat and Identification Proposed by Noffke *at al.* (2013):

1. MISS occur in rocks of not more than low-grade metamorphosis.
The Södra Sandvik outcrop has undergone several metamorphic events evidenced by both field and petrographic observations. Key evidence is the presence of a combination of biotite, quartz, muscovite and cordierite, indicating a medium grade metamorphic event, while the presence of sagenitic texture, sericitization and reaction rims serve as an evidence of at least one retrograde event. Additionally, field evidence such as crenulation cleavage indicates multiple deformational and metamorphic events as well. Which is consistent with the two phases of low to low-medium metamorphic grades metamorphism within the amphibolite facies reported by Skelton *et al.* (2018). Metamorphism can modify or even destroy biogenic signatures. Since the outcrop has experiences at least one medium grade metamorphic event with potential additional metamorphic overprints, this criterion can not be fulfilled.

While according to Noffke *et al.* (2013), the preservation is deemed impossible in rocks that have undergone medium grade metamorphism, the next six criteria will be explored anyway in order to establish whether the potential MISS could have existed but their trace was destroyed by metamorphism.

2. In stratigraphic sections, MISS occur at turning points of regression-transgression.
No evidence of regression-transgression was identified in the logged sequence, indicating that the outcrop was at some point exposed above water. The depositional facies of the outcrop were identified as a medial to distal turbidite system, likely situated on a slope deepening towards the NE on a continental shelf. The presence of concretions suggests approximate water depth of 40-100m based on modern studies by Kaikkonen *et al.* (2019). The presence of subaqueous current ripples at the end of the outcrop also suggests that the outcrop was submerged under water during deposition. Since turbidites form under water and no sea level changes were recorded in the log, this criterion cannot be fulfilled.

3. MISS occur in the depositional "microbial mat facies".
Noffke *et al.* (2013) do not specifically outline a distinct depositional setting. Both Noffke *et al.* (2013) and Konhauser (2007) state that modern analogies of MISS can survive in a various environments, from shallow marine settings to anoxic basins, hypersaline systems and can even be resistant to high energy events. The presence of concretions suggests a calmer environment in the first two sections of the outcrop compared to Section 3B, where current ripples were identified an the number of concretions decreased. While MISS could potentially form in a turbidite system during longer calm periods, it is uncertain if such periods would be long enough and sufficient for a microbial colony to establish itself. Perhaps, a study of a modern turbidite environment in a similar setting could help to clarify this. While this criterion allows for broad interpretation, it does not prove a biotic origin of the outcrop.

4. The distribution pattern of MISS reflects the average hydraulic pattern in a depositional area.
There is no clear correlation between the laminations and other features observed at Södra Sandvik and hydraulic conditions that would indicate biotic origin. MISS typically form in environments where stabilization of sediments is possible. Since the sediments were most likely transported and deposited by turbidity flows, which are episodic gravity driven flows. The analysis of Ripple Index and Ripple Symmetry supports the transport by a unidirectional current, consistent with turbidity current. Such features as laminations could have formed abiotically due to the gravity driven flows rather than mineral stabilization. Furthermore, soft sediment deformation structures such features as convolute laminations, load clasts and ball-and-pillow

structures indicate sediment loading and rapid deposition, conditions inconsistent with proper microbial mat development.

5. The fossil MISS resemble strongly or are identical in geometries and dimensions to modern ones.
The observed features in the field do resemble modern MISS. The structures presented in field sketches in Fig. 3 (Section 3.1) include a potential mat roll-up fragment and irregularly crinkled mat surfaces shown in Sketch A as well as sinoidal structures and small corrugations and undulations with preferential thickening over small surface irregularities are indicative of microbial activity presented in Sketch B. These morphologies suggest that this criterion based on visual identification is met.

6. The MISS include microtextures that represent, or were caused by, or are related to, ancient biofilms and microbial mats.
No microtextures indicative of microbial activity were identified. The SEM analysis also revealed that the laminations are mineralogically controlled and exhibit sharp, well-defined boundaries rather than diffuse and irregular boundaries indicative of microbial mats. Furthermore, no other micro morphologies expected to be preserved in microbial mats were discovered, for example, filamentous networks, EPS-related structures or trapped sediment grains etc. Fluorescence microscopy showed no evidence of organic remains. The absence of these features suggests that this criterion is not fulfilled.

7. Geochemical analyses support the interpretation as MISS.
Geochemical data does not support a biotic origin. SEM-EDS analysis detected no carbon within the laminations, which means that there is no preserved organic material in the samples. One of the arguments for microbial activity mentioned in Section 3.1 was the presence of iron observed in the outcrop as well as the iron rich concretions, since microbial mats can facilitate Fe(II) oxidation and binding of ferric minerals. However, SEM-EDS analysis did not reveal any minerals typically associated with MISS and iron cycling minerals such as pyrite, hematite or goethite. Iron incorporated into metamorphic minerals such as cordierite and biotite could be explained by detrital input or fluid-driven element redistribution rather then biotic activity. The REEs observed in monazite and zircon grains as well as diffuse trace presence across the samples does not correspond with the laminations, indicating a metamorphic or detrital origin rather than microbial. These findings suggest that this criterion is not fulfilled.

The criteria by Noffke *et al.* (2013) demonstrates that even though the structures observed in the field visually resemble MISS, the remaining of the requirements do not align with known MISS occurrences based on modern studies and strongly suggest an abiotic origin for the structures observed in the outcrop. While this does not entirely exclude the possibility that microbial mats have once existed, the medium grade metamorphic overprint did not leave any evidence to confirm their presence.

Falsification Approach

A falsification approach is applied to consider if observed sedimentary structures at Södra Sandvik can be explained by potential abiotic processes. The evidence suggests a medial to distal turbidite system. The presence of laminations, current ripples, soft sediment deformation features and slumping aligns with depositional features in a turbidite system. In a medial to distal turbidite setting sediments such as silty sand are transported and deposited first, while clay and mud remain in suspension and settle gradually as the turbidity current wanes, forming alternating light and dark laminations. Wavy laminations, both continuous and discontinuous can be commonly found in turbidites and can be interpreted as the product of low-energy currents with finer particles settling from suspension. Crinkly texture of the laminations could be possibly explained by soft sediment deformation, compaction and dewatering processes rather than microbial activity. Incipient ball-and pillow structures and convolute laminations are present in the very first section of the log and gradually increase in size throughout the outcrop, supporting soft sediment deformation processes happening across the whole outcrop. The feature similar to a roll up clast (depicted in Sketch A in Fig. 3) could have formed due to sediment loading, similar to the incipient ball-and-pillow structures present in

the same section. Additionally, the fine laminations with thicker dark laminations over crests (depicted in Sketch B, Fig. 3) could be explained by differential sedimentation and liquefaction. Thus, the formation of the laminations and other structures can be explained abiogenically, which is also supported by the lack of preserved organic material and by the geochemical or mineralogical analyses. Additionally, concretions and the presence of iron in cordierites and biotites can be explained by diagenetic processes rather than biological activity. Furthermore, the origin of REEs observed in monazite and zircon grains as well as the diffuse trace presence across the samples can be attributed to either detrital input or redistribution by metamorphic fluids. If the concretions formed due to microbial metabolic activity, known to accumulate REEs, the amount of REEs would be expected to decrease throughout the outcrop along with the decreasing number of concretions and iron-baring minerals. This supports the presence of REEs due to detrital input or redistribution by metamorphic fluids. While biofilms are present in most sedimentary environments according to Noffke *et al.* (2022), the key question is whether they have altered the sediment enough in order to form MISS and leave diagnostic structures. No diagnostic structures have been discovered.

5.0 Conclusion

This study tested the hypothesis that the observed features at Södra Sandvik are of biotic origin by applying a falsification approach and the MISS identification criteria used in the studies of modern and ancient MISS sites. The observed sedimentary structures, including laminations, concretions, soft sediment deformation features and ripples are consistent with a medial to distal turbidite system transitioning from a shallower environment into a deeper setting. Although some features resemble MISS visually, no preserved organic material, biogenic microtextures or diagnostic of past microbial activity minerals were discovered. This lack of evidence points to abiotic origin of the features, with their formation explained through physical and diagenetic processes in a turbidite system. Additionally, REEs found in the samples were found to be associated with monazite and zircon crystals or as trace amounts distributed across the whole outcrop and have no correlation to the laminations, suggesting detrital or metamorphic origin. Even if microbial mats once existed, metamorphic overprint has likely destroyed any potential evidence of microbial existence. Therefore, the hypothesis cannot be confirmed.

Acknowledgements

This bachelor's thesis was carried out at Department of Geological Sciences at Stockholm University. Its completion would not have been possible without the support and guidance of several institutions and individuals to whom I am sincerely grateful. I would like to express my gratitude to my supervisor, Christophe Dupraz, for his guidance throughout this project and for providing us with the opportunity to learn new analytical techniques, as well as a possibility to visit and work in the laboratory of the University of Fribourg. A special thank you to the University of Fribourg for welcoming us so warmly, in particular to Matteo Mangiagalli for his teaching us fluorescence microscopy, and Christoph Neururer for patiently instructing us in Scanning Electron Microscopy and Energy Dispersive X-ray Spectrometry. I am also grateful to Alasdair Skelton for his advice in selecting the study outcrop, which turned out to be highly insightful. Furthermore, I am also sincerely thankful to Heidelberg Materials laboratory in Slite (Cementa AB on Gotland) for granting me access to their petrographic microscope at any time and for their welcoming and accommodating support. A special thank you to José Aguirre Castillo and Halina Siewiora for making this possible and for taking their time to organize everything and even assist me. Lastly, I am deeply thankful to my fieldwork partner, Lain Velasco, for being an excellent and fun company in the field, engaging conversations and unwavering patience in holding field scales for photographs in the most impractical positions.

6.0 Reference List

Allaby, M. 2020. *A Dictionary of Geology and Earth Sciences* (5th ed.). Oxford University Press, Oxford, UK.

Barker, A. J. 2014. *A Key for Identification of Rock-forming Minerals in Thin-Section*. CRC Press/Balkema, Leiden, Netherlands.

Baas, J.H. 1978. Ripple, ripple mark, ripple structure. *Sedimentology*. *Encyclopedia of Earth Science*. Springer, Berlin, Heidelberg. https://doi.org/10.1007/3-540-31079-7_172

Dupraz, C., Reid, R. P., Braissant, O., Decho, A. W., Norman, R. S. & Visscher, P. T. 2009. Processes of carbonate precipitation in modern microbial mats. *Earth-Science Reviews*, 96, 141-162. https://doi.org/10.1016/j.earscirev.2008.10.005

El Albani, A., Bengtson, S., Canfield, D. E., Riboulleau, A., Bard, C. R., Macchiarelli, R., Pemba, L. N., Ham marlund, E., Meunier, A., Mouele, I. M., Benzerara, K., Bernard, S., Boulvais, P., Chaussidon, M., Cesari, C., Fontaine, C., Chi-Fru, E., Ruiz, J. M. G., Gauthier-Lafaye, F., Mazurier, A., Pierson-Wick mann, A. C., Rouxel, O., Trentesaux, A., Vecoli, M., Versteegh, G. J. G., White, L., Whitehouse, M. & Bekker, A. 2014. The 2.1 Ga Old Francevillian biota: Biogenicity, taphonomy and biodiversity. *Plos One*, 9, e99438. https://doi.org/10.1371/journal.pone.0099438

Fossen, H. 2016. *Structural Geology* (2nd ed.). Cambridge University Press, Cambridge, UK.

Gavelin, S., Lundström, I. & Norström, S. 1976: *Svecofennian stratigraphy on Utö, Stockholm Archipelago. Correlations with Finland and Sweden*. Sveriges Geologiska Undersökning. Serie C Nr 719. C David sons Boktryckeri AB, Växjö.

Gray, D. R. 1987. Crenulation cleavages. *Structural Geology and Tectonics. Encyclopedia of Earth Science*. Springer, Berlin, Heidelberg. https://doi.org/10.1007/3-540-31080-0_22

Javaux, E. J. & Benzerara, K. 2009. Microfossils. *Comptes Rendus Palevol,* 8, 605-615. https://doi.org/10.1016/j.crpv.2009.04.004

Jellinek, A. M., Lenardic, A. & Pierrehumbert, R. T. 2020. Ice, fire, or fizzle: The climate footprint of Earth's supercontinental cycles. *Geochemistry, Geophysics, Geosystems,* 21, e2019GC008464. https://doi.org/10.1029/2019GC008464

Jerram, D. & Caddick, M. 2022. *The Field Description of Metamorphic Rocks* (2nd ed.). John Wiley & Sons Ltd, West Sussex, UK

Jobe, Z. R., Lowe, D. R. & Morris, W. R. 2012. Climbing-ripple successions in turbidite systems: depositional environments, sedimentation rates and accumulation times. *Sedimentology*, 59(3), 867–898. https://doi-org.ezp.sub.su.se/10.1111/j.1365-3091.2011.01283.x

Kaikkonen, L., Virtanen, E. A., Kostamo, K., Lappalainen, J. & Kotilainen, A. T. 2019. Extensive coverage of marine mineral concretions revealed in shallow shelf sea areas. *Frontiers in Marine Science*, 6, 541. https://doi.org/10.3389/fmars.2019.00541

Klein, C. & Philpotts, A. R. 2017. *Earth Materials: Introduction to Mineralogy and Petrology* (2nd ed.). Cambridge University Press, Cambridge, UK.

Konhauser, K. 2007. *Introduction to Geomicrobiology*. Blackwell Publishing, UK.

MacKenzie, W. S., Adams, A. E. & Brodie & K. H. 2017. *Rocks and Minerals in Thin Section: A Colour Atlas* (2nd ed.). CRC Press/Balkema, Leiden, Netherlands.

Marshak, S. 2001. *Earth: Portrait of a Planet* (5th ed.). W. W. Norton & Company, Inc., New York, US

Nesse, W. D. 2000. *Introduction to Mineralogy*. Oxford University Press, New York, US

Nichols, G. 2023. *Sedimentology and Stratigraphy* (3rd ed.). John Wiley & Sons Ltd, West Sussex, UK.

Noffke, N., Beraldi-Campesi, H., Callefo, F., Carmona, N., Cuadrado, D. G., Hickman-Lewis, K., Homann, M., Mitchell, R., Sheldon, N., Westall, F. & Xiao, S. 2022. Part B, Volume 2, Chapter 5: *Microbially induced sedimentary structures (MISS)*. Treatise Online, 162, 1–29.

Noffke, N., Christian, D., Wacey, D. & Hazen, R. M. 2013. Microbially induced sedimentary structures recording an ancient ecosystem in the ca. 3.48 billion-year-old Dresser Formation, Pilbara, Western Australia. *Astrobiology*, 13(12), 1103–1124. https://doi.org/10.1089/ast.2013.1030

Okoro, A. U., Onuoha, K. M. & Okogbue, C. O. 2011. Oscillatory ripples, evaluation of ancient wave climates and epierogeny in the Anambra basin and the Afikpo sub-basin, Southeastern Nigeria. *Global Journal of Geological Sciences*, 9(1), 11-17. https://api.semanticscholar.org/CorpusID:59404570

Olejarz, J., Iwasa, Y., Knoll, A. H. & Nowak, M. A. 2021. The Great Oxygenation Event as a consequence of ecological dynamics modulated by planetary change. *Nature Communications,* 12, 3985. https://doi.org/10.1038/s41467-021-23286-7

Passchier, C. W. & Trouw, R. A. J. 2005. *Microtectonics* (2nd ed.). Springer-Verlag, Berlin Heidelberg.

Pereira, I., Bruand, E., Nicollet, C., Koga, K. T. & Brovarone, A. V. 2023. Ti-bearing minerals: From the ocean floor to subduction and back. *Journal of Petrology*, 64(7), egad041. https://doi.org/10.1093/petrology/egad041

Philpotts, A. R. & Ague, J. J. 2009. *Principles of Igneous and Metamorphic Petrology* (2nd ed.). Cambridge University Press, Cambridge, UK.

Rajlich, P. 1991. Kinematics of crenulation cleavage development: Example from the Upper Devonian rocks from northeast of the Bohemian massif, Czechoslovakia. *Tectonophysics*, 190, 193–208. https://doi.org/10.1016/0040-1951(91)90430-Z

SGU, 2024: *Map of Bedrock 1 Million*. Web-page, https://apps.sgu.se/kartvisare/kartvisare-berggrund-1-miljon.html.

Shau, Y.-H., Yang, H.-Y. & Peacor, D. R. 1991. On oriented titanite and rutile inclusions in sagenitic biotite. *American Mineralogist*, 76, 1205–1217.

Skelton, A. 2023. Geology of Utö. Unpublished teaching material, Stockholm University.

Skelton, A., Mansfeld, J., Ahlin, S., Lundqvist, T., Linde, J. & Nilsson, J. 2018. A compilation of metamorphic pressure–temperature estimates from the Svecofennian province of Eastern and Central Sweden. *GFF*, 140, 1-10. https://doi.org/10.1080/11035897.2017.1414074

Talbot, C. J. 2008. Palaeoproterozoic crustal building in NE Utö, southern Svecofennides Sweden. *GFF,* 130, pp. 49–70. https://doi.org/10.1080/11035890801302049

Tanner, W. F. 1967. Ripple mark indices and their uses. *Sedimentology*, 9: 89-104. https://doi-org.ezp.sub.su.se/10.1111/j.1365-3091.1967.tb01332.x

Tucker, M. E. 2011. *Sedimentary Rocks in the Field: A Practical Guide* (4th ed.). John Wiley & Sons Ltd, West Sussex, UK.

Vernon, R. H. & Clarke, G. L. 2008. *Principles of Metamorphic Petrology*. Cambridge University Press, Cambridge, UK.

7.0 Appendices

Appendix A - Outcrop Correlation Sketch

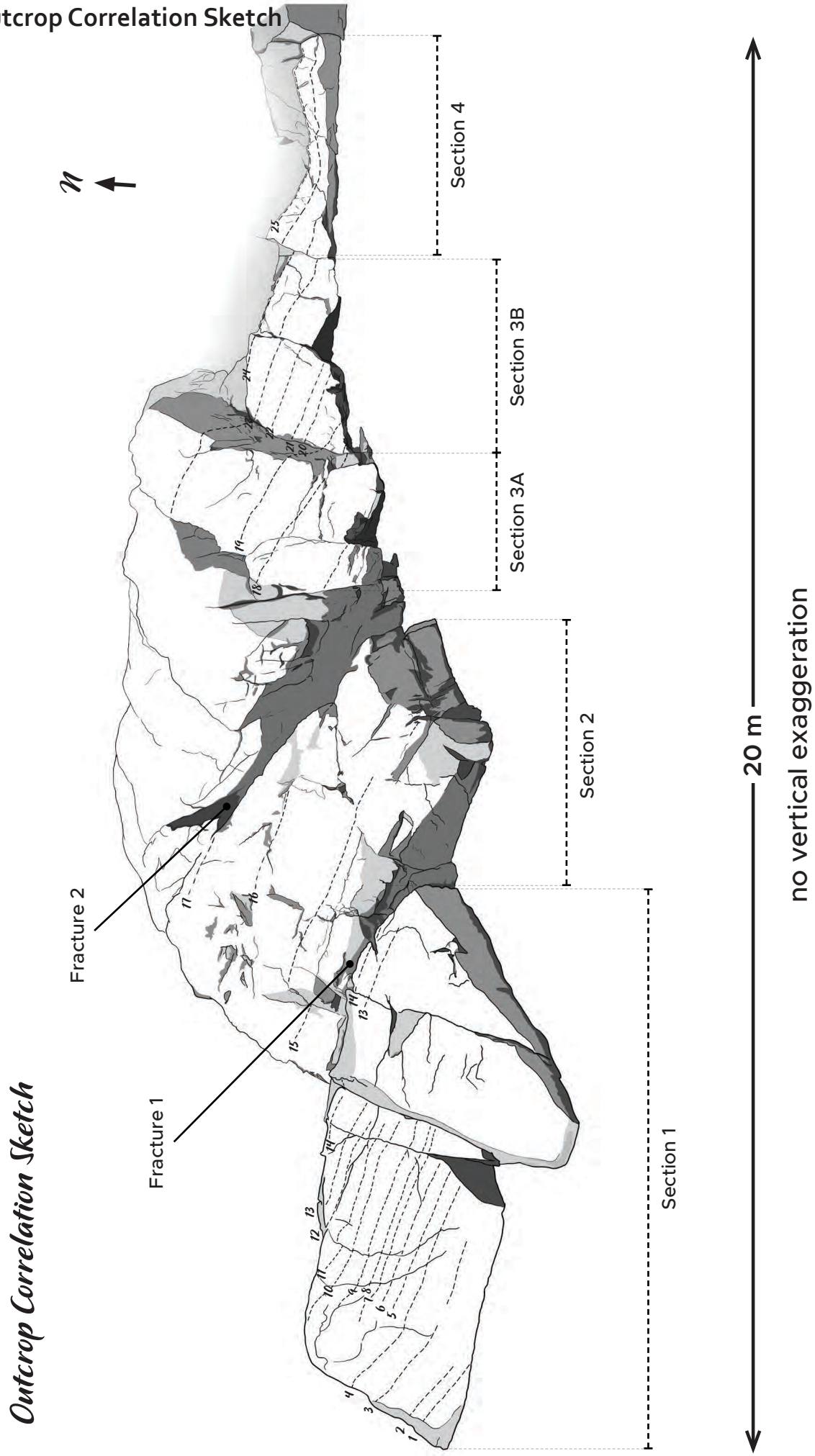

Appendix B - Photographs for Correlation With Sedimentological Log

This Appendix provides overview photographs of the logged sections and close-up photographs of the units.

Section 1

001 - Unit 1

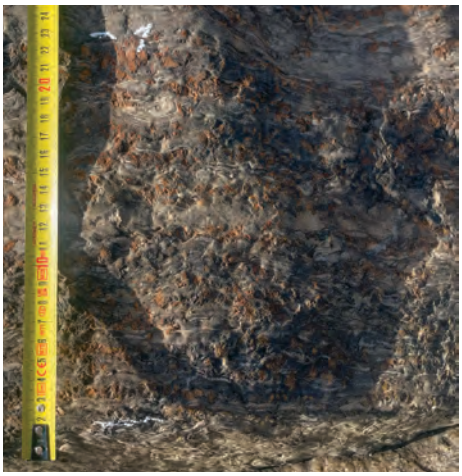

002 - Unit 2

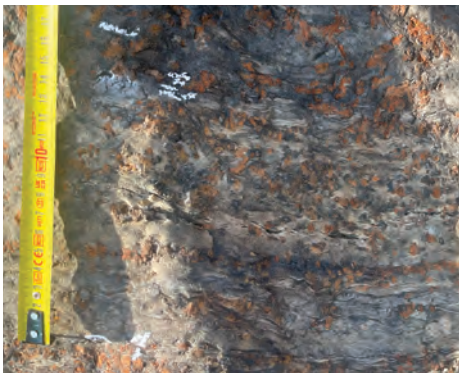

003 - Unit 3

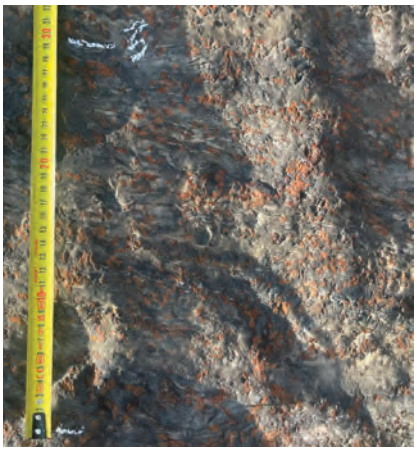

004 - Unit 4

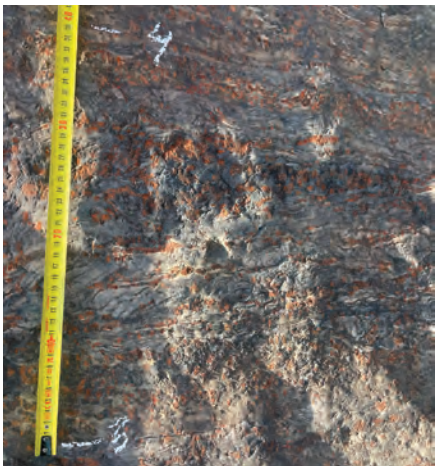

005 - Unit 4 continued

006 - Unit 5

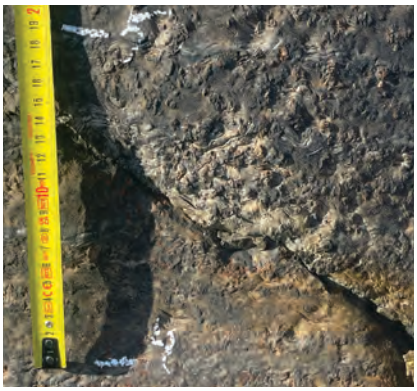

007 - Units 6 and 7

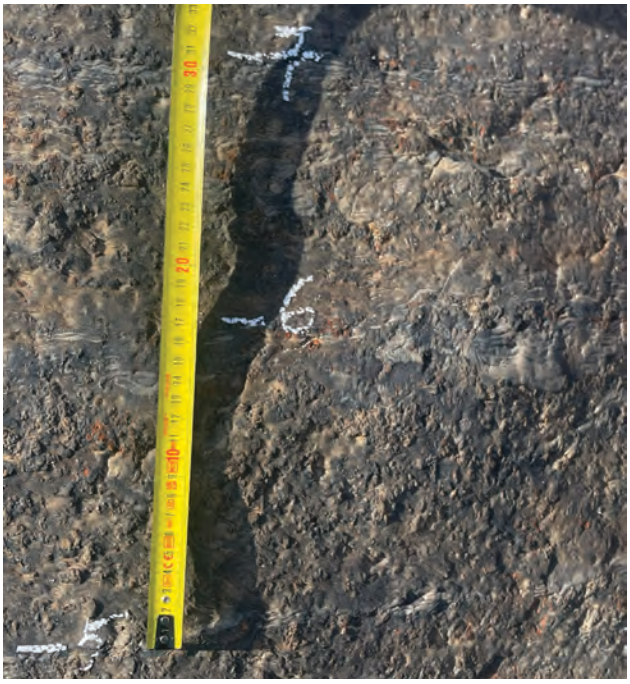

008 - Units 7 to 11

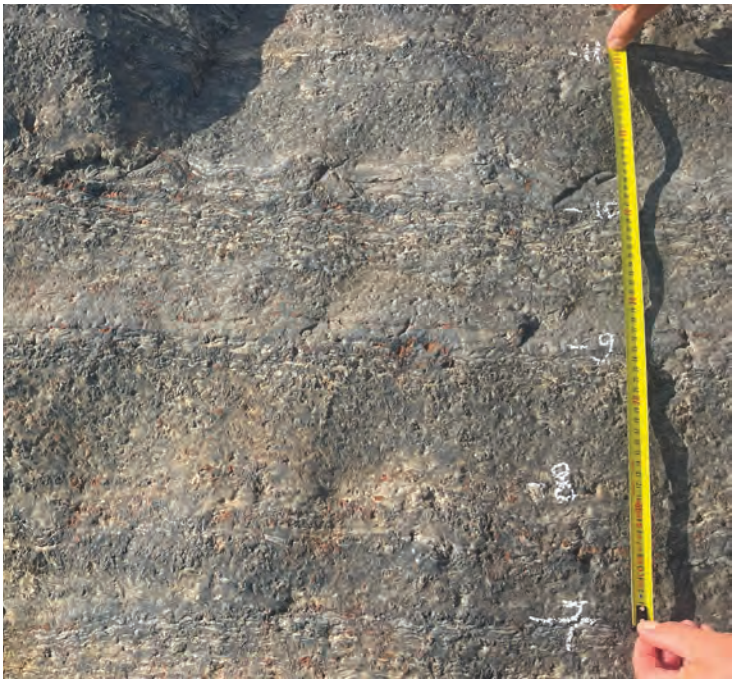

009 - Units 12 and 13

010 - Unit 14

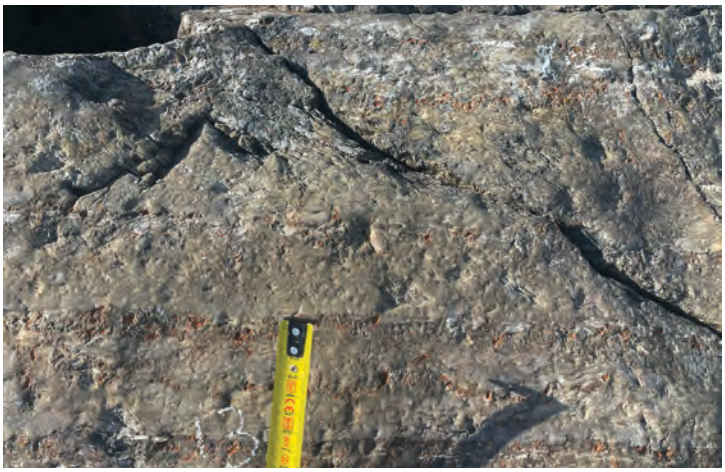

011

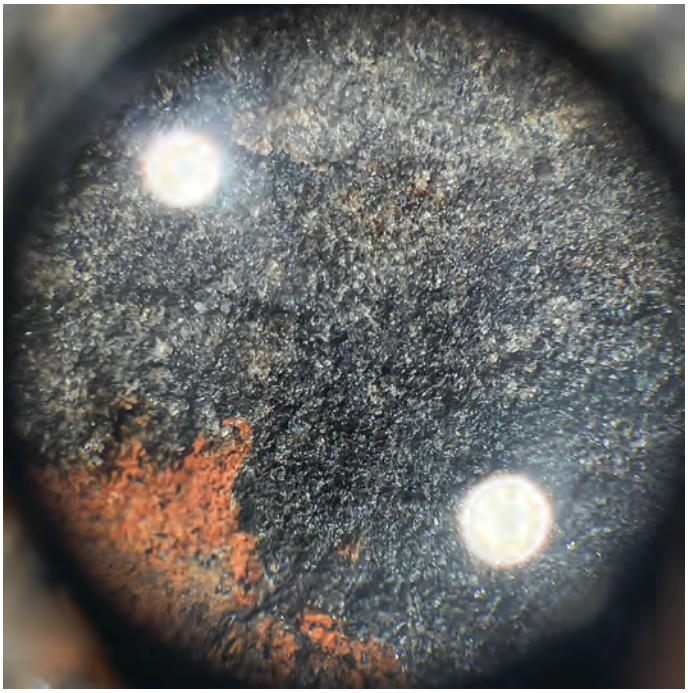

012

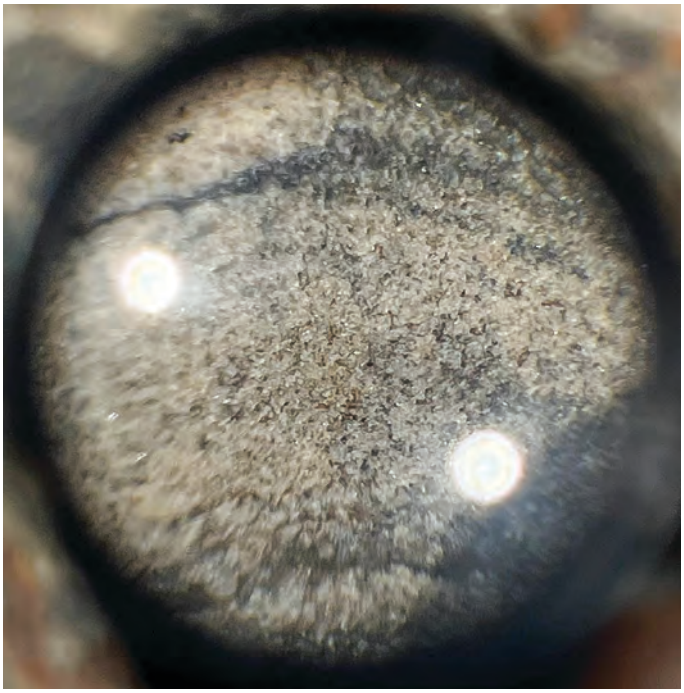

Images of grain sizes under x10 magnification, Section 1. Image 011 demonstrates darker biotite-rich laminations, likely former mud. Image 012 shows lighter areas dominated by silty sand-sized grains from the lighter parts of the section.

Section 2

013 - Units 15-17

014 - Unit 15

015 - Unit 15 continued

016 - Unit 15, possible ball-and-pillow structure

Close-up of a possible ball-and-pillow structure within Unit 15. The area is outlined in the Image 014 above.

017 - Unit 16

018 - Unit 17

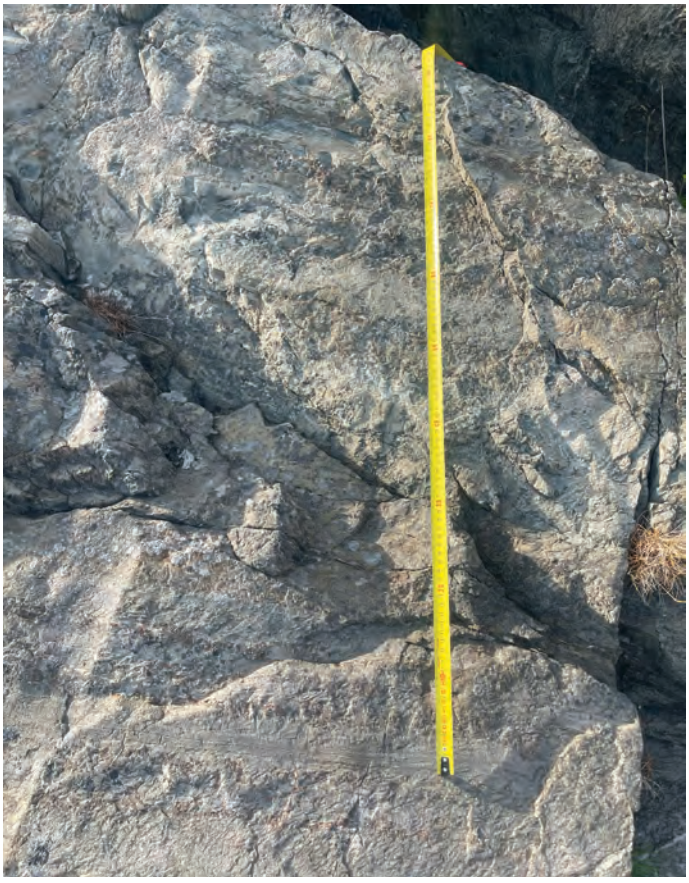

019 - Unit 17

Close-up of the fine laminations within the unit.

020

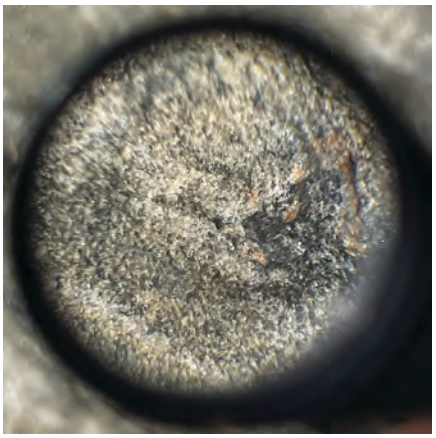

021

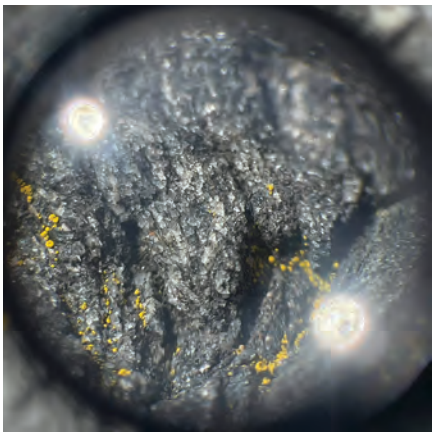

022

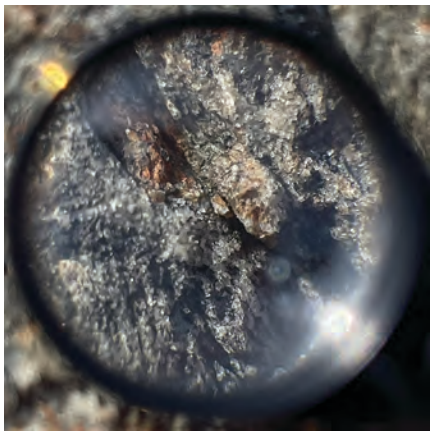

Images of grain size observations under x10 magnification from Section 2. Image 020 shows silty sand-sized grains in lighter areas. Recrystallized quartz within biotite-rich darker areas can be seen in image 021. Image 022 features a rusty cordierite crystal within biotite, partially weathered.

Sections 3A and 3B

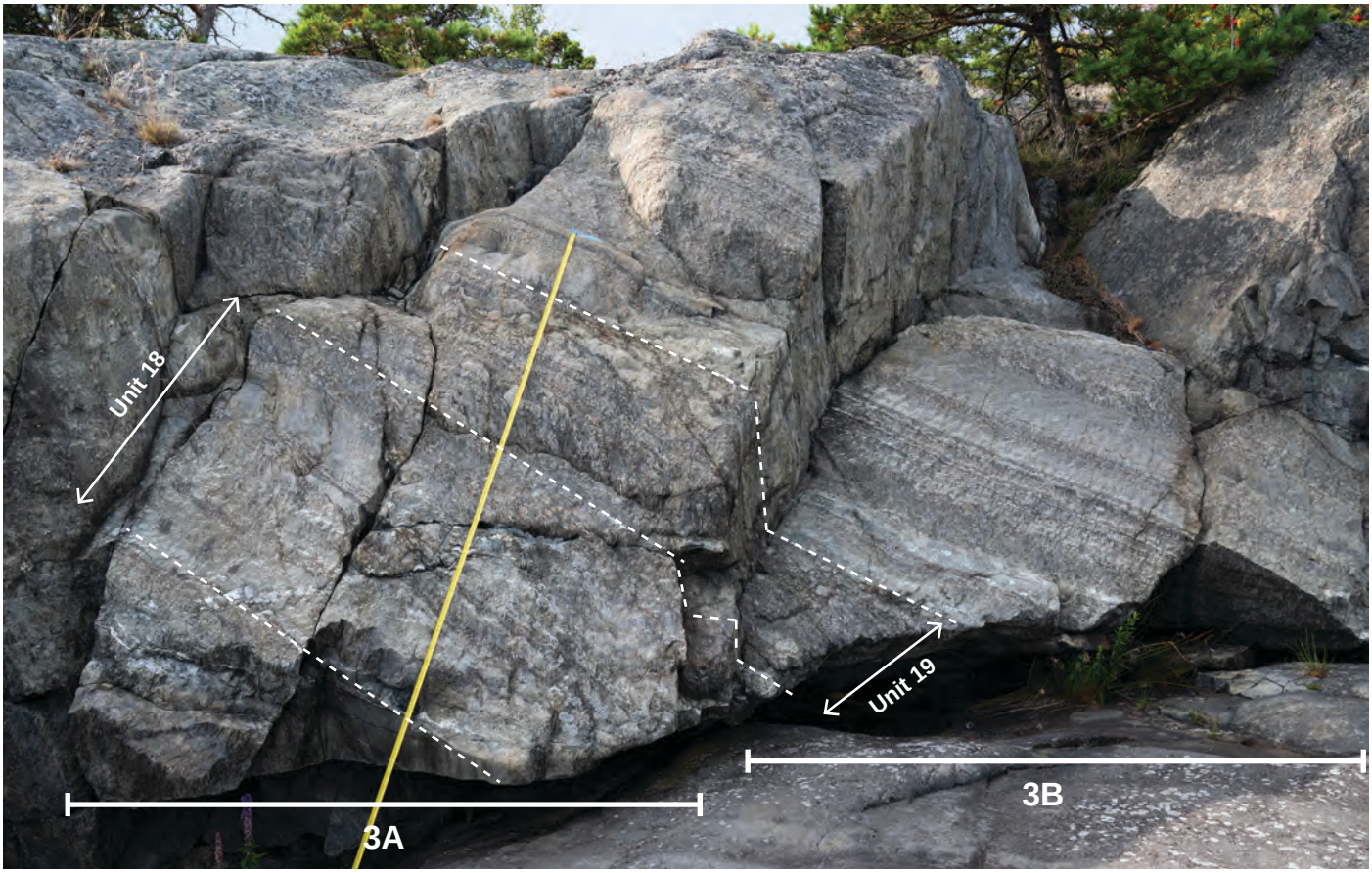

Overview of Sections 3A and 3B. Unit 19 crosses both Section 3A and 3B. Unit 19 was logged as part of Section 3B for clarity as it marks the beginning of this section.

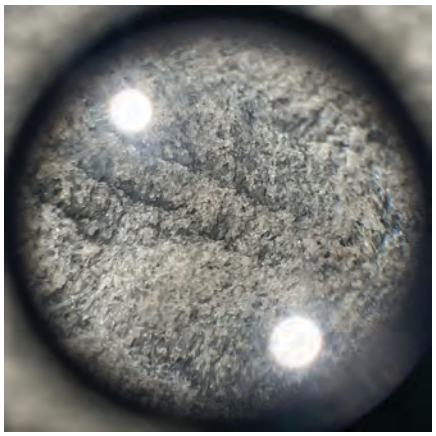

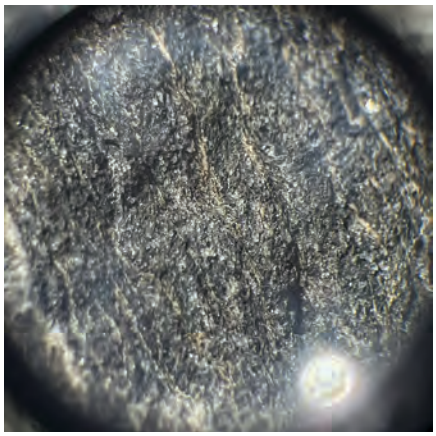

023 (left) and **024 (right)**

Grain size under x10 magnification in Section 3A:

Image 023 shows silty sand-sized grains in a lighter area.

Image 024 shows a biotite rich darker area with clear foliation.

025 - Unit 18

Section 3B

026 - Unit 19 within the whole section

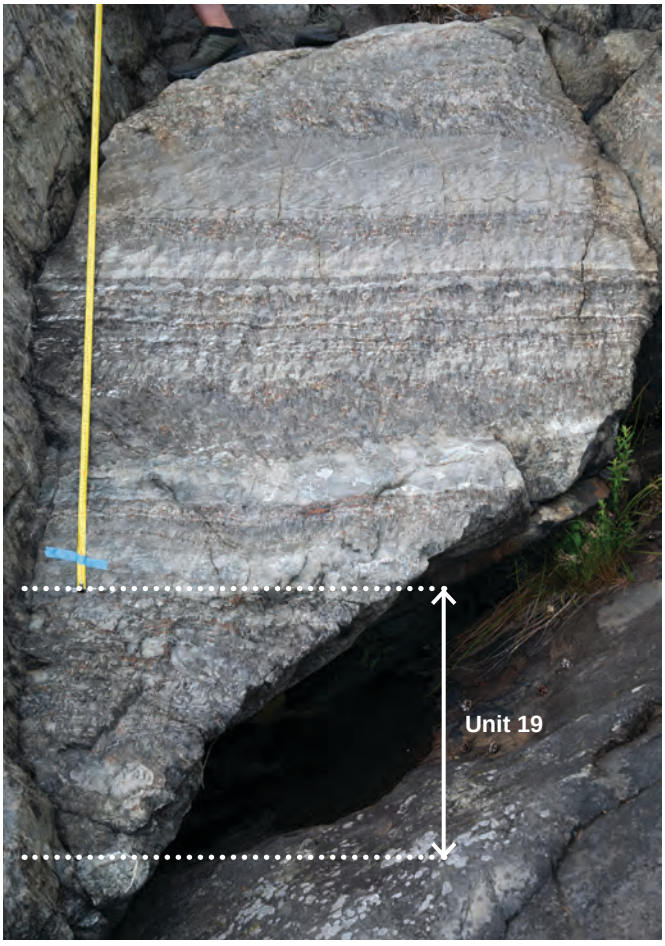

027 - Unit 19 close-up

028 - Unit 19 continued within Section 3A

029 - Close-up of ball-and-pillow structures

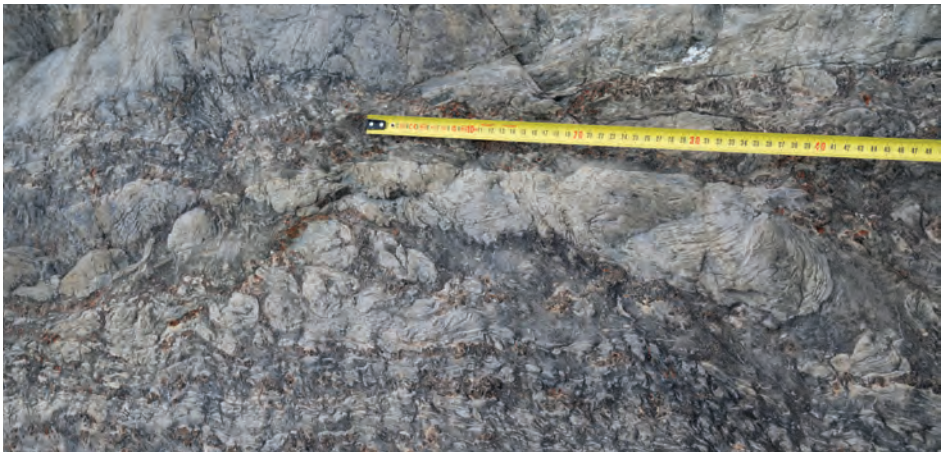

030

031

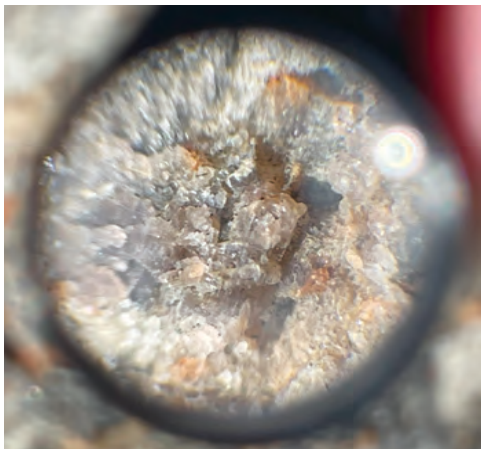

032

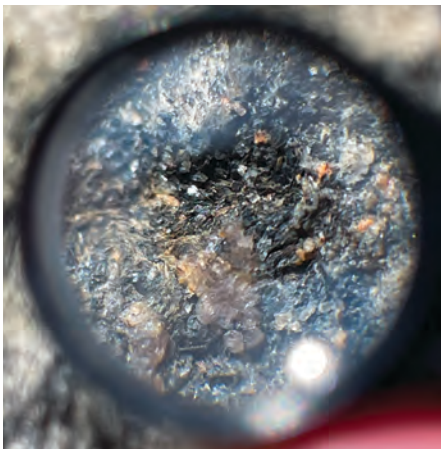

Photographs of grain sizes from Unit 19 (continued in Section 3A, shown in Image 028) with large ball-and-pillow structures. Image 030 shows silty-sand-sized grains in lighter areas. Image 031 shows a potential recrystallized feldspar crystal. Image 032 displays a darker layer containing a feldspar crystal within the biotite-rich matrix.

Section 3B with numbered units 19 to 24

032 - Unit 20

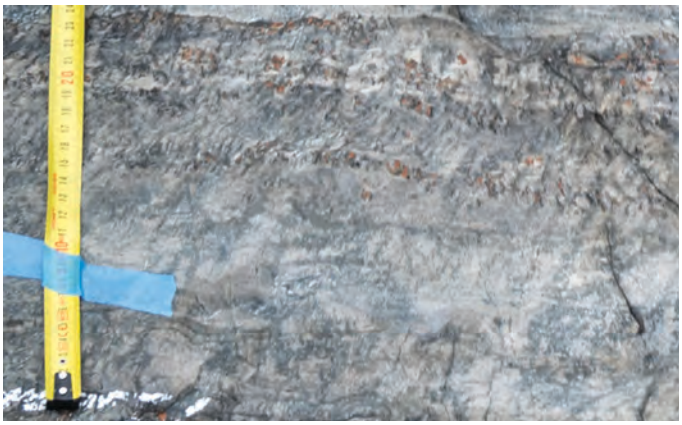

033 - Unit 21

034 - Unit 22

035 - Unit 22, close-up of the 3-4 cm ripples

036 - Unit 23

037 - Unit 24

037

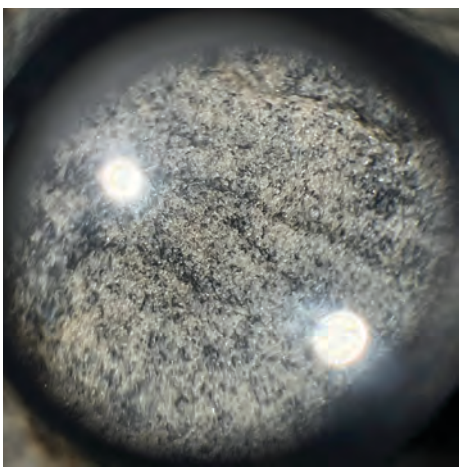

038

039

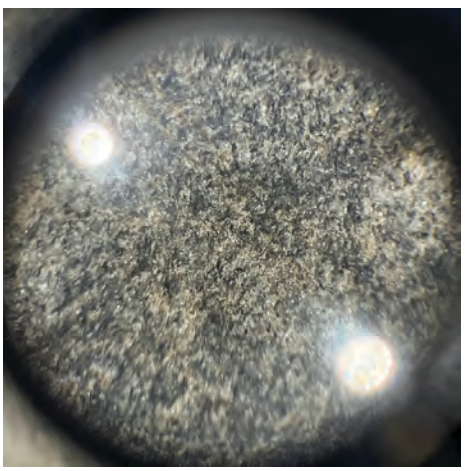

Grain size under x10 magnification from Section 3B. Image 037 shows silty sand-sized grains in lighter areas. Image 038 shows darker biotite-rich layers with recrystallized quartz and rusty-colored cordierites. Image 039 represents an intermediate grey area, which contains a mix of silty sand and biotite.

Section 4

040 - Units 24 and 25

041

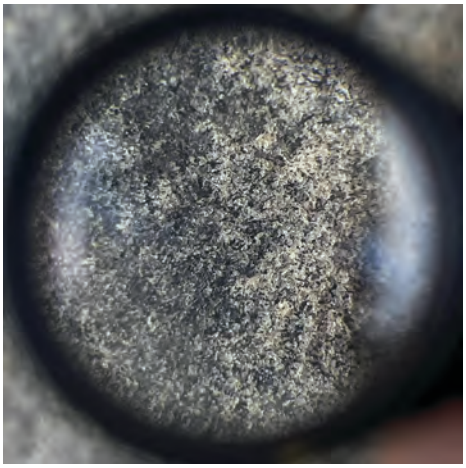

Grain size under x10 magnification from Section 4. Image 041 shows a transitional area between lighter silty sand and darker biotite-rich parts of Unit 25.

Appendix C - Ripple Indices

Fig. C1 Ripple morphology and measurement parameters. Redrawn from Okoro *et al.* (2011)

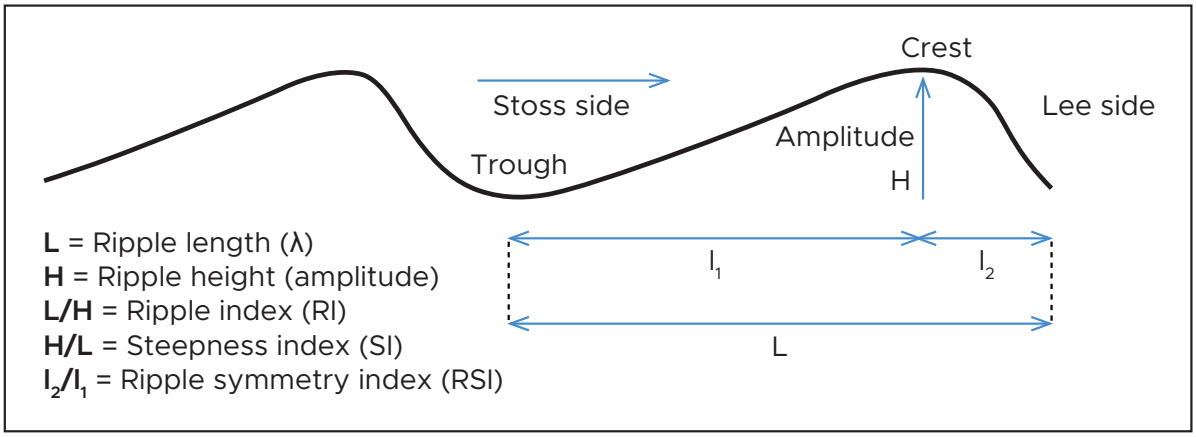

Fig. C2 Five of the most well-preserved ripple marks measured following the parameters illustrated in Fig. C1. Measurements include ripple height (H), length (λ) and symmetry indices (I_1 and I_2).

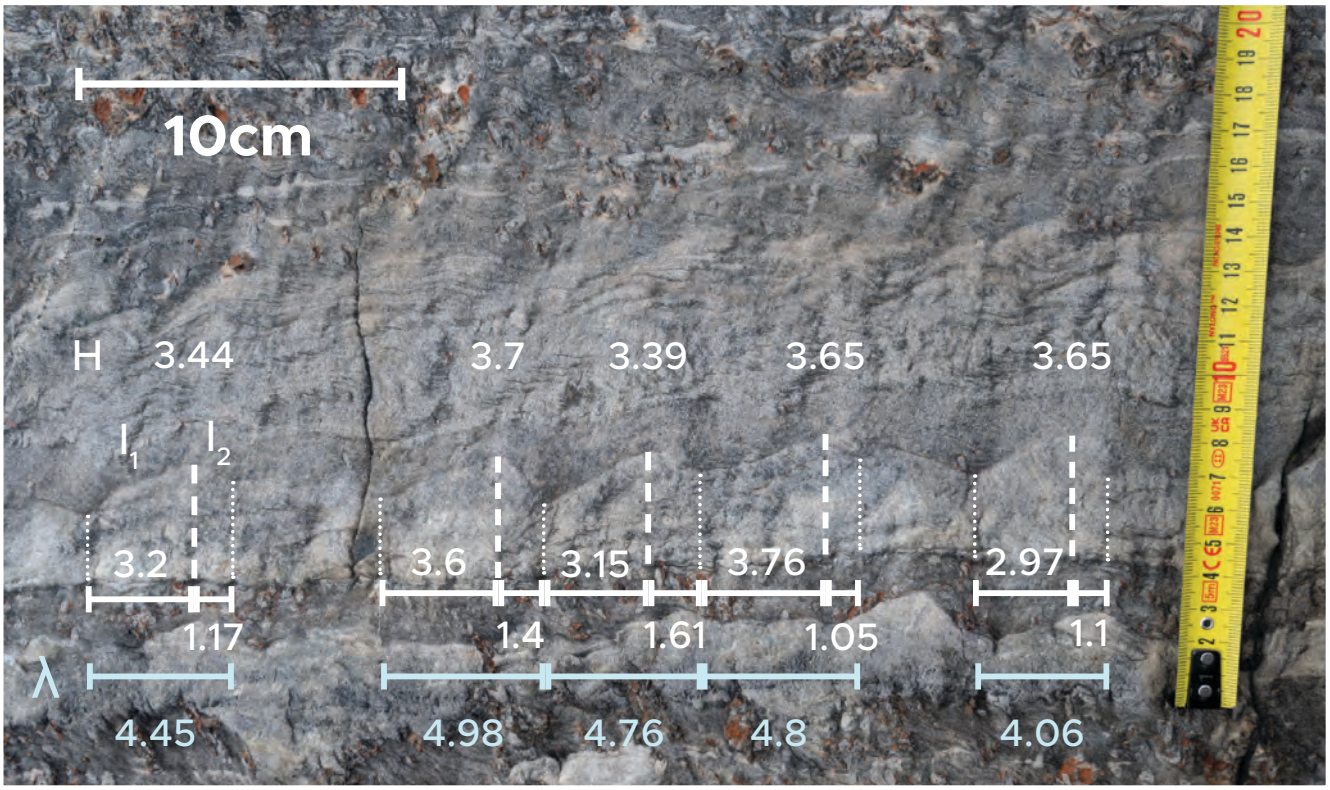

Fig. C3 Morphological measurements of five well-preserved ripple marks: length (L), height (H), symmetry indices (I_1 and I_2), Ripple Index (RI) and Ripple Symmetry Index (RSI).

Ripple #	L (cm)	H (cm)	l_1 (cm)	l_2 (cm)	RI (L/H)	RSI (l_1/l_2)
1	4.45	3.44	3.2	1.17	1.29	2.74
2	4.98	3.7	3.6	1.4	1.35	2.57
3	4.76	3.39	3.15	1.61	1.4	1.96
4	4.8	3.65	3.76	1.05	1.32	3.6
5	4.06	3.65	2.97	1.1	1.11	2.7
Mean	4.6	3.5	3.34	1.27	1.29	2.63

Appendix D - Brightfield and Fluorescence Scans

Green fluorescence (FITC) images were omitted due to the absence of signal, since the samples were coated by resin. Brightfield and TexRed fluorescence images are presented for all samples collected at Södra Sandvik locality below.

Samples collected at the start of the logged area in Section 1 (Samples 1, 1a, 9 and 11):

Sample 1 (Round structure)


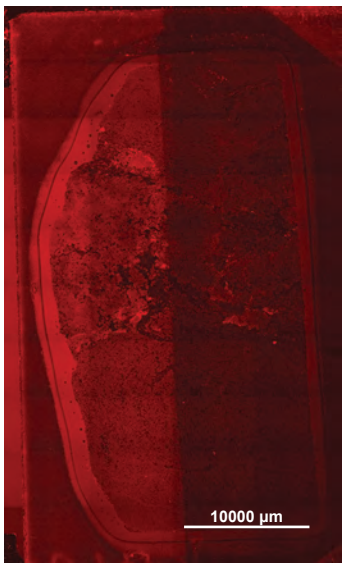


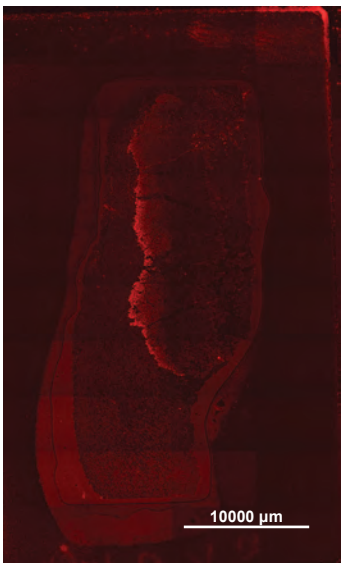

Sample 9 (Thin laminations)


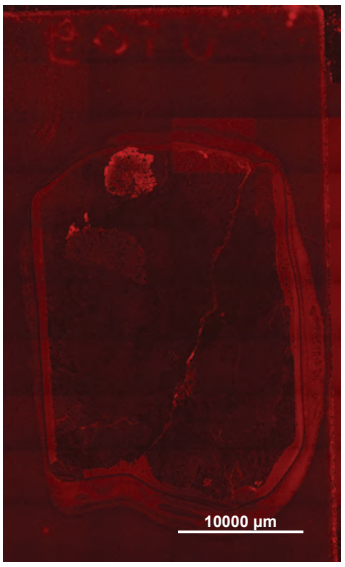

Sample 11 (Laminations, beginning of Section 1)


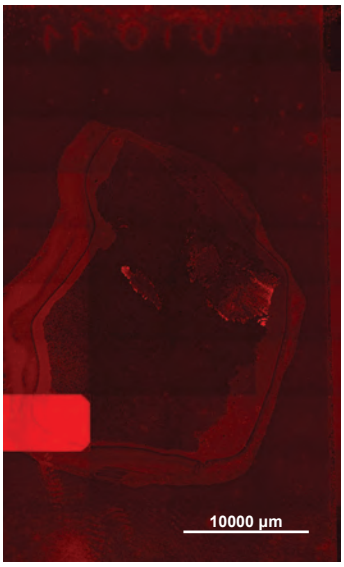

Continued on the next page

Samples collected at the end of the logged area, just past Section 4 (7, 8, 10, 15 and 16):

Sample 7 (Laminations)

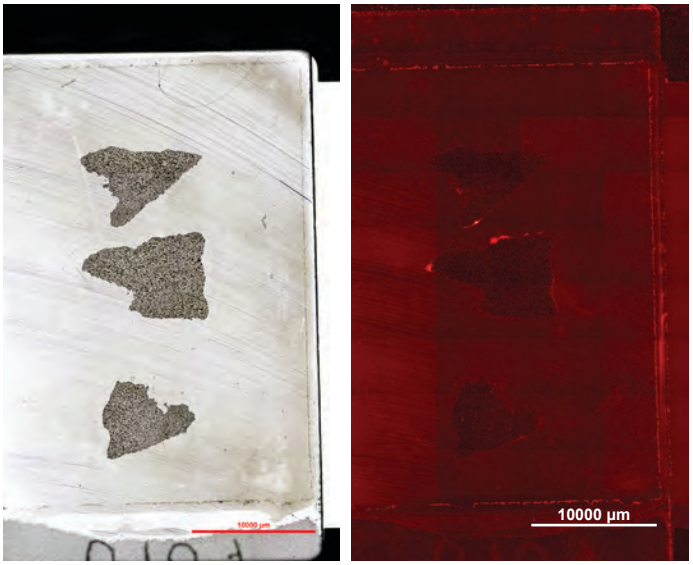

Sample 8 (Laminations)

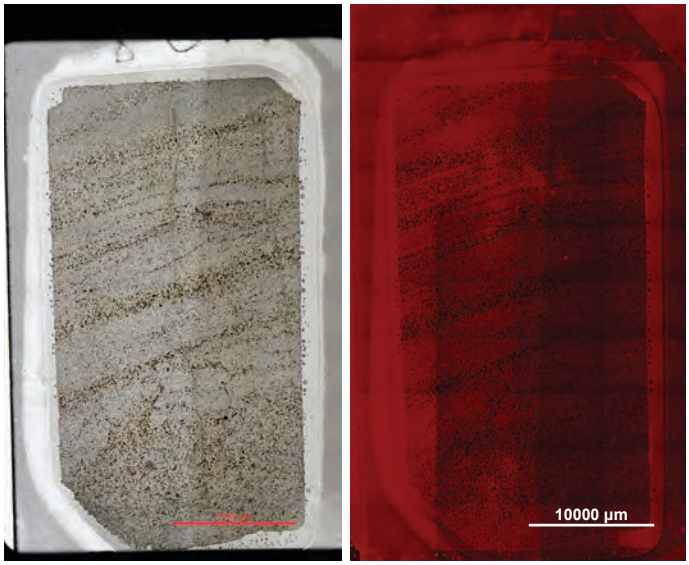

Sample 10 (Load clasts)

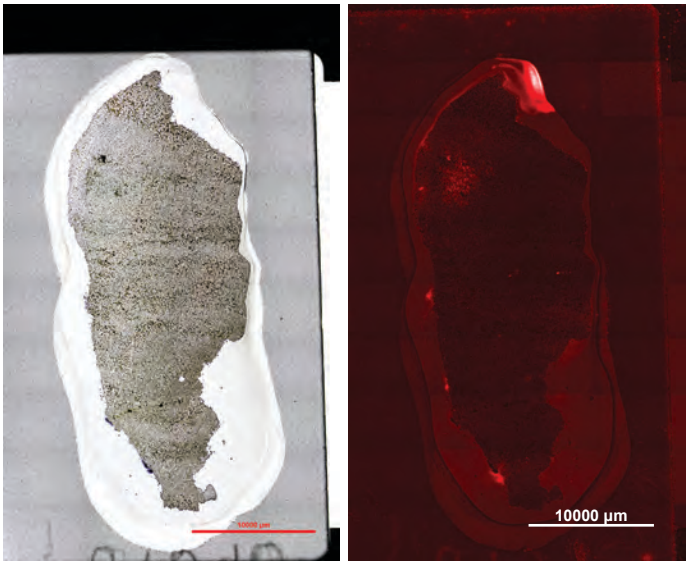

Sample 15 (Load structures)

Sample 16 (Laminations)

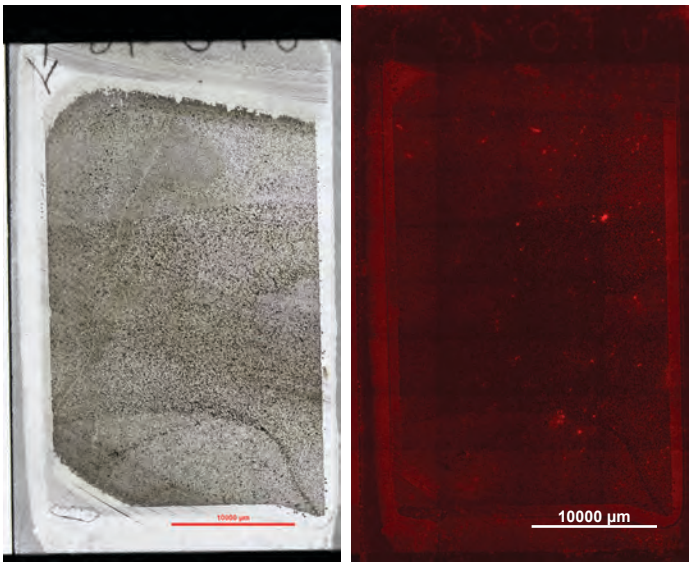

Appendix E - Fluorescence Scans and Photomicrographs of Fluorescent Areas

Sample 9

This is an overview of two fluorescent areas in Sample 9 marked with dashed a white line in the thin section scan in the right lower corner of the figure. Images A-C represent fluorescent Zone 1. Images D-G represent fluorescent Zone 2 with images F-G providing a closer look at the same area. Fluorescence is observed within the edges of cordierite prophyroblasts here as well.

Fluorescent area 1:

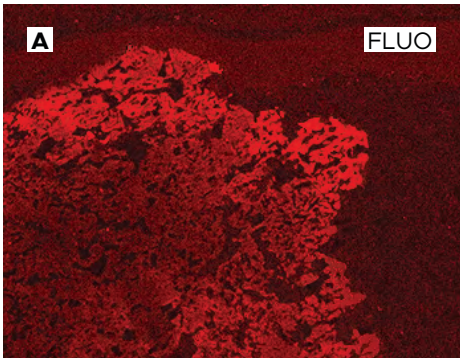

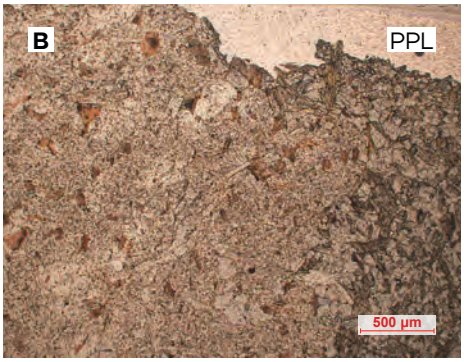

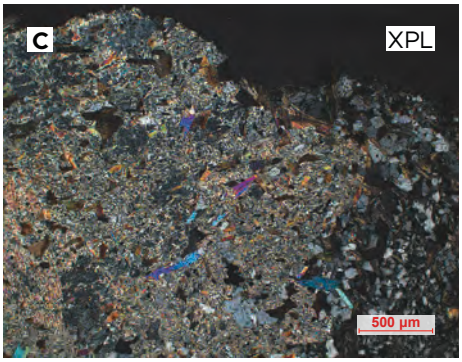

Fluorescent area 2:

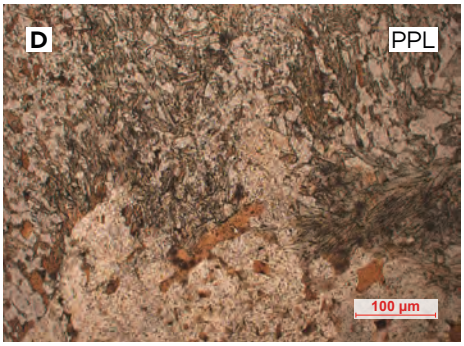

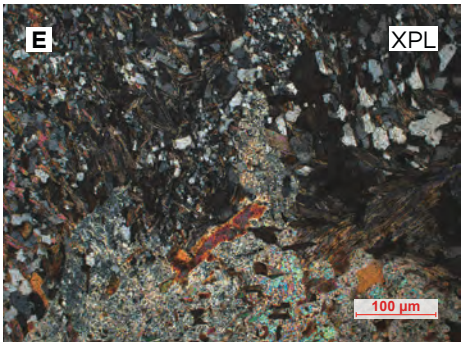

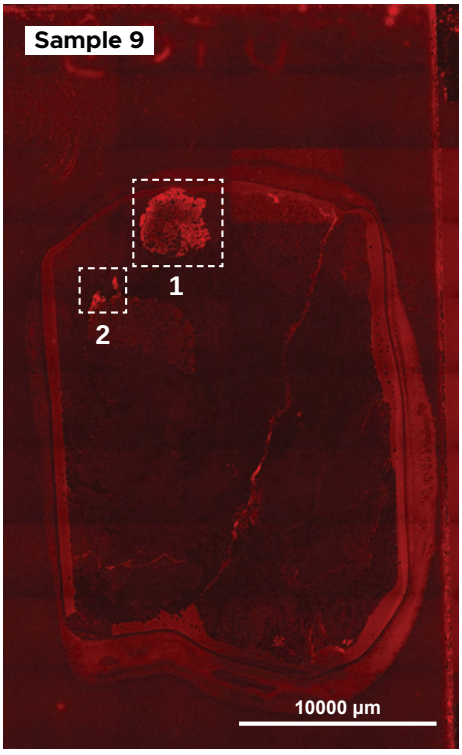

Fluorescent area 2 (close-up):

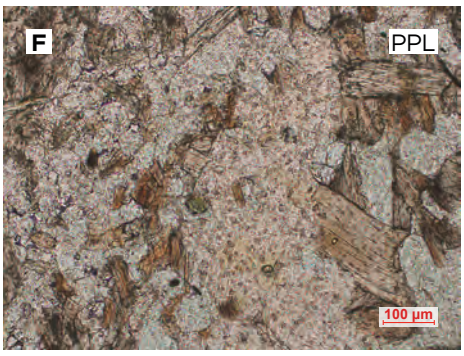

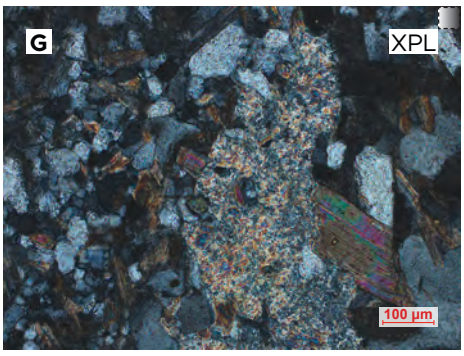

Sample 11

Photomicrographs showcasing one of two fluorescent areas within Sample 11. All images represent the same zone marked with dashed white line on the thin section scan, with images D and E providing a closer look of the same area. The edges of cordierite porphyroblasts are fluorescent similar to other samples.

Fluorescent area:

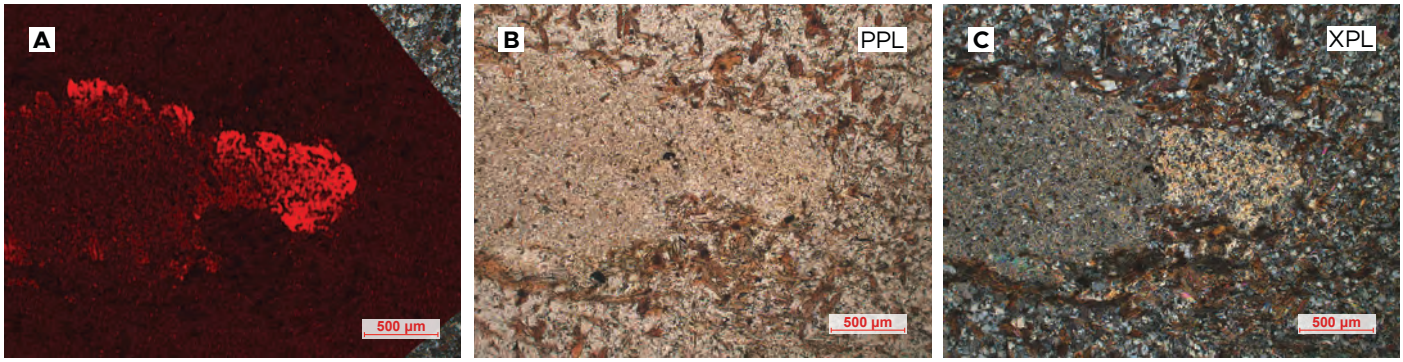

Fluorescent area (close-up):

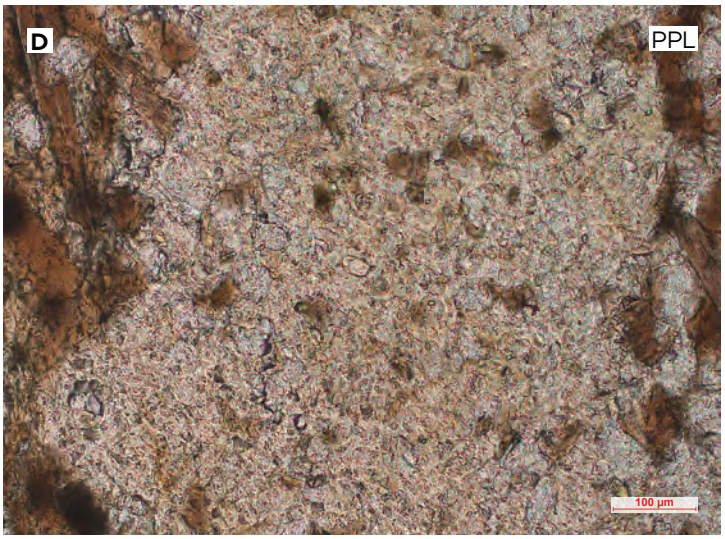

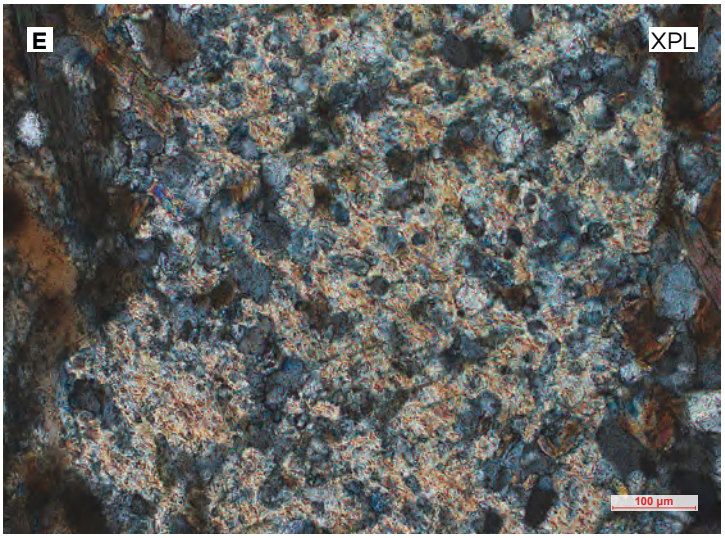

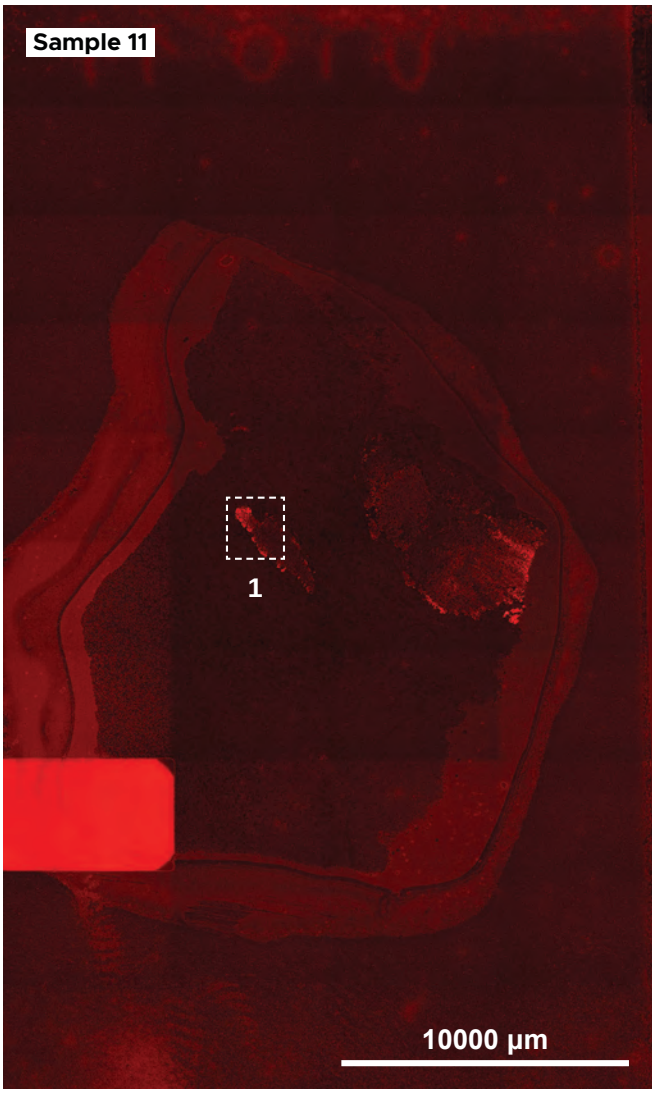

Appendix F - SEM-EDS Data

F1. Unprocessed Chemistry Data for All Sites and Maps Exported from Aztec

SAMPLE 8, COMPOSITE MAP

Element	Signal Type	Line	App. Concentration	k Ratio	Wt%	Wt% Sigma	Standard Name	Factory Standard
O		K series			46,00			
Na	EDS	K series	3,78	0,01595	3,58	0,01	Albite	Yes
Al	EDS	K series	8,98	0,06447	8,67	0,01	Al2O3	Yes
Si	EDS	K series	29,69	0,23526	29,70	0,03	SiO2	Yes
K	EDS	K series	3,06	0,02591	2,77	0,01	KBr	Yes
Ca	EDS	K series	1,38	0,01235	1,25	0,01	Wollastonite	Yes
Ti	EDS	K series	0,29	0,00294	0,31	0,01	Ti	Yes
Mn	EDS	K series	0,04	0,00041	0,04	0,01	Mn	Yes
Fe	EDS	K series	3,33	0,03328	3,40	0,01	Fe	Yes
Rb	EDS	L series	2,84	0,02837	3,58	0,05	Rb (v)	Yes
Cd	EDS	L series	0,06	0,00064	0,08	0,02	Cd	Yes
In	EDS	L series	0,26	0,00233	0,27	0,03	InAs	Yes
Sb	EDS	L series	0,14	0,00145	0,17	0,02	Sb	Yes
Ba	EDS	L series	0,06	0,00056	0,07	0,01	BaF2	Yes
Tb	EDS	L series	0,10	0,00098	0,12	0,02	Tb (v)	Yes
Total					100,00			

SAMPLE 8, SITE 3

Spectrum 11

Element	Signal Type	Line	App. Concentration	k Ratio	Wt%	Wt% Sigma	Standard Name	Factory Standard
O	EDS	K series	161,66	0,54399	47,49	0,18	SiO2	Yes
Na	EDS	K series	5,15	0,02172	1,18	0,05	Albite	Yes
Al	EDS	K series	49,04	0,35224	11,15	0,08	Al2O3	Yes
Si	EDS	K series	116,77	0,92527	28,87	0,12	SiO2	Yes
K	EDS	K series	49,47	0,41908	10,95	0,08	KBr	Yes
Ca	EDS	K series	1,59	0,01423	0,37	0,04	Wollastonite	Yes
Total					100,00			

Spectrum 12

Element	Signal Type	Line	App. Concentration	k Ratio	Wt%	Wt% Sigma	Standard Name	Factory Standard
O		K series			48,14			
Na	EDS	K series	30,24	0,12761	6,83	0,07	Albite	Yes
Al	EDS	K series	50,84	0,36517	12,65	0,08	Al2O3	Yes
Si	EDS	K series	107,08	0,84851	29,17	0,10	SiO2	Yes
Ca	EDS	K series	13,83	0,12355	3,21	0,04	Wollastonite	Yes
Total					100,00			

Spectrum 13

Element	Signal Type	Line	App. Concentration	k Ratio	Wt%	Wt% Sigma	Standard Name	Factory Standard
O		K series			42,21			
Mg	EDS	K series	19,80	0,13129	7,17	0,08	MgO	Yes
Al	EDS	K series	34,65	0,24886	11,76	0,10	Al2O3	Yes
Si	EDS	K series	44,57	0,35318	15,11	0,09	SiO2	Yes
K	EDS	K series	8,26	0,07000	2,02	0,04	KBr	Yes
Ca	EDS	K series	0,99	0,00888	0,24	0,03	Wollastonite	Yes
Ti	EDS	K series	1,54	0,01540	0,43	0,04	Ti	Yes
Mn	EDS	K series	0,84	0,00837	0,24	0,05	Mn	Yes
Fe	EDS	K series	73,90	0,73903	20,81	0,12	Fe	Yes
Total					100,00			

Spectrum 14

Element	Signal Type	Line	App. Concentration	k Ratio	Wt%	Wt% Sigma	Standard Name	Factory Standard
O		K series			28,33			
P	EDS	K series	61,13	0,34193	14,25	0,14	GaP	Yes
Ca	EDS	K series	2,67	0,02382	0,61	0,04	Wollastonite	Yes
La	EDS	L series	56,17	0,50399	14,80	0,28	LaB6	Yes
Ce	EDS	L series	103,94	0,96732	28,09	0,37	CeO2	Yes
Pr	EDS	L series	8,26	0,08259	2,37	0,39	Pr (v)	Yes
Nd	EDS	L series	35,48	0,35481	10,22	0,28	Nd (v)	Yes
Sm	EDS	L series	4,48	0,04484	1,34	0,21	Sm (v)	Yes
Total					100,00			

Spectrum 17

Element	Signal Type	Line	App. Concentration	k Ratio	Wt%	Wt% Sigma	Standard Name	Factory Standard
O		K series			34,33			
Na	EDS	K series	5,28	0,02229	2,01	0,12	Albite	Yes
Al	EDS	K series	7,85	0,05637	3,16	0,08	Al2O3	Yes
Si	EDS	K series	17,27	0,13688	6,13	0,09	SiO2	Yes
P	EDS	K series	53,78	0,30082	12,23	0,12	GaP	Yes
Ca	EDS	K series	15,92	0,14223	3,71	0,06	Wollastonite	Yes
La	EDS	L series	39,97	0,35861	10,90	0,26	LaB6	Yes
Ce	EDS	L series	70,60	0,65708	19,76	0,29	CeO2	Yes
Nd	EDS	L series	25,99	0,25991	7,77	0,23	Nd (v)	Yes
Total					100,00			

Spectrum 18

Element	Signal Type	Line	App. Concentration	k Ratio	Wt%	Wt% Sigma	Standard Name	Factory Standard
O		K series			41,99			
Mg	EDS	K series	8,74	0,05796	5,88	0,11	MgO	Yes
Al	EDS	K series	17,94	0,12884	11,24	0,13	Al2O3	Yes
Si	EDS	K series	26,54	0,21028	16,76	0,13	SiO2	Yes
K	EDS	K series	14,74	0,12490	7,00	0,09	KBr	Yes
Ti	EDS	K series	1,70	0,01701	0,95	0,06	Ti	Yes
Fe	EDS	K series	29,32	0,29323	16,19	0,16	Fe	Yes
Total					100,00			

Spectrum 19

Element	Signal Type	Line	App. Concentration	k Ratio	Wt%	Wt% Sigma	Standard Name	Factory Standard
O		K series			42,03			
Mg	EDS	K series	7,96	0,05278	6,29	0,12	MgO	Yes
Al	EDS	K series	15,31	0,10998	11,29	0,14	Al2O3	Yes
Si	EDS	K series	22,03	0,17459	16,30	0,14	SiO2	Yes
K	EDS	K series	9,90	0,08389	5,44	0,09	KBr	Yes
Ti	EDS	K series	1,14	0,01143	0,73	0,06	Ti	Yes
Mn	EDS	K series	0,38	0,00381	0,25	0,07	Mn	Yes
Fe	EDS	K series	27,76	0,27755	17,67	0,17	Fe	Yes
Total					100,00			

Spectrum 20

Element	Signal Type	Line	App. Concentration	k Ratio	Wt%	Wt% Sigma	Standard Name	Factory Standard
O		K series			30,26			
P	EDS	K series	31,32	0,17520	16,22	0,20	GaP	Yes
Ca	EDS	K series	1,45	0,01297	0,76	0,07	Wollastonite	Yes
La	EDS	L series	25,36	0,22750	15,36	0,41	LaB6	Yes
Ce	EDS	L series	44,13	0,41069	27,40	0,44	CeO2	Yes
Nd	EDS	L series	15,10	0,15103	10,00	0,36	Nd (v)	Yes
Total					100,00			

Spectrum 21

Element	Signal Type	Line	App. Concentration	k Ratio	Wt%	Wt% Sigma	Standard Name	Factory Standard
O		K series			30,54			
Al	EDS	K series	1,09	0,00783	0,97	0,09	Al2O3	Yes
Si	EDS	K series	1,97	0,01565	1,50	0,10	SiO2	Yes
P	EDS	K series	29,30	0,16390	13,58	0,21	GaP	Yes
Ca	EDS	K series	8,55	0,07635	4,10	0,09	Wollastonite	Yes
Fe	EDS	K series	0,84	0,00839	0,48	0,13	Fe	Yes
Y	EDS	L series	3,19	0,03192	2,67	0,37	Y	Yes
La	EDS	L series	21,69	0,19465	12,11	0,39	LaB6	Yes
Ce	EDS	L series	39,57	0,36829	22,65	0,51	CeO2	Yes
Pr	EDS	L series	3,05	0,03049	1,85	0,51	Pr (v)	Yes
Nd	EDS	L series	13,78	0,13778	8,40	0,38	Nd (v)	Yes
Sm	EDS	L series	1,82	0,01822	1,14	0,31	Sm (v)	Yes
Total					100,00			

Spectrum 22

Element	Signal Type	Line	App. Concentration	k Ratio	Wt%	Wt% Sigma	Standard Name	Factory Standard
O		K series			29,05			
Al	EDS	K series	0,79	0,00568	0,94	0,10	Al2O3	Yes
Si	EDS	K series	1,46	0,01158	1,47	0,11	SiO2	Yes
P	EDS	K series	21,28	0,11905	12,93	0,20	GaP	Yes
Ca	EDS	K series	1,13	0,01009	0,68	0,07	Wollastonite	Yes
Y	EDS	L series	1,81	0,01807	1,98	0,41	Y	Yes
La	EDS	L series	21,11	0,18942	14,70	0,44	LaB6	Yes
Ce	EDS	L series	38,93	0,36231	27,79	0,48	CeO2	Yes
Nd	EDS	L series	13,74	0,13741	10,45	0,39	Nd (v)	Yes
Total					100,00			

SAMPLE 1 - SITE 3

Spectrum 23

Element	Signal Type	Line	App. Concentration	k Ratio	Wt%	Wt% Sigma	Standard Name	Factory Standard
O		K series			36,55			
Na	EDS	K series	1,57	0,00662	1,65	0,13	Albite	Yes
Al	EDS	K series	2,39	0,01715	2,45	0,12	Al2O3	Yes
Si	EDS	K series	17,49	0,13855	16,82	0,23	SiO2	Yes
Ca	EDS	K series	0,70	0,00628	0,72	0,09	Wollastonite	Yes
Fe	EDS	K series	1,58	0,01585	1,67	0,14	Fe	Yes
Y	EDS	L series	4,13	0,04126	5,61	0,61	Y	Yes
Zr	EDS	L series	26,70	0,26699	34,54	0,46	Zr	Yes
Total					100,00			

Spectrum 24

Element	Signal Type	Line	App. Concentration	k Ratio	Wt%	Wt% Sigma	Standard Name	Factory Standard
O		K series			49,62			
Na	EDS	K series	1,50	0,00632	1,78	0,24	Albite	Yes
Si	EDS	K series	36,32	0,28779	39,98	0,26	SiO2	Yes
S	EDS	K series	0,54	0,00462	0,77	0,10	FeS2	Yes
Cl	EDS	K series	2,38	0,02080	3,25	0,12	NaCl	Yes
K	EDS	K series	1,02	0,00868	1,19	0,09	KBr	Yes
Ca	EDS	K series	1,61	0,01440	1,85	0,09	Wollastonite	Yes
Ti	EDS	K series	0,34	0,00343	0,46	0,08	Ti	Yes
Zn	EDS	K series	0,82	0,00815	1,10	0,19	Zn	Yes
Total					100,00			

Spectrum 25

Element	Signal Type	Line	App. Concentration	k Ratio	Wt%	Wt% Sigma	Standard Name	Factory Standard
O		K series			43,12			
Mg	EDS	K series	8,14	0,05396	9,84	0,17	MgO	Yes
Al	EDS	K series	10,85	0,07793	12,91	0,19	Al2O3	Yes
Si	EDS	K series	12,42	0,09842	14,93	0,18	SiO2	Yes
K	EDS	K series	0,54	0,00460	0,46	0,06	KBr	Yes
Fe	EDS	K series	19,17	0,19174	18,74	0,22	Fe	Yes
Total					100,00			

Spectrum 26

Element	Signal Type	Line	App. Concentration	k Ratio	Wt%	Wt% Sigma	Standard Name	Factory Standard
O		K series			53,26			
Si	EDS	K series	53,31	0,42242	46,74	0,18	SiO2	Yes
Total					100,00			

Spectrum 27

Element	Signal Type	Line	App. Concentration	k Ratio	Wt%	Wt% Sigma	Standard Name	Factory Standard
O		K series			49,48			
Na	EDS	K series	7,96	0,03358	6,53	0,14	Albite	Yes
Al	EDS	K series	9,99	0,07176	8,95	0,14	Al2O3	Yes
Si	EDS	K series	36,53	0,28948	34,26	0,20	SiO2	Yes
K	EDS	K series	0,59	0,00503	0,51	0,06	KBr	Yes
Ca	EDS	K series	0,31	0,00279	0,27	0,05	Wollastonite	Yes
Total					100,00			

Spectrum 28

Element	Signal Type	Line	App. Concentration	k Ratio	Wt%	Wt% Sigma	Standard Name	Factory Standard
O		K series			48,59			
Na	EDS	K series	10,58	0,04467	8,71	0,15	Albite	Yes
Al	EDS	K series	11,46	0,08228	10,68	0,15	Al2O3	Yes
Si	EDS	K series	31,77	0,25173	31,46	0,20	SiO2	Yes
Ca	EDS	K series	0,65	0,00577	0,55	0,06	Wollastonite	Yes
Total					100,00			

Spectrum 29

Element	Signal Type	Line	App. Concentration	k Ratio	Wt%	Wt% Sigma	Standard Name	Factory Standard
O		K series			40,91			
Si	EDS	K series	0,95	0,00756	0,85	0,08	SiO2	Yes
P	EDS	K series	31,86	0,17819	18,71	0,17	GaP	Yes
Ca	EDS	K series	47,38	0,42337	39,15	0,21	Wollastonite	Yes
Fe	EDS	K series	0,37	0,00368	0,38	0,10	Fe	Yes
Total					100,00			

Spectrum 30

Element	Signal Type	Line	App. Concentration	k Ratio	Wt%	Wt% Sigma	Standard Name	Factory Standard
O		K series			42,79			
Mg	EDS	K series	6,73	0,04466	10,31	0,19	MgO	Yes
Al	EDS	K series	8,02	0,05760	12,12	0,21	Al2O3	Yes
Si	EDS	K series	9,53	0,07552	14,34	0,19	SiO2	Yes
K	EDS	K series	0,32	0,00269	0,34	0,07	KBr	Yes
Ti	EDS	K series	0,62	0,00623	0,76	0,08	Ti	Yes
Fe	EDS	K series	15,84	0,15836	19,35	0,25	Fe	Yes
Total					100,00			

SAMPLE 1 - SITE 4

Spectrum 31

Element	Signal Type	Line	App. Concentration	k Ratio	Wt%	Wt% Sigma	Standard Name	Factory Standard
Li		K series			0,00			
O		K series			30,54			
Al	EDS	K series	0,40	0,00286	0,68	0,13	Al2O3	Yes
Si	EDS	K series	1,23	0,00975	1,78	0,14	SiO2	Yes
P	EDS	K series	14,82	0,08287	13,03	0,25	GaP	Yes
S	EDS	K series	0,46	0,00396	0,58	0,11	FeS2	Yes
Ca	EDS	K series	0,45	0,00398	0,40	0,08	Wollastonite	Yes
Cr	EDS	K series	0,00	0,00000	0,00	0,23	Cr	Yes
Fe	EDS	K series	2,73	0,02734	2,95	0,19	Fe	Yes
Y	EDS	L series	1,49	0,01494	2,38	0,50	Y	Yes
La	EDS	L series	13,26	0,11898	13,68	0,52	LaB6	Yes
Ce	EDS	L series	23,29	0,21674	24,64	0,58	CeO2	Yes
Nd	EDS	L series	8,28	0,08281	9,34	0,51	Nd (v)	Yes
Total					100,00			

Spectrum 32

Element	Signal Type	Line	App. Concentration	k Ratio	Wt%	Wt% Sigma	Standard Name	Factory Standard
O		K series			31,38			
Si	EDS	K series	1,01	0,00801	1,51	0,14	SiO2	Yes
P	EDS	K series	17,60	0,09844	16,06	0,26	GaP	Yes
Ca	EDS	K series	0,70	0,00624	0,65	0,10	Wollastonite	Yes
La	EDS	L series	15,62	0,14017	16,91	0,55	LaB6	Yes
Ce	EDS	L series	30,15	0,28060	33,48	0,55	CeO2	Yes
Total					100,00			

Spectrum 33

Element	Signal Type	Line	App. Concentration	k Ratio	Wt%	Wt% Sigma	Standard Name	Factory Standard
O		K series			53,24			
Al	EDS	K series	0,13	0,00096	0,11	0,07	Al2O3	Yes
Si	EDS	K series	60,87	0,48237	46,65	0,18	SiO2	Yes
Total					100,00			

Spectrum 34

Element	Signal Type	Line	App. Concentration	k Ratio	Wt%	Wt% Sigma	Standard Name	Factory Standard
O	EDS	K series	43,99	0,14802	50,85	0,34	SiO2	Yes
Mg	EDS	K series	0,90	0,00596	0,96	0,09	MgO	Yes
Al	EDS	K series	17,91	0,12866	17,29	0,20	Al2O3	Yes
Si	EDS	K series	20,08	0,15914	22,72	0,23	SiO2	Yes
K	EDS	K series	8,82	0,07468	8,19	0,14	KBr	Yes
Total					100,00			

Spectrum 35

Element	Signal Type	Line	App. Concentration	k Ratio	Wt%	Wt% Sigma	Standard Name	Factory Standard
O	EDS	K series	48,98	0,16482	48,91	0,36	SiO2	Yes
Mg	EDS	K series	3,15	0,02090	3,54	0,12	MgO	Yes
Al	EDS	K series	14,58	0,10475	15,12	0,19	Al2O3	Yes
Si	EDS	K series	17,22	0,13646	19,61	0,21	SiO2	Yes
K	EDS	K series	6,78	0,05742	6,04	0,12	KBr	Yes
Fe	EDS	K series	6,57	0,06566	6,77	0,17	Fe	Yes
Total					100,00			

Spectrum 37

Element	Signal Type	Line	App. Concentration	k Ratio	Wt%	Wt% Sigma	Standard Name	Factory Standard
O		K series			41,06			
Mg	EDS	K series	1,56	0,01037	2,66	0,13	MgO	Yes
Al	EDS	K series	2,32	0,01670	3,37	0,13	Al2O3	Yes
Si	EDS	K series	4,09	0,03237	5,30	0,13	SiO2	Yes
Ti	EDS	K series	35,47	0,35466	41,17	0,25	Ti	Yes
Fe	EDS	K series	5,20	0,05201	6,45	0,18	Fe	Yes
Total					100,00			

Spectrum 38

Element	Signal Type	Line	App. Concentration	k Ratio	Wt%	Wt% Sigma	Standard Name	Factory Standard
O		K series			30,46			
Al	EDS	K series	0,48	0,00344	0,85	0,13	Al2O3	Yes
Si	EDS	K series	1,00	0,00794	1,50	0,14	SiO2	Yes
P	EDS	K series	16,12	0,09019	14,66	0,25	GaP	Yes
Ca	EDS	K series	0,46	0,00412	0,42	0,09	Wollastonite	Yes
La	EDS	L series	14,31	0,12840	15,01	0,53	LaB6	Yes
Ce	EDS	L series	25,95	0,24152	27,91	0,57	CeO2	Yes
Nd	EDS	L series	8,00	0,08002	9,18	0,48	Nd (v)	Yes
Total					100,00			

Spectrum 39

Element	Signal Type	Line	App. Concentration	k Ratio	Wt%	Wt% Sigma	Standard Name	Factory Standard
O		K series			53,26			
Si	EDS	K series	55,65	0,44099	46,74	0,18	SiO2	Yes
Total					100,00			

F2. Mineral Formulas and Stoichiometric Calculations derived from Spectrum Data for Samples 1 & 8

These tables present mineral formulas derived from elemental weight percentages extracted from Aztec software. The calculations were made to verify mineral identification. Normalization was not applied to oxide weight percentages, if they differed less than 5% from the total of 100% due to small difference and in order to preserve the original values.

Sample 1 Site 3

Spectrum 23

Element	Wt %	σ	El. Atomic Wt	Oxide	Oxide Mol. Wt	Oxide Wt %	Mol. Proportion	# O	O Atomic Prop-n	# Anions	O / Cation	Cations
O	36.55	0.41	16	—	—	—	—	—	—	—	—	—
Zr	34.54	0.46	91.22	ZrO_2	123.22	46.66	0.38	2	0.76	1.33	2.00	0.67
Si	16.82	0.23	28.09	SiO_2	60.08	35.98	0.60	2	1.20	2.11	2.00	1.06
Y	5.61	0.61	88.91	Y_2O_3	225.81	7.12	0.03	3	0.09	0.17	1.50	0.11
Al	2.45	0.12	26.98	Al_2O_3	101.96	4.63	0.05	3	0.14	0.24	1.50	0.16
Fe	1.67	0.14	55.85	FeO	71.85	2.15	0.03	1	0.03	0.05	1.00	0.05
Na	1.65	0.13	22.99	Na_2O	61.98	2.22	0.04	1	0.04	0.06	0.50	0.13
Ca	0.72	0.09	40.08	CaO	56.08	1.01	0.02	1	0.02	0.03	1.00	0.03
	100.01					99.77			2.27			

Oxygens (Norm.) = 4 **Normalization factor =** 1.76

Formula: $Zr_{0.67}Si_{1.06}Al_{0.16}Fe_{0.05}Ca_{0.03}Na_{0.13}O_4$ **Mineral:** Zircon

Spectrum 24

Element	Wt %	σ	El. Atomic Wt	Oxide	Oxide Mol. Wt	Oxide Wt %	Mol. Proportion	# O	O Atomic Prop-n	# Anions	O / Cation	Cations
O	49.62	0.29	16	—	—	—	—	—	—	—	—	—
Si	39.98	0.26	28.09	SiO_2	60.08	85.51	1.42	2	2.85	6.75	2.00	3.37
Cl	3.25	0.12	35.45	Cl_2O_7	182.9	8.38	0.05	7	0.32	0.76	3.50	0.22
Ca	1.85	0.09	40.08	CaO	56.08	2.59	0.05	1	0.05	0.11	1.00	0.11
Na	1.78	0.24	22.99	Na_2O	61.98	2.40	0.04	1	0.04	0.09	0.50	0.18
K	1.19	0.09	39.1	K_2O	94.2	1.43	0.02	1	0.02	0.04	0.50	0.07
Zn	1.1	0.19	65.38	ZnO	81.38	1.37	0.02	1	0.02	0.04	1.00	0.04
S	0.77	0.1	32.07	SO_3	80.06	1.92	0.02	3	0.07	0.17	3.00	0.06
Ti	0.46	0.08	47.87	TiO_2	79.87	0.77	0.01	2	0.02	0.05	2.00	0.02
	100					104.38			3.38			

Oxygens (Norm.) = 8 **Normalization factor =** 2.37

Formula: $Na_{0.18}K_{0.07}Ca_{0.11}Zn_{0.04}Ti_{0.02}Si_{3.37}S_{0.06}Cl_{0.22}O_{11}$ **Mineral:** Plagioclase feldspar (possibly oligoclase) with Zn, Ti and Cl impurities.

Spectrum 25

Element	Wt %	σ	El. Atomic Wt	Oxide	Oxide Mol. Wt	Oxide Wt %	Mol. Proportion	# O	O Atomic Prop-n	# Anions	O / Cation	Cations
O	43.12	0.26	16	—	—	—	—	—	—	—	—	—
Fe	18.74	0.22	55.85	FeO	71.85	24.11	0.34	1	0.34	1.46	1.00	1.46
Si	14.93	0.18	28.09	SiO_2	60.08	31.93	0.53	2	1.06	4.63	2.00	2.31
Al	12.91	0.19	26.98	Al_2O_3	101.96	24.39	0.24	3	0.72	3.12	1.50	2.08
Mg	9.84	0.17	24.31	MgO	40.3	16.31	0.40	1	0.40	1.76	1.00	1.76
K	0.46	0.06	39.1	K_2O	94.2	0.55	0.01	1	0.01	0.03	0.50	0.05
	100					97.30			2.53			

Oxygens (Norm.) = 11 **Normalization factor =** 4.35

Formula: $K_{0.05}Mg_{1.76}Fe_{1.46}Si_{2.31}Al_{2.08}O_{11}$ **Mineral:** Biotite (possibly alternatining into chlorite)

Spectrum 26

Element	Wt %	σ	El. Atomic Wt	Oxide	Oxide Mol. Wt	Oxide Wt %	Mol. Proportion	# O	O Atomic Prop-n	# Anions	O / Cation	Cations
O	53.26	0.18	16	—	—	—	—	—	—	—	—	—
Si	46.74	0.18	28.09	SiO_2	60.08	99.97	1.66	2	3.33	2.00	2.00	1.00
	100					99.97			3.33			

Formula: SiO2 **Mineral:** Quartz

Spectrum 27

Element	Wt %	σ	El. Atomic Wt	Oxide	Oxide Mol. Wt	Oxide Wt %	Mol. Proportion	# O	O Atomic Prop-n	# Anions	O / Cation	Cations
O	49.48	0.22	16	—	—	—	—	—	—	—	—	—
Si	34.26	0.2	28.09	SiO_2	60.08	73.28	1.22	2	2.44	6.31	2	3.16
Al	8.95	0.14	26.98	Al_2O_3	101.96	16.91	0.17	3	0.50	1.29	1.5	0.86
Na	6.53	0.14	22.99	Na_2O	61.98	8.80	0.14	1	0.14	0.37	0.5	0.73
K	0.51	0.06	39.1	K_2O	94.2	0.61	0.01	1	0.01	0.02	0.5	0.03
Ca	0.27	0.05	40.08	CaO	56.08	0.38	0.01	1	0.01	0.02	1	0.02
	100					99.98			3.09			

Oxygens (Norm.) = 8 **Normalization factor =** 2.59

Formula: $Na_{0.73}K_{0.03}Ca_{0.02}Al_{0.86}Si_{3.16}O_8$ **Mineral:** Plagioclase feldspar (albite)

Spectrum 28

Element	Wt %	σ	El. Atomic Wt	Oxide	Oxide Mol. Wt	Oxide Wt %	Mol. Proportion	# O	O Atomic Prop-n	# Anions	O / Cation	Cations
O	48.59	0.22	16	—	—	—	—	—	—	—	—	—
Si	31.46	0.2	28.09	SiO_2	60.08	67.29	1.12	2	2.24	5.90	2.00	2.95
Al	10.68	0.15	26.98	Al_2O_3	101.96	20.18	0.20	3	0.59	1.56	1.50	1.04
Na	8.71	0.15	22.99	Na_2O	61.98	11.74	0.19	1	0.19	0.50	0.50	1.00
Ca	0.55	0.06	40.08	CaO	56.08	0.77	0.01	1	0.01	0.04	0.50	0.07
	99.99					99.98			3.04			

Oxygens (Norm.) = 8.00 **Normalization factor =** 2.63

Formula: $NaCa_{0.07}Al_{1.04}Si_{2.95}O_8$ **Mineral:** Plagioclase feldspar (possibly oligoclase)

Spectrum 29

Element	Wt %	σ	El. Atomic Wt	Oxide	Oxide Mol. Wt	Oxide Wt %	Mol. Proportion	# O	O Atomic Prop-n	# Anions	O / Cation	Cations
O	40.91	0.21	16	—	—	—	—	—	—	—	—	—
Ca	39.15	0.21	40.08	CaO	56.08	54.78	0.98	1	0.98	1.53	1.00	1.53
P	18.71	0.17	30.97	P_2O_5	141.94	42.88	0.30	5	1.51	2.37	2.50	0.95
Si	0.85	0.08	28.09	SiO_2	60.08	1.82	0.03	2	0.06	0.09	2.00	0.05
Fe	0.38	0.1	55.85	FeO	71.85	0.49	0.01	1	0.01	0.01	1.00	0.01
	100					99.96			2.55			

Oxygens (Norm.) = 4 **Normalization factor =** 1.57

Formula: $Ca_{1.53}P_{0.95}Si_{0.05}Fe_{0.01}O_4$ **Mineral:** Apatite

Spectrum 30

Element	Wt %	σ	El. Atomic Wt	Oxide	Oxide Mol. Wt	Oxide Wt %	Mol. Proportion	# O	O Atomic Prop-n	# Anions	O / Cation	Cations
O	42.79	0.29	16	—	—	—	—	—	—	—	—	—
Fe	19.35	0.25	55.85	FeO	71.85	24.89	0.35	1	0.35	1.52	1.00	1.52
Si	14.34	0.19	28.09	SiO_2	60.08	30.67	0.51	2	1.02	4.49	2.00	2.24
Al	12.12	0.21	26.98	Al_2O_3	101.96	22.90	0.22	3	0.67	2.96	1.50	1.98
Mg	10.31	0.19	24.31	MgO	40.3	17.09	0.42	1	0.42	1.86	1.00	1.86
Ti	0.76	0.08	47.87	TiO_2	79.87	1.27	0.02	2	0.03	0.14	2.00	0.07
K	0.34	0.07	39.1	K_2O	94.2	0.41	0.004	1	0.004	0.02	0.50	0.04
	100.01					97.23			2.50			

Oxygens (Norm.) = 11.00 **Normalization factor =** 4.40

Formula: $K_{0.04}(Mg_{1.86}Fe_{1.52}Ti_{0.07})Al_{1.98}Si_{2.24}O_{11}$ **Mineral:** Biotite (altered due to chloritization)

Sample 8 Site 3

Spectrum 11

Element	Wt %	σ	El. Atomic Wt	Oxide	Oxide Mol. Wt	Oxide Wt %	Mol. Proportion	#O	O Atomic Prop-n	# of Anions	O / Cation	Cations
O	46.47	0.11	16	—	—	—	—	—	—	—	—	—
Si	29.44	0.1	28.09	SiO_2	60.09	62.98	1.05	2	2.10	5.77	2	2.89
Al	11.33	0.07	26.98	Al_2O_3	101.96	21.41	0.21	3	0.63	1.74	1.5	1.16
K	11.19	0.07	39.1	K_2O	94.2	13.48	0.14	1	0.14	0.39	0.5	0.79
Na	1.19	0.05	22.99	Na_2O	61.98	1.60	0.03	1	0.03	0.07	0.5	0.14
Ca	0.38	0.04	40.08	CaO	56.08	0.53	0.01	1	0.01	0.03	1	0.03
	100				100.00	100.00			2.90			

Normalization factor = 2.75 **Oxygens (Norm.) =** 8

Formula: $K_{0.79}Na_{0.14}Ca_{0.03}Al_{1.16}Si_{2.89}O_8$ **Mineral:** K-feldpsar

Spectrum 12

Element	Wt %	σ	El. Atomic Wt	Oxide	Oxide Mol. Wt	Oxide Wt %	Mol. Proportion	#O	O Atomic Prop-n	# of Anions	O / Cation	Cations
O	48.14	0.11	16	—	—	—	—	—	—	—	—	—
Si	29.17	0.1	28.09	SiO_2	60.09	62.40	1.04	2	2.08	5.52	2	2.76
Al	12.65	0.08	26.98	Al_2O_3	101.96	23.90	0.23	3	0.70	1.87	1.5	1.25
Na	6.83	0.07	22.99	Na_2O	61.98	9.21	0.15	1	0.15	0.39	0.5	0.79
Ca	3.21	0.04	40.08	CaO	56.08	4.49	0.08	1	0.08	0.21	1	0.21
						100.00			3.01			

Normalization factor = 2.66 **Oxygens (Norm.) =** 8

Formula: $Na_{0.79}Ca_{0.21}Al_{1.25}Si_{2.76}O_8$ **Mineral:** Plagioclase feldspar

Spectrum 13

Element	Wt %	σ	El. Atomic Wt	Oxide	Oxide Mol. Wt	Oxide Wt %	Mol. Proportion	#O	O Atomic Prop-n	# of Anions	O / Cation	Cations	Oxygens (Norm.)
O	42.21	0.14	16	—	—	—	—	—	—	—	—	—	11.00
Fe	20.81	0.12	55.85	FeO	71.85	26.77	0.37	1	0.37	1.67	1	1.67	
Si	15.11	0.09	28.09	SiO_2	60.08	32.32	0.54	2	1.08	4.83	2	2.41	
Al	11.76	0.1	26.98	Al_2O_3	101.96	22.22	0.22	3	0.65	2.93	1.5	1.96	
Mg	7.17	0.08	24.31	MgO	40.3	11.89	0.29	1	0.29	1.32	1	1.32	
K	2.02	0.04	39.1	K_2O	94.2	2.43	0.03	1	0.03	0.12	0.5	0.23	
Ti	0.43	0.04	47.87	TiO_2	79.87	0.72	0.01	2	0.02	0.08	2	0.04	
Ca	0.24	0.03	40.08	CaO	56.08	0.34	0.01	1	0.01	0.03	1	0.03	
Mn	0.24	0.05	54.9	MnO	70.94	0.31	0.00	1	0.00	0.02	1	0.02	
						96.99			2.45				

Normalization factor = 4.49 **Oxygens (Norm.) =** 11

Formula: $K_{0.23}(Mg_{1.32}Fe_{1.67}Ti_{0.04}Mn_{0.02}Ca_{0.03})Al_{1.96}Si_{2.41}O_{11}$ **Mineral:** Biotie

Spectrum 14

Element	Wt %	σ	El. Atomic Wt	Oxide	Oxide Mol. Wt	Oxide Wt %	Mol. Proportion	#O	O Atomic Prop-n	# of Anions	O / Cation	Cations
O	28.33	0.26	16	—	—	—	—	—	—	—	—	—
Ce	28.09	0.37	140.12	Ce_2O_3	328.23	32.90	0.10	3	0.30	0.68	1.5	0.45
La	14.8	0.28	138.91	La_2O_3	325.81	17.36	0.05	3	0.16	0.36	1.5	0.24
P	14.25	0.14	30.97	P_2O_5	141.94	32.65	0.23	5	1.15	2.60	2.5	1.04
Nd	10.22	0.28	144.24	Nd_2O_3	336.48	11.92	0.04	3	0.11	0.24	1.5	0.16
Pr	2.37	0.39	140.91	Pr_2O_3	329.81	2.77	0.01	3	0.03	0.06	1.5	0.04
Sm	1.34	0.21	150.36	Sm_2O_3	348.72	1.55	0.00	3	0.01	0.03	1.5	0.02
Ca	0.61	0.04	40.08	CaO	56.08	0.85	0.02	1	0.02	0.03	1	0.03
						100.01			1.77			

Normalization factor = 2.26 **Oxygens (Norm.) =** 4

Formula $(Ce_{0.45}La_{0.24}Nd_{0.16}Pr_{0.04}Sm_{0.02})Ca_{0.03}P_{1.04}O_4$ **Mineral:** Monazite

Spectrum 17

Element	Wt %	σ	El. Atomic Wt	Oxide	Oxide Mol. Wt	Oxide Wt %	Mol. Proportion	#O	O Atomic Prop-n	# of Anions	O / Cation	Cations
O	34.33	0.23	16	O	—	—	—	—	—	—	—	—
Ce	19.76	0.29	140.12	Ce_2O_3	328.23	23.14	0.07	3	0.21	0.39	1.5	0.26
P	12.23	0.12	30.97	P_2O_5	141.94	28.03	0.20	5	0.99	1.84	2.5	0.74
La	10.9	0.26	138.91	La_2O_3	325.81	12.78	0.04	3	0.12	0.22	1.5	0.15
Nd	7.77	0.23	144.24	Nd_2O_3	336.48	9.06	0.03	3	0.08	0.15	1.5	0.10
Si	6.13	0.09	28.09	SiO_2	60.08	13.11	0.22	2	0.44	0.81	2	0.41
Ca	3.71	0.06	40.08	CaO	56.08	5.19	0.09	1	0.09	0.17	1	0.17
Al	3.16	0.08	26.98	Al_2O_3	101.96	5.97	0.06	3	0.18	0.33	1.5	0.22
Na	2.01	0.12	22.99	Na_2O	61.98	2.71	0.04	1	0.04	0.08	0.5	0.16
						100.00			2.15			

Normalization factor = 1.86 **Oxygens (Norm.) =** 4

Formula $(Ce_{0.26}La_{0.15}Nd_{0.10})Na_{0.16}Ca_{0.17}Al_{0.22}Si_{0.41}P_{0.74}O_4$ **Mineral:** Monazite with minor impurities Na Ca, Al, and Si.

Spectrum 18

Element	Wt %	σ	El. Atomic Wt	Oxide	Oxide Mol. Wt	Oxide Wt %	Mol. Proportion	#O	O Atomic Prop-n	# of Anions	O / Cation	Cations
O	41.99	0.19	16	O	—	—	—	—	—	—	—	—
Si	16.76	0.13	28.09	SiO_2	60.08	35.85	0.60	2	1.19	5.29	2	2.65
Fe	16.19	0.16	55.85	FeO	71.85	20.83	0.29	1	0.29	1.29	1	1.29
Al	11.24	0.13	26.98	Al_2O_3	101.96	21.24	0.21	3	0.62	2.77	1.5	1.85
K	7	0.09	39.1	K_2O	94.20	8.43	0.09	1	0.09	0.40	0.5	0.79
Mg	5.88	0.11	24.31	MgO	40.30	9.75	0.24	1	0.24	1.07	1	1.07
Ti	0.95	0.06	47.87	TiO_2	79.87	1.59	0.02	2	0.04	0.18	2	0.09
						97.68			2.48			

Normalization factor = 4.44 **Oxygens (Norm.) =** 11

Formula $K_{0.79}(Mg_{1.07}Fe_{1.29}Ti_{0.09})Al_{1.85}Si_{2.65}O_{11}$ **Mineral:** Biotite

Spectrum 19

Element	Wt %	σ	El. Atomic Wt	Oxide	Oxide Mol. Wt	Oxide Wt %	Mol. Proportion	#O	O Atomic Prop-n	# of Anions	O / Cation	Cations
O	42.03	0.2	16	O	—	—	—	—	—	—	—	—
Fe	17.67	0.17	55.85	FeO	71.85	22.73	0.32	1	0.32	1.41	1	1.41
Si	16.3	0.14	28.09	SiO_2	60.08	34.86	0.58	2	1.16	5.17	2	2.59
Al	11.29	0.14	26.98	Al_2O_3	101.96	21.33	0.21	3	0.63	2.80	1.5	1.87
Mg	6.29	0.12	24.31	MgO	40.30	10.43	0.26	1	0.26	1.15	1	1.15
K	5.44	0.09	39.1	K_2O	94.20	6.55	0.07	1	0.07	0.31	0.5	0.62
Ti	0.73	0.06	47.87	TiO_2	79.87	1.22	0.02	2	0.03	0.14	2	0.07
Mn	0.25	0.07	54.94	MnO	70.94	0.32	0.00	1	0.00	0.02	1	0.02
	100					97.45			2.47			

Normalization factor = 4.46 **Oxygens (Norm.) =** 11

Formula $K_{0.62}(Mg_{1.15}Fe_{1.41}Ti_{0.07}Mn_{0.02})Al_{1.87}Si_{2.59}O_{11}$ **Mineral:** Biotite

Spectrum 20

Element	Wt %	σ	El. Atomic Wt	Oxide	Oxide Mol. Wt	Oxide Wt %	Mol. Proportion	#O	O Atomic Prop-n	# of Anions	O / Cation	Cations
O	30.26	0.31	16	O	—	—	—	—	—	—	—	—
Ce	27.4	0.44	140.12	Ce_2O_3	328.23	32.09	0.10	3	0.29	0.62	1.5	0.41
P	16.22	0.2	30.97	P_2O_5	141.94	37.17	0.26	5	1.31	2.77	2.5	1.11
La	15.36	0.41	138.91	La_2O_3	325.81	18.01	0.06	3	0.17	0.35	1.5	0.23
Nd	10	0.36	144.24	Nd_2O_3	336.48	11.66	0.03	3	0.10	0.22	1.5	0.15
Ca	0.76	0.07	40.08	CaO	56.08	1.06	0.02	1	0.02	0.04	1	0.04
						100.00			1.89			

Normalization factor = 2.11 **Oxygens (Norm.) =** 4

Formula $(Ce_{0.41}La_{0.23}Nd_{0.15}Ca_{0.04})P_{1.11}O_4$ **Mineral:** Monazite

Spectrum 21

Element	Wt %	σ	El. Atomic Wt	Oxide	Oxide Mol. Wt	Oxide Wt %	Mol. Proportion	#O	O Atomic Prop-n	# of Anions	O / Cation	Cations
O	30.54	0.41	16	O	—	—	—	—	—	—	—	—
Ce	22.65	0.51	140.12	Ce_2O_3	328.23	26.53	0.08	3	0.24	0.51	1.5	0.34
P	13.58	0.21	30.97	P_2O_5	141.94	31.12	0.22	5	1.10	2.30	2.5	0.92
La	12.11	0.39	138.91	La_2O_3	325.81	14.20	0.04	3	0.13	0.27	1.5	0.18
Nd	8.4	0.38	144.24	Nd_2O_3	336.48	9.80	0.03	3	0.09	0.18	1.5	0.12
Ca	4.1	0.09	40.08	CaO	56.08	5.74	0.10	1	0.10	0.21	1	0.21
Y	2.67	0.37	88.91	Y_2O_3	225.81	3.39	0.02	3	0.05	0.09	1.5	0.06
Pr	1.85	0.51	140.91	Pr_2O_3	329.81	2.17	0.01	3	0.02	0.04	1.5	0.03
Si	1.5	0.1	28.09	SiO_2	60.08	3.21	0.05	2	0.11	0.22	2	0.11
Sm	1.14	0.31	150.36	Sm_2O_3	348.72	1.32	0.00	3	0.01	0.02	1.5	0.02
Al	0.97	0.09	26.98	Al_2O_3	101.96	1.83	0.02	3	0.05	0.11	1.5	0.08
Fe	0.48	0.13	55.85	FeO	71.85	0.62	0.01	1	0.01	0.02	1	0.02
						99.92			1.90			

Normalization factor = 2.10 Oxygens (Norm.) = 4

Formula $(Ce_{0.34}La_{0.18}Nd_{0.12}Y_{0.06}Pr_{0.03}Sm_{0.02})Ca_{0.21}Si_{0.11}Al_{0.08}Fe_{0.02}P_{0.92}O_4$ Mineral: Monazite with impurities Ca, Si, Al and Fe.

Spectrum 22

Element	Wt %	σ	El. Atomic Wt	Oxide	Oxide Mol. Wt	Oxide Wt %	Mol. Proportion	#O	O Atomic Prop-n	# of Anions	O / Cation	Cations
O	29.05	0.37	16	O	—	—	—	—	—	—	—	—
Ce	27.79	0.48	140.12	Ce_2O_3	328.23	32.55	0.10	3	0.30	0.66	1.5	0.44
La	14.7	0.44	138.91	La_2O_3	325.81	17.24	0.05	3	0.16	0.35	1.5	0.23
P	12.93	0.2	30.97	P_2O_5	141.94	29.63	0.21	5	1.04	2.30	2.5	0.92
Nd	10.45	0.39	144.24	Nd_2O_3	336.48	12.19	0.04	3	0.11	0.24	1.5	0.16
Y	1.98	0.41	88.91	Y_2O_3	225.81	2.51	0.01	3	0.03	0.07	1.5	0.05
Si	1.47	0.11	28.09	SiO_2	60.08	3.14	0.05	2	0.10	0.23	2	0.12
Al	0.94	0.1	26.98	Al_2O_3	101.96	1.78	0.02	3	0.05	0.12	1.5	0.08
Ca	0.68	0.07	40.08	CaO	56.08	0.95	0.02	1	0.02	0.04	1	0.04
						99.99			1.82			

Normalization factor = 2.20 Oxygens (Norm.) = 4

Formula $(Ce_{0.44}La_{0.23}Nd_{0.16}Y_{0.05}Ca_{0.04})Si_{0.12}Al_{0.08}P_{0.92}O_4$ Mineral: Monazite with impurities with Y, Si, Al and Ca.

F3. SEM-EDS Error Margins for Spectra with Sigma Weight % Values over 0.3%

Sigma weight % values represent the standard deviation of element measurements in SEM-EDS analyses and provide an estimate of the error range. This table presents all error margins calculated for spectra and elements with sigma values above 0.3%. The value of 0.3% was chosen as a high enough boundary to identify potentially unreliable measurements. This table was created to acknowledge that there may be some uncertainties in the data.

Sample 8, Site 3

Spectrum	Element	Weight%	Weight% σ	Relative Error (%)
14	Ce	28.09	0.37	1.32
20	Ce	27.4	0.44	1.61
20	La	15.36	0.41	2.67
21	O	30.54	0.41	1.34
21	Pr	1.85	0.51	27.57
21	Sm	1.14	0.31	27.19
22	Ce	27.79	0.48	1.73
22	Y	1.98	0.41	20.71

Sample 1, Site 3

Spectrum	Element	Weight%	Weight% σ	Relative Error (%)
23	Zr	34.54	0.46	1.33
23	Y	5.61	0.61	10.87
24	O	49.62	0.29	0.58
30	O	42.79	0.29	0.68
30	Fe	19.35	0.25	1.29
30	Al	12.12	0.21	1.73
30	Mg	10.31	0.19	1.84

Sample 1, Site 4

Spectrum	Element	Weight%	Weight% σ	Relative Error (%)
31	O	32.03	0.6	1.87
31	Ce	30.59	0.62	2.03
34	O	50.85	0.34	0.67
35	O	48.91	0.36	0.74
35	Si	19.61	0.21	1.07
37	O	51.85	0.54	1.04
38	Ce	26.58	0.56	2.11
38	La	14.29	0.51	3.57

Sample 15, Site 7

Spectrum	Element	Weight%	Weight% σ	Relative Error (%)
57	O	67.1	0.53	0.79
57	Ti	19.23	0.35	1.82
58	O	46.78	0.49	1.05
58	Si	18.81	0.37	1.97
61	O	46.13	0.35	0.76

F4. Composite Elemental Maps of Si, O, Na, La, Ca, Ce, Nd (Sample 8)

1. 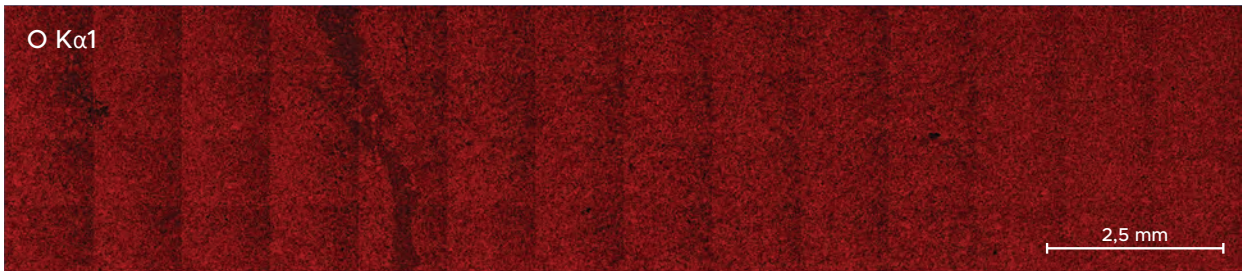

2. 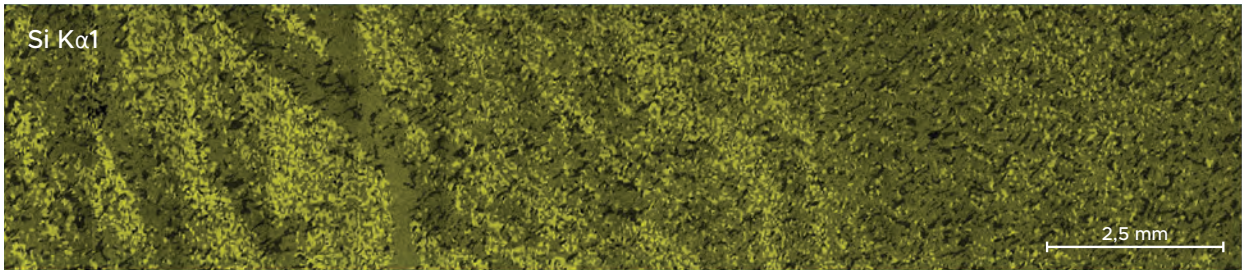

3. 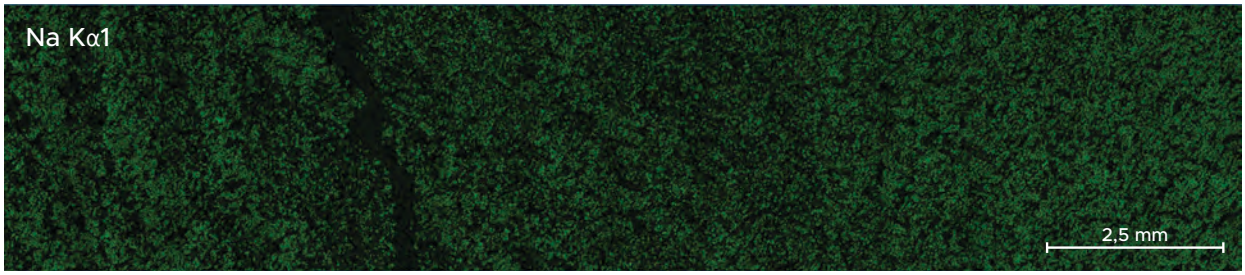

4. 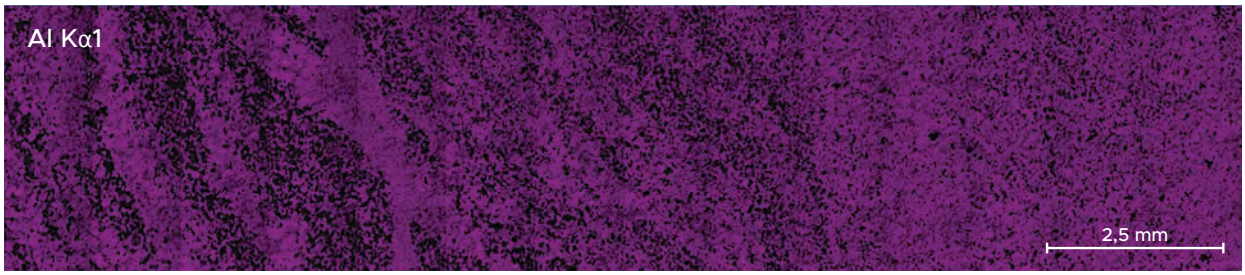

5. 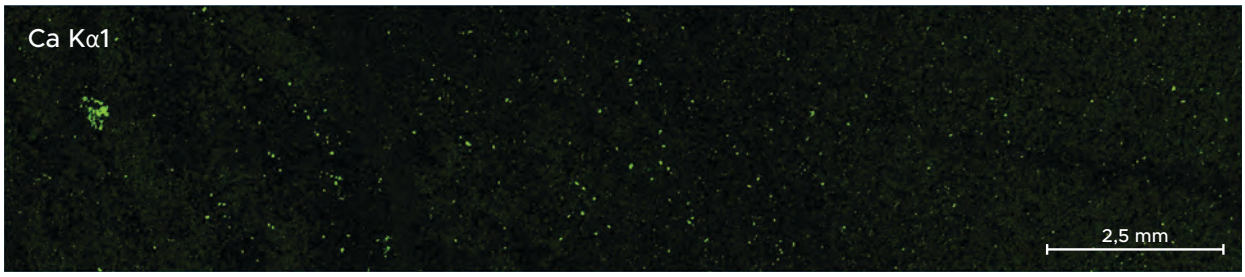

6. 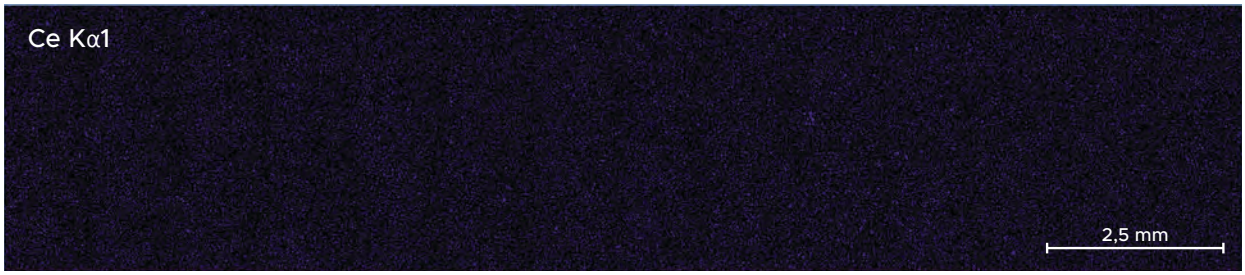

7.